University of Stuttgart
Institute of Nuclear Technology
and Energy Systems

Thermo-hydraulic Analysis of Wall Bounded Flows with Supercritical Carbon Dioxide Using Direct Numerical Simulation

A doctoral dissertation by

Sandeep Pandey

November 2018 IKE 8-131

University of Stuttgart
Institute of Nuclear Technology
and Energy Systems

Thermo-hydraulic Analysis of Wall Bounded Flows with Supercritical Carbon Dioxide Using Direct Numerical Simulation

von der Fakultät Energie-, Verfahrens- und Biotechnik der Universität Stuttgart zur Erlangung der Würde eines Doktor-Ingenieurs (Dr.-Ing.) genehmigte Abhandlung

vorgelegt von
Sandeep Pandey (M. Tech.)
aus Jodhpur, Indien

Hauptberichter : Prof. Dr.-Ing. habil. E. Laurien
Mitberichter : Prof. Dr.-Ing. habil. B. Weigand

Tag der Einreichung : 14.11.2018
Tag der mündlichen Prüfung : 12.04.2019

ISSN : 0173-6892

November 2018 **IKE 8-131**

Eidesstattliche Erklärung zu meiner Dissertation mit dem Titel:
Thermo-hydraulic Analysis of Wall Bounded Flows with Supercritical Carbon Dioxide Using Direct Numerical Simulation

Hiermit erkläre ich, dass ich die beigefügte Dissertation selbstständig verfasst und keine anderen als die angegebenen Hilfsmittel genutzt habe. Alle wörtlich oder inhaltlich übernommenen Stellen habe ich als solche gekennzeichnet.

Ich versichere außerdem, dass ich die beigefügte Dissertation nur in diesem und keinem anderen Promotionsverfahren eingereicht habe und, dass diesem Promotionsverfahren keine endgültig gescheiterten Promotionsverfahren vorausgegangen sind.

Stuttgart, den 08.11.2018 — Sandeep

Ort, Datum — Unterschrift

Name / Anschrift

Sandeep Pandey
Wiener Strasse 88
70469 Stuttgart.

I would like to dedicate this thesis to my loving mother ...

"asato mā sadgamaya
tamasomā jyotir gamaya
mrityormāamritam gamaya"
From ignorance, lead me to truth
From darkness, lead me to light
From death, lead me to immortality.

Acknowledgements

This work would not be complete without a proper acknowledgment of the invaluable support, advice, and encouragement I have received from several sources around me, to only some of whom, it is possible to give a particular mention here.

I wish to first express my deep gratitude to Prof. Eckart Laurien for his kind supervision, constant guidance, motivation and helpful advice throughout the course of this study. I am extremely thankful to him for allowing me to pursue a research subject of my choosing. I would also like to thank my examiner Prof. Bernhard Weigand for all his help, support, advice and valuable remarks. I am especially indebted to Dr.-Ing. Xu Chu with whom I had several hours of long stimulating and fruitful discussions.

I am sincerely thankful to Prof. Claus-Dieter Munz and Dipl.-Ing. Fabian Föll for their cooperation with the CFD code Flexi. I also want to thank Dr.-Ing. Wanli Chang for his assistance in the development of machine learning based models. I extend my gratitude to Prof. Jörg Starflinger for his support during my stay at IKE. I would like to thank Mr. Corbinian Nigbur for proof-reading some parts and translating the abstract into German. I am grateful to my colleagues at IKE who provided a healthy work environment which was equally necessary.

This study would not have been possible without the generous fellowship from the Forschungsinstitut für Kernenergie und Energiewandlung (KE) e.V. Stuttgart, Germany. I would also like to acknowledge High Performance

Computing Center (HLRS), Stuttgart for the computational resources. I also extend my sincere gratitude towards the country and the people of Germany that welcomed me with open arms.

I would also like to thank all my friends for their positive comments and support throughout the study period. In the end, I heartily thank my loving parents and my sister for their care and affection. Their encouragement and support have helped me to strive for success.

Abstract

The power cycle based on supercritical carbon dioxide technologies promises a higher thermal efficiency and a compact plant layout. However, heat transfer and hydraulic characteristics are peculiar in the near-critical region due to the sharp variation of thermophysical properties in a narrow temperature and pressure range. Therefore, this works presents the results of several direct numerical simulations (DNS) of turbulent wall-bounded flow at supercritical pressure. The spatially developing pipe flows are simulated with the low Mach number approximation to characterize the cooling process of supercritical carbon dioxide. The upward and downward flow of carbon dioxide in vertical orientation has been considered. Heat transfer deterioration followed by recovery is observed in the downward flow while enhancement occurs in the upward flow as compared to forced convection. During the heat transfer deterioration, sweep and ejection events are decreased greatly, triggering the reduction in turbulence. The recovery in turbulence is brought by the Q_1 and Q_3 (also known as outward and inward interaction) events, contrary to the conventional belief about turbulence generation. The turbulence anisotropy of the Reynolds stress tensor showed that the turbulence structure becomes rod-like during the deteriorated heat transfer regime in the downward flow and disc-like for the upward flow. In addition to low Mach number DNS, a framework for using fully-compressible discontinuous Galerkin spectral element method for DNS of supercritical carbon dioxide is presented. A turbulent channel flow is considered to demonstrate the ability of this framework and to observe the

effects of Mach number in the supercritical fluid regime. The increase in the Mach number increases the turbulence in the flow for a given Reynolds number. Finally, a computationally light data-driven approach for heat transfer and hydraulic characteristics modeling of supercritical fluids is presented based on the deep neural network. This innovative approach has shown remarkable prediction capabilities.

Zusammenfassung

Der auf der Technologie überkritischen Kohlenstoffdioxids basierende Leistungszyklus verspricht einen höheren thermischen Wirkungsgrad bei gleichzeitig kompakterem Anlagenlayout. In einem engen Temperatur- und Druckbereich nahe des kritischen Punktes unterliegen Wärmeübertragung und hydraulischen Eigenschaften jedoch einer starker Variation aufgrund sich verändernder thermophysikalischen Eigenschaften. Daher präsentiert diese Arbeit die Ergebnisse mehrerer Direkter Numerischer Simulationen (DNS) turbulenter wandgebundener Strömungen bei überkritischem Druck. Die sich räumlich entwickelnden Rohrströmungen werden mit der „low Mach number"-Approximation simuliert , um den Abkühlungsprozess von überkritischem Kohlendioxid zu charakterisieren. Sowohl Aufwärts- als auch Abwärtsströmung von Kohlendioxid in vertikaler Ausrichtung werden berücksichtigt. Bei Abwärtsströmung tritt eine Verschlechterung der Wärmeübertragung, gefolgt von einer Erholung derselben, auf, wohingegen bei Aufwärtsströmung eine Verbesserung gegenüber erzwungener Konvektion beobachtet werden kann. Während der Verschlechterung der Wärmeübertragung werden Sweep- und Ausstoßereignisse stark reduziert, wodurch die Turbulenz verringert wird. Die Erholung der Turbulenz wird durch die Ereignisse Q_1 und Q_3 (bekannt als Interaktion nach außen und innen) hervorgerufen. Die Turbulenzanisotropie des Reynolds-Spannungstensors zeigt, dass die Turbulenzstruktur beim verschlechterten Wärmeübertragungsregime für die Abwärtsströmung stabförmig und für die Aufwärtsströmung scheibenförmig wird. Neben der

Low Mach-Zahl DNS wird ein Rahmen für die Verwendung einer vollständig komprimierbaren diskontinuierlichen Galerkin-Spektralelementmethode für DNS von überkritischem Kohlendioxid vorgestellt. Um die Fähigkeit dieses Gerüsts zu demonstrieren und die Auswirkungen der Mach-Zahl im überkritischen Flüssigkeitsbereich zu beobachten, wird eine turbulente Kanalströmung betrachtet. Die Erhöhung der Mach-Zahl steigert die Turbulenz im Fluss für eine gegebene Reynolds-Zahl. Schließlich wird ein rechnerisch günstiger, datengestützter Ansatz zur Modellierung der Wärmeübertragung und der hydraulischen Eigenschaften von überkritischen Fluiden basierend auf einem tiefes neuronalen Netzwerk vorgestellt. Dieser innovative Ansatz zeigt bemerkenswerte Vorhersagefähigkeiten.

Table of contents

Nomenclature

Roman Symbols

C	contribution to skin friction coefficient
c_p	isobaric specific heat capacity, kJ/(kg·K)
D	diameter, m
f	friction factor
G	mass flux, kg/(m^2·s)
g	acceleration due to gravity, m/s^2
H	channel half width, m
h	specific enthalpy, kJ/kg
k	turbulent kinetic energy, kg/(m·s^2)
L	length, m
N	contribution to Nusselt number
p	pressure, Pa
P_k	turbulence production due to shear, kg/(m·s^3)

Q	Quadrants
q	heat flux, W/m^2
R	radius, m
r, θ, z	cylindrical coordinates
s	specific entropy, kJ/(kg·K)
T	temperature, K
t	time, s
T_k	turbulent diffusion, kg/(m·s^3)
u, U	velocity, m/s
u_τ	friction velocity, m/s
V_k	viscous diffusion, kg/(m·s^3)
x, y, z	Cartesian coordinates

Greek Symbols

α	thermal diffusivity, m^2/s
β	thermal expansion coefficient, 1/K
ε	dissipation, kg/(m·s^3)
κ	thermal conductivity, W/(m^2·K)
λ	eigenvalue of a tensor
μ	dynamic viscosity, Pa·s
ν	kinematic viscosity, m^2/s

Π_k pressure diffusion, kg/(m·s^3)

ρ density, kg/m^3

τ shear stress, Pa

Superscripts

$+$ non-dimensional quantity

cum cumulative

Subscripts

0 inlet

b bulk

c critical

min minimum

pc pseudo-critical

w wall

DNN deep neural network

DNS direct numerical simulations

max maximum

rms root mean square

Dimensionless Numbers

Bo Buoyancy number

Gr Grashof number

Ma	Mach number
Nu	Nusselt number
Pr	Prandtl number
Re	Reynolds number

Chapter 1

Introduction

1.1 Motivation

Access to affordable and modern energy resources directly contributes to the economic and social growth and simultaneously minimizes the poverty which is the first Sustainable Development Goal set by the United Nations in 2015. A report from the International Energy Agency [6] claims that approximately 1.1 billion population globally lacks electricity supply as of 2016. As the global population is on the rise, this will certainly increase the global energy need. As per the International Energy Outlook 2017 [5], world energy consumption will grow by 28% between 2015 and 2040 due to the rapid urbanization, strong economic growth, digitization, and increased mobility. The current energy sector contributes roughly two-thirds of the total anthropogenic greenhouse gas (GHG) emissions. To limit the global temperature rise due to GHG, 195 countries signed the historic Paris Agreement at the Conference of the Parties of the United Nations Framework Convention on Climate Change (UNFCCC) with the long-term goal to limit the increase in global average temperature to well below 2°C above pre-industrial levels; and to limit the increase to

1.5°C. To achieve these goals, every nation needs a massive transformation in the energy sector combined with the environmentally-conscious decisions. Renewable energy technologies (RET) are becoming cost-effective and competitive to the fossil fuels. Nonetheless, RET suffers from the reliability of the supply due to its dependence on the local weather conditions. Therefore, an energy mix of renewable and fossil fuels will continue and help the policy-makers to meet the goals of the Paris agreement. In addition, fossil fuel power plants assist the integration of renewable energy into the grid by providing a backup in non-favorable conditions. Another alternative is nuclear power which has a similar life-cycle GHG emission as of RET. In addition, technological advancements in terms of efficiency increment of existing power cycles also have a huge potential to curb down the GHG emissions. It is highly desirable to utilize the energy resources in a most efficient way.

In the quest for efficiency enhancement in energy conversion, supercritical fluids are attractive options. A supercritical fluid is identified as a substance at a temperature and pressure above its critical point. A critical point denotes a point on the phase diagram at which phase equilibrium occurs. At the liquid-vapor critical point, a liquid and its vapor can coexist and surface tension of the liquid vanish. Below the critical point, a finite amount of heat is needed to convert a liquid into its vapor which is known as 'latent heat of vaporization'. The latent heat becomes zero at the critical point. Above the liquid-vapor critical point, a substance can be transformed without the phase transition. Schuster et al. [118] have investigated the supercritical Organic Rankine Cycle (ORC), which primarily use the low-temperature heat sources (such as geothermal energy, solar desalination, and waste heat recovery) and supercritical organic fluids. The thermal efficiency was improved by more than 8%, compared with the subcritical state. Chen et al. [26] have proposed a supercritical Rankine Cycle (SRC) based on zeotropic mixture working fluids, which shows 10-30% enhancement in the thermal efficiency over the conventional subcritical ORC. In addition, Zhang and Yamaguchi [133] have shown that a solar thermal collector based on supercritical carbon dioxide

(sCO_2) achieves an annually-averaged collector efficiency of 60%, which is much higher than that of a normal water-based solar collector. It has been found by Zhang and Yamaguchi [132] that the power generation efficiency of the solar Rankine cycle using sCO_2 is in the range of 8.78-9.45%, higher than the value 8.20% of the solar cell.

The applications of the supercritical fluids are not limited to the low-temperature heat sources. The idea of using supercritical fluids in the power plants has been intensively explored since the 1960s [72]. The supercritical and ultra-supercritical coal-fired power plants have shown superiority over their subcritical counterparts. Various advanced technologies can be coupled to these supercritical power plants to increase the efficiency as well as to reduce carbon emissions [114, 137, 23]. Moreover, the Supercritical Water-Cooled Reactor (SCWR) is one of the nuclear reactor candidates suggested by Generation-IV International Forum (GIF) with the aim of improving the thermal efficiency of power cycles by increasing the reactor's outlet temperature (ranging from 500 to 1000°C) [117]. It is estimated that the SCWR is able to achieve a thermal efficiency of about 45%, compared to about 33% for the current Light Water Reactor (LWR) [111]. In addition to the land-based power plants, the SCWR is expected to be used in marine vessels (ships and submarines) as well. The water used as a coolant is compatible with the operating environment of the vessels. The main advantages of using supercritical water are the compact design of heat exchangers, elimination of the dry-out problem, exclusion of steam separators, high power density, a smaller core, and better fuel economy [21]. However, structural material may degrade under high temperature and extremely corrosive environment, and power plant is prone to accidents along with a shorter lifespan. To circumvent this problem, supercritical carbon dioxide (sCO_2) is one of the alternatives. It can operate in the mid-temperature range (450 to 700°C) and improve the plant reliability [3].

Apart from power generation application, supercritical fluids are extensively used in various other applications for e.g. supercritical hydrogen and

methane are used as fuel for supersonic transport, supercritical carbon dioxide is used as refrigerant for air-conditioners and refrigerators, supercritical water is used as working fluid in ultra-supercritical fossil fuel power plants and oxidizer for waste treatment, other supercritical fluids are widely used for the processing of macromolecules and bioactive compounds, transformation of geothermal energy, pharmaceutical industries, high-pressure sterilization, jet cutting, and thin-film deposition for microelectronics [106, 38]. The trend of using carbon dioxide as working fluid is increasing because it is natural, harmless, and non-ignitable fluid, and it has 0 Ozone depletion potential (ODP) and 1 Global warming potential (GWP).

From the power generation perspective, lower critical pressure and temperature of carbon dioxide (p_c=7.38 MPa, T_c= 304.25 K) as compared to water (p_c=22.06 MPa, T_c= 674.09 K) provide an opportunity to generate electricity in a reduced operating range. The supercritical carbon dioxide Brayton cycle takes advantage of a lower fluid compressibility in the near-critical region and higher turbine inlet temperate resulting in higher cycle efficiency. In this way, sCO_2 Brayton cycle combines the advantages of both the steam Rankine cycle and gas turbine cycle. There exist several plant layouts with carbon dioxide as the working fluid, including single and split flow layouts with the options of precompression, recuperation, intercooling, and reheating [36]. Among all these layouts, the recompression layouts have shown great potential in terms of superior thermal efficiency, compactness, and simplicity [3].

In a typical recompression Brayton cycle, isobaric heat addition takes place at high pressure as shown by process 2-3-4-5 in Figure 1.1, which is far away from the critical point (in the range of 20 to 25 MPa) and heat rejection takes place in the near-critical pressure (7.5 to 10 MPa) as depicted by process 6-7-8-1. The flow is split at point 8, and the major part of the fluid is cooled down in the reject heat exchanger (i.e. pre-cooler) in process 8-1. The fluid is compressed isentropically in the compressor (process 1-2) and recompressor (process 8-3). During process 2-3, the major part of the split fluid is heated in the low-temperature recuperator and at point-3; it is mixed

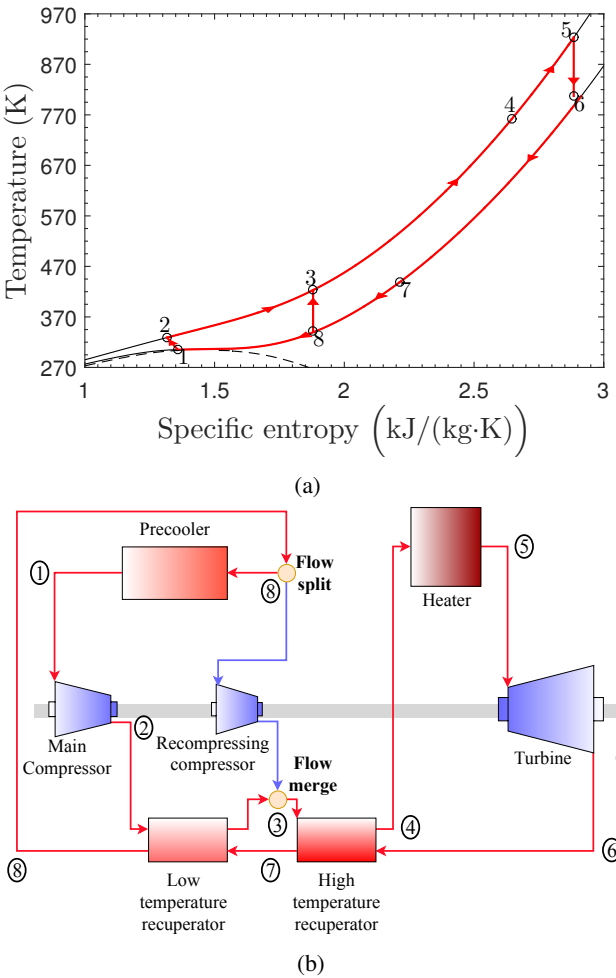

Fig. 1.1 Recompression Brayton Cycle (a): T-s diagram and (b): cycle layout

up with the fluid coming from the recompressor. Then the fluid is sent to the high-temperature recuperator (process 3-4), where it extracts the heat from

the fluid at the low-pressure side (process 6-7). The remaining part of the heat is supplied via an external source (such as nuclear fission, solar thermal, geothermal, waste heat) during the process 4-5. The isentropic expansion from high-pressure to low-pressure takes place in the turbine in process 5-6 and fluid is passed through the high and low-temperature recuperator for the regeneration purpose. The heat exchanger and other equipment in the power cycle are subjected to wall-bounded turbulent flow, where at least one wall is present with the no-slip boundary conditions. The completely confined flow in the channel and pipe will result in the turbulent boundary layers [15]. This turbulent boundary layer influences the flow significantly in the supercritical fluids with the heat transfer.

1.2 Literature Review

The idea of using supercritical fluid in thermal power plants is in existence since 1950s [138]. The claim of higher efficiency enticed the plant's owner which led to research and development efforts for designing nuclear reactors using helium [106]. But, the problem of heat transfer deterioration and its prediction baffled the scientific community. In the power cycle shown in Figure 1.1, the variation of thermophysical properties is smooth at high pressure of 20-25 MPa, thus commonly used correlations for linearly-varying properties can be applied to predict the heat transfer. The problem of an accurate and reliable prediction of heat transfer arises at the lower pressure of 7.5-10 MPa, where almost all thermophysical properties change abruptly with temperature as shown in Figure 1.2. The fluid can neither be identified as a liquid nor a gas in the vicinity of the critical point. This narrow region is often known as the near-critical region. When a fluid is heated in the near-critical region then it can undergo a transition from liquid-like state to gas-like state (vice versa for cooling), and these states are separated by a coexistence line, commonly known as the Widom line [16]. When crossing the Widom line, a sharp cross-over of different thermophysical properties

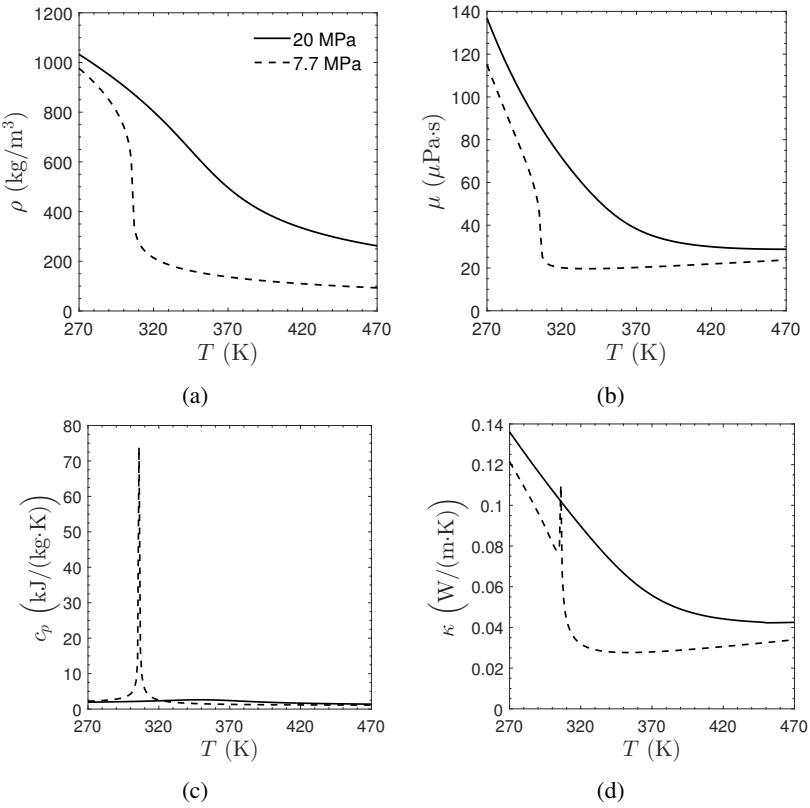

Fig. 1.2 Variation of (a): density, (b): dynamic viscosity, (c): isobaric specific heat capacity and (d): thermal conductivity with the temperature [81]

takes place. In the near-critical region, thermophysical properties change significantly in a narrow temperature range. The specific heat capacity shows its maximum at the pseudocritical temperature and its location (with respect to p and T) is represented as a point on the Widom line. This strong variation in thermophysical properties causes unusual heat transfer behavior compared to subcritical conditions and it can include heat transfer enhancement and/or

deterioration depending upon the type of the heat transfer (i.e. cooling or heating) and flow direction [13, 64]. The heat transfer deterioration will not only reduce the efficiency but can also lead to a catastrophic accident. Therefore, it is essential to predict heat transfer behavior, so that engineers can circumvent this problem of heat transfer deterioration in advance. Numerous efforts have been made to address this issue by means of experiments and numerical methods.

1.2.1 Experimental studies

Simple geometries such as circular pipes or annular channels have been used to investigate the heat transfer experimentally in the vicinity of the pseudo-critical temperature. Schmidt et al. [52] made the first experimental investigation in 1946 for the heat transfer at natural convection in a liquid near its critical state. They discovered that the heat transfer is enhanced at the near-critical point and focused on single-phase thermosyphons [107]. Shitsman [124, 125] conducted experiments with upward flowing supercritical water and noticed impairment of the heat transfer at high heat flux. Several other authors have carried out the experimental analysis of heat transfer to supercritical water [2, 50, 54, 71, 78, 135]. Due to the scaled down properties of sCO_2, it is relatively easy to handle the fluid in a laboratory. Therefore, recent studies are made the CO_2.

Shiralkar and Griffith [123] performed experiments with carbon dioxide in the near-critical region. They first reported that deteriorated heat transfer can occur with high heat fluxes at supercritical pressure as long as the bulk temperature is below the pseudocritical temperature. Almost after 35 years, Kim and Bae extensively investigated the heat transfer to sCO_2 by means of experiments [68, 13, 14]. They have conducted a series of experiments in the pressure range of 7.75 MPa to 8.85 MPa with different mass and heat flux combinations. They observed the heat transfer deterioration as a wall-temperature peak at high heat flux and low mass flux when the fluid

properties changed drastically. In the experiments of Kim and Kim [67], similar observations of heat transfer deterioration were observed in the upward flow of sCO_2 while in the downward flow, the wall temperature increased monotonically without any peak. The authors concluded that different nature of wall temperature distribution is due to the relationship between the flow direction and buoyancy force in the near-wall region. Xu et al. [134] used an infrared thermometer to obtain the continuous wall temperature for a vertically-oriented mini tube. The authors have observed the abnormal heat transfer in their experiments and verified the previously reported effects of heat flux and flow direction. There are comparatively few investigations which have been conducted for cooling of the fluid.

Tanaka et al. [128] investigated the cooling phenomenon for the first time. They compared the heating and cooling of the sCO_2. An experimental analysis of the heat transfer and pressure drop associated with in-tube cooling of supercritical carbon dioxide was conducted by Pitla et al. [108] at various flow rates with the aim of gas cooler design. Dang and Hihara [33] also conducted experiments in which sCO_2 was cooled in circular tubes. They summarized from their parametric study that the heat transfer coefficient and pressure drop increase with increasing mass flux. Jiang et al. [64] investigated the heat transfer in a vertical cooled tube by means of experiments. An important observation from their study was heat transfer enhancement for upward flow and deterioration followed by recovery for downward flow. Liu et al. [84] developed a test loop to analyze the flow and heat transfer behavior in the horizontal orientation and presented a parametric study by varying different variables in the experiment such as mass flow, pipe diameter, inlet pressure, and temperature. Zhang et al. [139] characterized the in-tube cooling for four horizontal tubes with variations in tube diameter, mass flux, and pressure. Wang et al. [131] found that the heat transfer coefficient in the horizontal helically coiled tube is higher than that of the vertical helically coiled tube. Due to the revival of supercritical power cycles, many recent studies are focused towards the supercritical carbon dioxide [83, 79, 44].

Typically, experiments with sCO_2 require high financial resources along with longer time to build them. Moreover, a limited amount of qualitative data is available for e.g. wall temperature and pressure drop. These data serve for preliminary identification of heat transfer peculiarity. However, most of the time, they failed to deliver insight information regarding the flow. In this scenario, numerical studies are useful.

1.2.2 Numerical studies

Besides experiments, numerical methods are also useful. Figure 1.3 depicts the available options for the heat transfer prediction for supercritical carbon dioxide. Correlations and analytical models are the simplest and fastest way to compute the heat transfer coefficient. Most of these correlations are derived from a particular experimental dataset. There are a number of correlations available in the literature for both constant and linearly varying properties. A commonly used correlation given by Gnielinski is given by Equation 1.1, which couples the friction and heat transfer, and provides excellent predictions for constant properties flow.

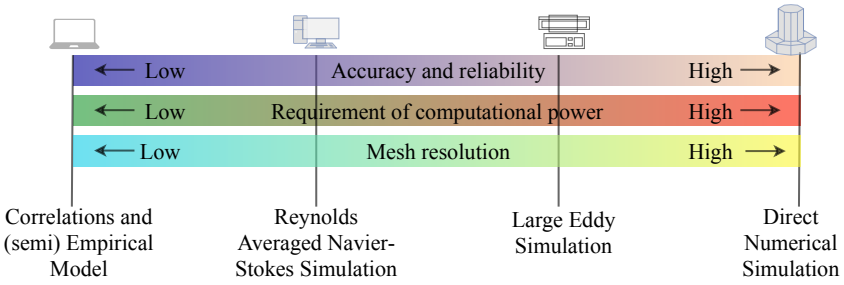

Fig. 1.3 A spectrum of numerical prediction methods for sCO_2 for a given Reynolds number and geometry

$$\mathrm{Nu_b} = \frac{\frac{f}{8}(\mathrm{Re_b} - 1000)\mathrm{Pr}}{1 + 12.7(\frac{f}{8})^{1/2}(\mathrm{Pr}^{2/3} - 1)} \tag{1.1}$$

where

$$f = [0.79\ln(\mathrm{Re_b}) - 1.64]^{-2}$$

Several specific correlations have been proposed to treat the steep variation in the thermophysical properties of supercritical fluids [89, 20, 125, 74, 19, 60, 59]. Cheng et al. [27] reviewed the experimental data of heat transfer and pressure drop while focusing on the use of sCO_2 as a refrigerant. They compared various correlations with experimental data but no correlation was found to cover a wide operation range. A detailed comparative analysis is performed by Pioro et al. [106], showing that most of the correlations are only able to predict the qualitative rough trend, yet not the actual magnitude. Based upon this study, three correlations targeting the supercritical fluids, as given by Equations 1.2, 1.3 and 1.4 are selected for comparison. Equation 1.2 shows one of the earliest correlations proposed by Miropol'skii and Shitsman [92] in late 1950s.

$$\mathrm{Nu_b} = 0.023\mathrm{Re_b^{0.8}Pr_{min}^{0.8}} \tag{1.2}$$

The correlation given by Equation 1.3 is derived by Krasnoshchekov and Protopopov [74] and the correlation in Equation 1.4 is from Jackson [59].

$$\mathrm{Nu_b} = \mathrm{Nu_0}\left(\frac{\mu_\mathrm{b}}{\mu_\mathrm{w}}\right)^{0.11}\left(\frac{\kappa_\mathrm{b}}{\kappa_\mathrm{w}}\right)^{-0.33}\left(\frac{\overline{c_p}}{c_{p\mathrm{b}}}\right)^{0.35}, \tag{1.3}$$

where

$$\mathrm{Nu}_0 = \frac{\frac{\xi}{8}\mathrm{Re}_\mathrm{b}\overline{\mathrm{Pr}}}{12.7\frac{\xi}{8}(\overline{\mathrm{Pr}}^{2/3}-1)+1.07},$$

$$\overline{c_p} = 0.5(c_{p\mathrm{b}} + c_{p\mathrm{w}}),$$

$$\overline{\mathrm{Pr}} = 0.5(\mathrm{Pr}_\mathrm{b} + \mathrm{Pr}_\mathrm{w}),$$

$$\xi = [1.82\log_{10}(\mathrm{Re}_\mathrm{b}) - 1.64]^{-2}.$$

$$\mathrm{Nu}_\mathrm{b} = 0.0183\mathrm{Re}_\mathrm{b}^{0.82}\mathrm{Pr}_\mathrm{b}^{0.5}\left(\frac{\rho_\mathrm{w}}{\rho_\mathrm{b}}\right)^{0.3}\left(\frac{\overline{c_p}}{c_{p\mathrm{b}}}\right)^{n}, \tag{1.4}$$

where

$$n = \begin{cases} 0.4, & T_\mathrm{b} < T_\mathrm{w} < T_\mathrm{pc} \cup 1.2T_\mathrm{pc} < T_\mathrm{b} < T_\mathrm{w} \\ 0.4 + 0.2(\frac{T_\mathrm{w}}{T_\mathrm{pc}} - 1) & T_\mathrm{b} < T_\mathrm{pc} < T_\mathrm{w} \\ 0.4 + 0.2(\frac{T_\mathrm{w}}{T_\mathrm{pc}} - 1)(1 - 5(\frac{T_\mathrm{b}}{T_\mathrm{pc}} - 1)) & T_\mathrm{pc} < T_\mathrm{b} < 1.2T_\mathrm{pc} \cup T_\mathrm{b} < T_\mathrm{w} \end{cases}$$

A relatively new correlation from Kim and Kim [67] is proposed by Equation 1.5, which was derived for vertical upward and downward flow of supercritical pressurized fluid.

$$\mathrm{Nu}_\mathrm{b} = 2.0514\mathrm{Re}_\mathrm{b}^{0.928}\mathrm{Pr}_\mathrm{b}^{0.742}\left(\frac{\rho_\mathrm{w}}{\rho_\mathrm{b}}\right)^{1.305}\left(\frac{\mu_\mathrm{w}}{\mu_\mathrm{b}}\right)^{-0.669}\left(\frac{c_{p,\mathrm{w}}}{c_{p,\mathrm{b}}}\right)^{0.888}(q^+)^{0.792}, \tag{1.5}$$

where

$$q^+ = \frac{q_w\beta_b}{Gc_{p,b}}$$

To asses their capability, a comparison between the experiments of Kim et al. [68] and selected four correlations is illustrated in Figure 1.4. The prediction capability at normal heat transfer is acceptable. However, a mismatch

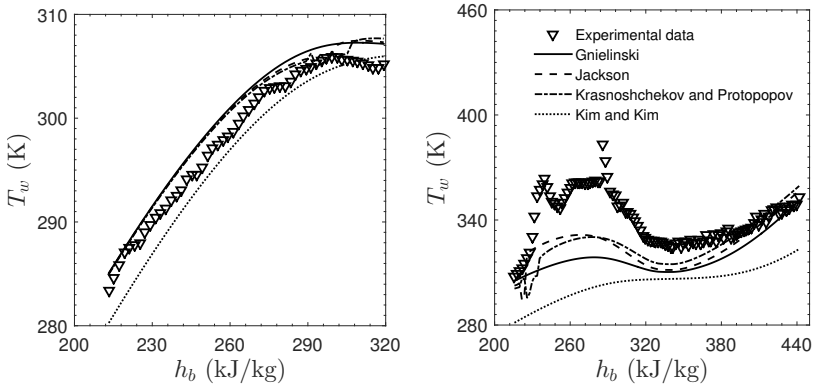

Fig. 1.4 A comparison of selected correlations with the experimental data of Kim et al. [68] for vertical heated flow of CO_2 at a pressure of 7.7 MPa and a mass flux of 400 kg/(m^2·s). (a): Normal heat transfer (q_w=10 kW/m^2) and (b): Deteriorated heat transfer (q_w=50 kW/m^2)

can be seen at deterioration. This is the main constraint with the correlations that they are experimental-data specific and lose their generality in peculiar heat transfer. An alternative to correlation is the analytical model. Laurien [75] derived an implicit model to predict the heat transfer at supercritical pressure by utilizing the two-layer theory. The author introduced correction factors to improve the agreement. However, the model was not universal, because correction factors were not based on the physical understanding of the flow. Jackson [61] proposed a semi-empirical model for heat transfer to the supercritical fluid which includes the effect of buoyancy and acceleration. The semi-analytical models are 'tuned' with the experiments, hence generality is far beyond the reach at the moment.

The Reynolds-averaged Navier–Stokes (RANS) simulation, in which turbulence is 'modeled', is at the next level of the spectrum shown in Figure 1.3. Numerous attempts have been made in the past to model the heat transfer to

sCO_2 by means of turbulence modeling [120, 136, 56, 110]. He et al. [56] assessed low-Reynolds number turbulence models and found that models either over-predict or under-predict the heat transfer depending upon their damping function characteristics with respect to buoyancy and flow acceleration. Analogous observations were reported by Sharabi et al. [120]. In addition to this, authors reported that the Renormalization Group (RNG) k—ε model with a two-layer treatment of the near-wall region was not able to reproduce experimental results. Pucciarelli and Ambrosini [109] made an attempt to improve Reynolds-averaged Navier-Stokes (RANS) turbulence models. In this work, they incorporated an algebraic heat flux model as an auxiliary tool to calculate the turbulent Prandtl number distribution. This distribution was further used in the energy equation. Through this, buoyancy induced phenomena were captured up to an extent but it was not general for further application with certainty. Therefore, it can be concluded that CFD studies with turbulence models are not reliable at supercritical pressure. Du et al. [37] investigated the heat transfer in a horizontal tube numerically and showed that many turbulence models were able to reproduce heat transfer variation qualitatively but not quantitatively. Cao et al. [22] focused on laminar mixed convection in a horizontal miniature tube of a hydraulic diameter less than 1 mm. As a result of buoyancy, a secondary flow was developed contributing to better heat transfer. Liao and Zhao [82] numerically investigated the heat transfer to sCO_2 in mini and microtubes. In their analysis, both cooling and heating was investigated while considering only laminar flow. All the flow and heat transfer characteristics were affected by large variations of the thermophysical properties even in the laminar region.

However, direct numerical simulation (DNS) is an attractive alternative to overcome this difficulty at low Reynolds numbers. DNS not only provides a high-fidelity approach but also it has the ability to deliver insight into the turbulent flow. Due to the high accuracy, DNS is often termed as ‘numerical experiments’. Bae et al. [9] performed the first DNS of heated pipe flow for supercritical carbon dioxide. In their exemplary work, authors presented a

framework for DNS using the low Mach number Navier-Stokes equations. They developed an in-house, second-order accurate code based on the finite difference method. Various flow conditions were simulated and they correspond to variations in the heat flux, tube diameter, gravity, and flow direction. The authors observed heat transfer deterioration in upward flow and enhancement during downward flow conforming the trends discussed in Section 1.2.1. Nemati et al. [94] also accomplished DNS while focusing on three cases from Reference [9]. They illustrated that reduction of the turbulent kinetic energy (TKE) leads to heat transfer deterioration. They further explained that averaged thermophysical properties differ from that evaluated at mean temperature or enthalpy due to the Jensen inequality. It was an important remark which explains the inability of turbulence modeling to capture the heat transfer at supercritical pressure. Nemati et al. [95] further studied the effect of thermal boundary conditions on heat transfer. They illustrated that heat transfer to supercritical fluids strongly depends of the thermal wall boundary condition when the momentum diffusivity is equal or greater than the thermal diffusivity (i.e. Prandtl number, $\mathrm{Pr} \geq 1$). Chu and Laurien [31] performed a DNS for a horizontally-oriented pipe, in which the gravity force affected the heat transfer in the transverse direction. They analyzed the heat transfer and documented a secondary flow causing flow stratification. This flow stratification induced a higher wall temperature at the top compared to the bottom of the pipe. Bae et al. [10] and Peeters et al. [102] investigated the heat transfer in an annulus with different thermal boundary conditions imposed at the wall. When the inner wall was heated and the outer wall is cooled such that pseudocritical temperature lies close the inner wall then the streak coherency decreased near to the hot wall along with the reduction in streamwise vortices [102]. Due to variable properties in the near-critical region turbulence becomes anisotropic [10]. He et al. [55] investigated the effect of a streamwise body force and provided a new perception for the flow relaminarization. They have categorized the body-force aided flow into three regimes: (1) partially laminarized, (2) fully laminarized and (3) recovering

flows based upon velocity profile and turbulent kinetic energy distribution. The body force influenced the near-wall turbulence structure in terms of sweep and ejection events. Thus, there can be a plethora of interlinked reasons for incapabilities of turbulence modeling and they all are directly or indirectly connected to the role of turbulence. Therefore, it is very important to analyze the turbulence in such flows.

All the above mentioned investigations were based on the low Mach number approximation which decouples the acoustic interaction from the compressibility effects. In order to study the effect of compressibility in the trans- and supercritical region, fully-compressible simulations are necessary. Kawai [65] conducted a direct numerical simulation of heated transcritical boundary layers with zero pressure gradients under supercritical conditions. The effects of compressibility were significant in transcritical flow even at low Mach numbers. Recently, Sengupta et al. [119] performed a fully compressible DNS at low Mach numbers for channel flow with a hot and cold wall. For the same, they deployed a finite-volume code using the Peng-Robinson (PR) equation of state (EoS). They showed that compressibility effects can exist in the near-wall region at low Mach numbers when the pseudo-critical temperature transition occurs near the cold wall. Ma et al. [87] used their entropy-stable hybrid scheme for DNS of turbulent channel flow under transcritical conditions with a hot and a cold isothermal wall and assessed the attached eddy model in the context of turbulence of variable thermodynamic properties. Kim et al. [70] also performed DNS for channel flow under transcritical temperature conditions with a hot and cold wall at a Mach number of 0.26. In their simulations, a fully compressible and fully conservative approach was used and they tackle the numerical instability problem via systematic grid refinement. These fully compressible DNS studies were conducted at low Mach numbers with PR as EoS by using a finite volume method. The PR-EoS is computationally less expensive but it deviates from the standard database such as REFPROP by NIST [81].

The DNS proved to be a reliable and accurate numerical tool, however, the main downside of the DNS is the heavy computational burden. While less computer intensive techniques (RANS and simple correlations) failed in the predictions, a relatively new methods based on the machine learning algorithm has shown a great potential. Machine learning is a broad term for statistical techniques which provide a computer to learn from the data. Deep neural networks (DNNs), a machine learning algorithm, have received overwhelming attention and demonstrated its capability in capturing the intrinsic relationships hidden in the data in numerous domains [115, 34], including fluid dynamics. A multi-layer feed-forward neural network has been developed and trained by Scalabrin and Piazza [113] for forced convection heat transfer to sCO_2. Experimental data for training and validation were extracted from 8 publications in the literature, including both horizontal and upward pipe orientation. The performance achieved by the neural network was comparable to well-known empirical correlations. Another neural network is proposed by Pesteei and Mehrabi [104] for calculating the heat transfer coefficient of sCO_2 in a vertical tube with the diameter of 2 mm. Unlike the significant turbulent regime [113], experimental results at low Reynolds numbers (Re$<$2500) from a single publication of Jiang et al. [63] are used for training and validation. The available data amount is considerably less than that of Pesteei and Mehrabi [113]. In a more recent paper [35], a neural network is trained with in-house experimental data for a supercritical boiler design. The authors report 100% prediction accuracy for the training data at a deviation level of $\pm 7^{\circ}$C, which drops to about 80% in the validation. The ability of DNN coupled with DNS is not fully exploited until now, which has a high potential in terms reducing computational efforts and better accuracy. Recently, Chang et al. [24] trained an artificial neural network (ANN) based on 5280 data points collected from published experimental data for supercritical water. The validation study (strictly separated from training) shows that the mean error percentage and its standard deviation were both below 0.5%. Furthermore, a series of tests, including operational conditions out

of the training and validation data, were performed in comparison with four well-established correlations. The results demonstrated that the performance of the ANN is considerably better than the correlations.

1.3 Thesis goals and outline

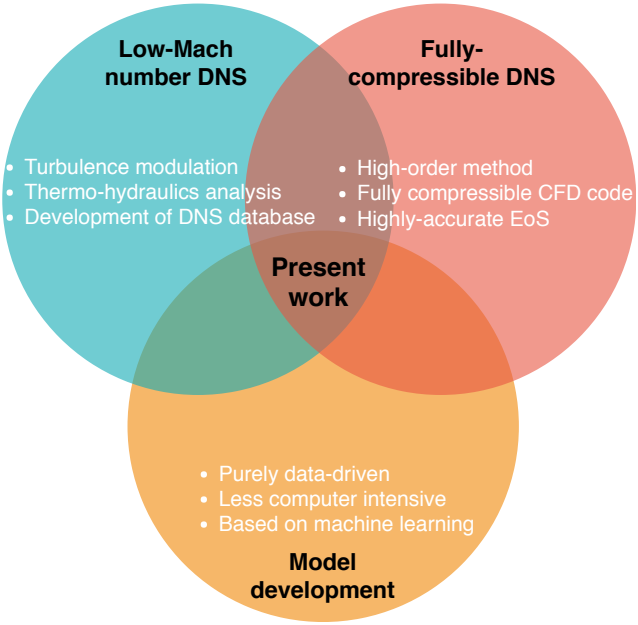

Fig. 1.5 Scope of the present thesis

From the above discussion, it becomes clear that heating of sCO_2 has gained much attention in the past compared with the cooling. As already pointed out, the heat-rejection process will take place in the near-critical region in the power loop. Therefore, it is equally important to analyze the cooling of sCO_2 in the near-critical region. Until now the possibility of heat transfer deterioration is known but the mechanism of it, is still unknown and

how it triggers during the cooling. There is not any high-fidelity simulation study available in the literature which is devoted to cooling of sCO_2 as per the best of author's knowledge. In addition, most of the DNS investigations are based on the low Mach number assumption and employ low-order methods. Therefore, a fully compressible, high-order, massively parallel framework is a necessity for DNS at relatively high Reynolds numbers. A computationally-cheap method is a foremost requirement for the power plant engineer which can capture the heat transfer abnormality at supercritical pressure. Based on these motivations, the objectives of the present work can be divided into the following broad categories (also shown in Figure 1.5):

- To characterize the heat transfer to supercritical carbon dioxide under cooling condition by means of DNS at low Mach numbers.
- To understand the role of turbulence in unusual heat transfer during cooling at supercritical pressure.
- To develop a high-order, fully compressible numerical framework for turbulent supercritical flow.
- To develop a less computer-intensive model for thermo-hydraulic predictions.

This thesis is divided into 6 chapters including the present one which introduced the problem and showing the research gap. Chapter 2 discusses the theoretical background along with the governing equations, numerical methods, and computational details. Two different solvers were used in this work, therefore, a brief description along with the verification of the solvers is discussed in Chapter 2. Chapter 3 thoroughly explains the results from the heat transfer characterization of the cooling process of sCO_2 which covers the first two objectives of this work. Different turbulent statistics were used for the discussion of heat transfer deterioration and enhancement. Chapter 4 covers the third objective by showing the capability of high-order CFD code for the DNS at supercritical pressure which also includes the effects of Mach number.

Chapter 5 presents a novel method to predict the heat transfer based on the machine learning approach by employing a big dataset generated from the DNS. In addition, Chapter 5 also includes details regarding the comprehensive DNS database developed in this work for the heating along with a parametric study. Finally, Chapter 6 provides a brief summary of the work followed by recommendations for future work. Additionally, two appendices are also provided which give an overview of the supplementary results from the DNS and details about the analytical model developed within the course of this work.

Chapter 2

Numerical and computational details for DNS

This chapter describes the numerical methods along with the mathematical model. The previous chapter gave a clear picture regarding the incapability of turbulence modeling applied to supercritical CO_2. Therefore, Direct Numerical Simulation (DNS), which is on the highest level of hierarchy in terms of accuracy, is adopted for this work. In DNS, the flow describing equations i.e. Navier-Stokes equations, are solved numerically without any turbulence model. Unlike RANS and LES, DNS resolves the spatial and temporal scales of the flow.

For DNS, several open source CFD codes are available. For this work, OpenFOAM [96], which is a C++ library, is selected. OpenFOAM is a well-established CFD code for DNS, used by several researchers for a variety of applications [28, 43, 53]. This CFD code is extended for the DNS of spatially developing pipe flow with the low Mach number assumptions. The Mach

number is defined as the ratio of bulk flow velocity to the local speed of sound. In addition, a new CFD code, named Flexi [57], is also extended for sCO_2. This code was specifically developed for fully-compressible LES/DNS, which overcome the low Mach number assumption. Chapter 2.1 includes the details about OpenFOAM (low Mach number DNS) and Chapter 2.2 describes the details about Flexi (fully compressible DNS). A brief description of the flow governing equations, their numerical implementation followed by boundary conditions and initialization is presented individually for both the codes along with the parallel performance on the high-performance computer (HPC).

2.1 Description of low Mach number simulation

For the spatially developing pipe flow simulations, OpenFOAM is selected as a solver. Several libraries were developed within the code for the investigation of turbulence modulation. This section describes the information for flow domain, low Mach number Navier-Stokes equations, numerical schemes, and the parallel performance.

2.1.1 Integration domain and boundary conditions

Figure 2.1a depicts the geometry of the pipe and the boundary conditions for the DNS with OpenFOAM. The computational domain consists of a straight pipe of the diameter D with a total length of $35D$ length. The pipe is divided into two parts for the numerical simulation. The initial length of $L_1 = 5D$ serves as an inflow generator with an isothermal wall. The objective of the inflow generator is to provide a fully developed turbulent flow to the main domain at every time step. Instead of the periodic boundary condition for this section, a recycling/rescaling procedure [86] has been adopted for the inflow generator, in which fields from a $L = 4D$ are internally mapped at the inlet at every time step. The velocity field was initialized with the perturbation

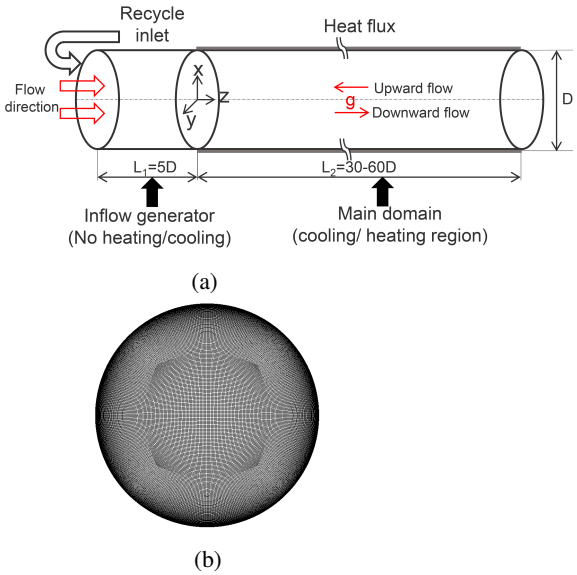

Fig. 2.1 Details for low Mach number DNS using OpenFOAM (a): geometry of the simulation domain and (b): cross-sectional view of the computational mesh on $x-y$ plane

method introduced by Schoppa and Hussain [116]. This method proved to be a computationally efficient way to get a fully developed turbulent flow [28].

The second section of the pipe, identified by L_2 in Figure 2.1a, is known as the main domain, it is distinguished from the inflow generator by a heat flux applied to the wall. The wall heat flux (q_w), was set negative to represents a cooling or heat rejection while for heating or heat addition, it was set positive. In the main domain, the no-slip boundary condition is imposed at the wall while a convective outflow boundary condition $\left(\partial\phi\partial t + U_c\partial\phi\partial x = 0\right.$, where ϕ can be any dependent variable, e.g. the velocity U $\left.\right)$ is employed for the velocity and other variables at the outlet. The distinction between upward and downward flow is made by changing the direction of gravity in the momentum

equation while the distinction between forced and mixed convection is made by omitting or including the gravity term in the momentum equation.

The mesh consists of a structured O-grid with five blocks filled with the hexahedral elements, as shown in Figure 2.1b. The cross-sectional mesh consists of one center block and four surrounding blocks. This arrangement circumvents the problem of coordinate singularity and cells concentration at the center of the pipe. The center block is uniformly divided into 90 cells and neighboring blocks are divided into 76 cells with an expansion ratio of 10. It results in approximately 120 cells in the radial direction and 360 cells in the circumferential direction. The inflow generator has a resolution of $120\times360\times300$ (radial r, circumferential θ and axial z direction). The main domain has an equivalent resolution of $120\times360\times1800$ for $30D$ length pipe. A uniform grid spacing is used in the axial direction, while the radial grid is refined close to the wall. It result in non-dimensional grid resolution 0.18 (wall) $\leq \Delta r^+ \leq 1.8$ (center), $(R\Delta\theta)^+$= 3.1 (centre) and Δz^+=6.0. The non-dimensional grid resolution is given in wall units defined by $\Delta y^+ = \Delta y u_{\tau,0}/\nu_0$. Here, R is the radius of the pipe, Δy is the size of the discretized cell in the respective coordinate direction, ν is the kinematic viscosity and u_τ is the friction velocity calculated as: $u_{\tau,0} = \sqrt{|\tau_{w,0}|/\rho_0}$. The wall shear stress (τ_w) is based on inlet Reynolds number $\left(\mathrm{Re}_0 = \frac{GD}{\mu_0}\right)$ of 5400 and is calculated as: $\tau_w = \frac{1}{8} f \rho U^2$, with the Darcy friction factor, $f = \frac{0.316}{Re^{0.25}}$. The subscript '0' stands for the parameters defined at the inlet/reference conditions of p_0= 8 MPa and T_0= 342.05 K. A comparison of mesh resolution of current DNS with similar DNS studies in the literature is shown in table 2.1 (where N is the number of cells/number of grid points). The present mesh resolution is comparable with previous DNS performed with supercritical fluids [31, 95, 94] and higher than Bae et al. [9] in all three directions. In addition, the study presented, treats cooling, in which the bulk Reynolds number decreases along the streamwise direction. This also lowers the requirement of fine mesh as compared to heating.

Table 2.1 Comparison of mesh resolution of current DNS with previous DNS in the literature

Case	N_r	N_θ	N_z	Δr^+	$(R\Delta\theta)^+$	Δz^+
Bae et al. [9]	69	129	769	0.18-5.34	9.14	14.55
Nemati et al. [95, 94]	128	288	1728	0.55-4.31	3.93	6.25
Chu et al. [31]	168	172	2400	0.11-1.1	6.5	4.6
Present	120	360	1800	0.18-1.8	3.1	6.0

2.1.2 Governing equations

A fluid flow problem is governed by the fully-compressible Navier-Stokes (N-S) equations. In this DNS, the low Mach number Navier-Stokes equations are used instead of the fully compressible N-S equations. It is assumed that during the heat transfer at supercritical pressure, the Mach number is very low so that acoustic interaction can be decoupled from compressibility effects. Whilst the effects of variable fluid inertia due to the heat transfer is accounted by this anelastic approximation [80]. Nemati et al. [94] have shown that during heating of sCO_2, the Mach number varies between 0.0011 to 0.0026 for the entire considered range of enthalpy, which warrants the low Mach number assumption. The aforementioned assumption was also employed in previous DNS as well, e.g. by Bae et al. [9, 10], Nemati et al. [94, 95] and Chu et al. [31, 30]. The following Equations (2.1), (2.2) and (2.3) represent the mass, momentum and energy conservation in which a vector and a tensor is denoted by a bold symbol. Readers are advised to see the work of Nemati et al. [94] for a detailed derivation of low Mach number Navier-Stokes equations.

$$\frac{\partial \rho}{\partial t} + \nabla \cdot (\rho \mathbf{u}) = 0 \tag{2.1}$$

$$\frac{\partial \rho \mathbf{u}}{\partial t} + \nabla \cdot (\rho \mathbf{u}\mathbf{u}) = -\nabla p + \nabla \cdot (2\mu \mathbf{S}) \pm \mathbf{b_f} \tag{2.2}$$

$$\frac{\partial \rho h}{\partial t} + \nabla \cdot (\rho \mathbf{u} h) = \nabla \cdot (\kappa \nabla T) \tag{2.3}$$

In Equations (2.1)-(2.3), ρ denotes the fluid density, $\mathbf{u}$ is the velocity vector, p is the pressure, μ represents the dynamic viscosity, h is the specific enthalpy, κ is the thermal conductivity and T denotes the temperature. The $\mathbf{b_f}$ is the body force due to gravity and its value is $[0,0,\rho g]^{\mathrm{T}}$, $\mathbf{S}$ represents the strain tensor given by $\frac{1}{2}[(\nabla \mathbf{u} + (\nabla \mathbf{u})^{\mathrm{T}}) - \frac{2}{3}(\nabla \cdot \mathbf{u})\mathbf{I}]$ with $\mathbf{I}$ as the identity matrix.

In the limits of low Mach number flows, the thermodynamic pressure is considered to be constant while the fluctuations of the hydrodynamic pressure are assumed to be very small compared to the thermodynamic pressure so that all thermophysical property variations due to hydrodynamic pressure fluctuations can be neglected. Therefore, all thermophysical properties can be evaluated as a function of the enthalpy only [102]. Thermophysical properties can be evaluated by directly calling the standard database such as NIST REFPROP [81] or by creating a look-up table. However, both methods are computationally expensive and they slow down the computation due to the communication overhead. Therefore, here, thermophysical properties are implemented by 3^{rd} order piecewise spline functions. These properties were derived from NIST REFPROP [81]. Figure 2.2 depicts a comparison between the implemented spline function with the standard database by NIST for a pressure of 8 MPa. The error bound of the derived spline function and the NIST database was within $\pm 1\%$ for all thermophysical properties. This approach gives a significant speedup (up to a factor of 2.5) compared to directly using the database. Equation (2.4) shows the functional relationship between enthalpy and different thermophysical properties at a reference pressure (p_0).

$$h = h(p_0,T), T = T(p_0,h), \rho = \rho(p_0,h), \mu = \mu(p_0,h), c_p = c_p(p_0,h), \kappa = \kappa(p_0,h) \tag{2.4}$$

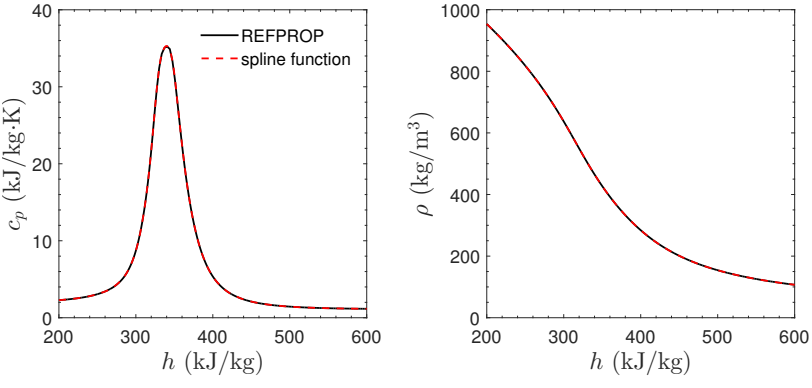

(a) (b)

Fig. 2.2 Comparison of implemented spline function with the NIST REFPROP [81] at a reference pressure (p_0) of 8 MPa. (a): Isobaric specific heat capacity and (b): density

2.1.3 Numerical schemes

A brief description of spatial and temporal discretization along with the numerical solution procedure is presented in this section. For solving the governing equations described in Section 2.1.2, the finite volume method is chosen. As the numerical solver, the open source finite volume code OpenFOAM (v2.4 and v5.0) [96] was extended accordingly. The temporal discretization is performed with a backward scheme, which is an implicit, second order and conditionally stable scheme. For the spatial discretization, a second order scheme is selected. The gradient, divergence, and Laplacian schemes were handled by the standard finite volume discretization of Gaussian integration with linear interpolation from cell centers to face centers. Thus, the code is overall second order accurate in both space and time. The Pressure-Implicit with Splitting of Operators (PISO) algorithm [58], which is a non-iterative method, was applied to couple the pressure and velocity terms in the momentum equation. The code solves the equations in Cartesian coordinates;

transformation to the cylindrical coordinate system was performed for post-processing.

2.1.4 Verification of the code

The numerical method is verified with recently available DNS data of Khoury et al. [40] for a fully developed constant property pipe flow. They used a high-order spectral element code based upon Galerkin approximation with 18.6×10^6 grid points. The inlet Reynolds number was 5300, which slightly differs from the presented DNS which is 5400. A comparison is made with the root mean square (rms) velocity and budget of the transport equation of the TKE budget. Equation 2.5 shows the transport equation of the TKE budget, in which k is the TKE, P_k is the turbulence production, ε is the dissipation, Π_k is the pressure diffusion, V_k is the viscous diffusion and T_k is the turbulence diffusion. In the equation, any quantity (say ϕ) was Reynolds averaged by averaging in time and it was decomposed in its mean part ($\overline{\phi}$) and fluctuating part (ϕ'). While, a Favre averaged quantity, decomposed in a mean part as, $\widetilde{\phi}=\overline{\rho\phi}/\overline{\rho}$, and its fluctuating part, was denoted by ϕ''. After getting the mean quantity by either of the methods, further averaging was performed in the circumferential direction, as it was considered a homogeneous direction. Turbulent statistics were obtained after averaging in time for at least 10 flow through times, corresponding to 300 times of the characteristic turbulent time scale ($t = R/U_0$).

$$\frac{\mathrm{D}k}{\mathrm{D}t} = P_k + \varepsilon + \Pi_k + V_k + T_k \tag{2.5}$$

Where,

$$k = \frac{1}{2}\overline{\rho u_i'' u_i''}, \qquad P_k = -\overline{\rho u_i'' u_j''}\frac{\partial \tilde{u}_j}{\partial x_i}, \qquad \varepsilon = \overline{\tau_{ij}'\frac{\partial u_i''}{\partial x_j}}$$

$$\Pi_k = -\frac{\partial \overline{p' u_j''}}{\partial x_j}, \qquad V_k = \frac{\partial \overline{\tau_{ij}' u_i''}}{\partial x_j}, \qquad T_k = -\frac{1}{2}\frac{\overline{\partial \rho u_i'' u_i'' u_j''}}{\partial x_j}$$

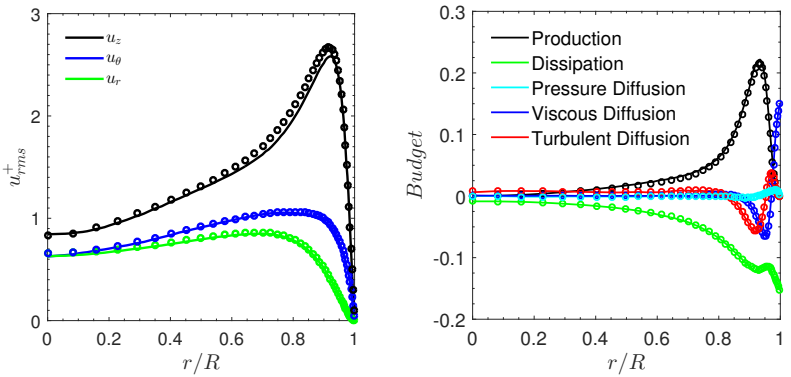

(a) (b)

Fig. 2.3 Inflow generator verification with (a): root mean square values for velocity normalized with u_τ and (b): turbulent kinetic energy budget normalized with $\rho u_\tau^4/\nu$. Solid lines: present study, and overlapping symbols: Khoury et. al [40]

Figure 2.3 shows an excellent agreement of the current DNS with the chosen reference. The core of this numerical method was developed by Chu [28]. He validated this method with experiments of Shehata and McEligot [121] for heat transfer to strongly heated air [121]. In addition, Chu and Laurien [30] have verified this code with other low Mach number DNS of supercritical CO_2. They have shown a satisfactory agreement with the DNS of Bae et al. [9] and Nemati et al. [94]. However, the mean wall temperature from all three DNS has shown a slight mismatch even with the same assumptions and validation with the same experimental data of Shehata and McEligot [121]. The obvious reason for this disagreement includes the selection of different thermophysical properties database, mesh resolution, and numerical schemes. This aspect needs further investigations and it is beyond the scope of the present work.

2.1.5 Computational performance

The simulations in this study were performed at the *Hazel Hen* facility of HLRS Stuttgart. It is a Cray XC40 system and consists of 7712 compute nodes. Each node has two Intel Haswell processors (E5-2680 v3, 12 cores) and 128GB memory, and the nodes are interconnected by a Cray Aries each network with a Dragonfly topology. This amounts to a total of 185,088 cores and a theoretical peak performance of 7.4 PFlops.

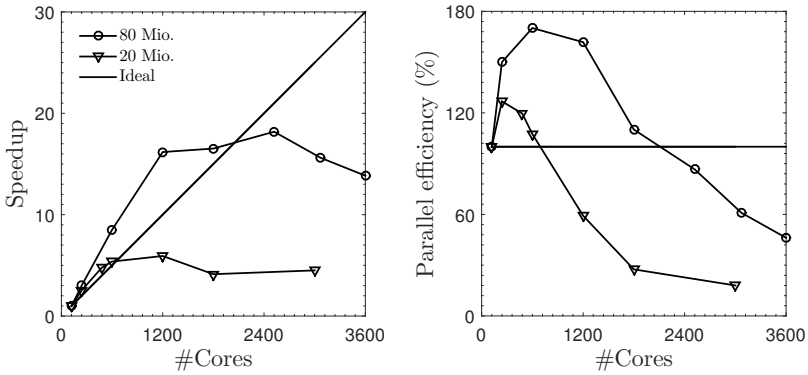

Fig. 2.4 Scaling behavior of OpenFOAM v4.0 on *Hazel Hen* at HLRS. This data was obtained with a problem size of 80 Mio. and 20 Mio. cells. (a): Speedup and (b): Parallel efficiency

The parallel computing in OpenFOAM uses OpenMPI, which is an open source Message Passing Interface (MPI) implementation of the standard MPI. For the parallel computing, OpenFOAM is based on the domain decomposition method, in which the computational domain is divided into smaller pieces and allocated to processors. There are four different algorithms available within OpenFOAM for the domain decomposition. The 'hierarchical'method was used in this work because it has shown better computational performance for the simulated geometry. During this study, only two latest time-step data

were stored to avoid the limitation of number of files and the memory. Thus, averaging in time was done on the run and as a post-processing step, other calculations such as coordinate transformation and Favre-averaging was performed. This also saves computational-time during reconstructing data and averaging afterwards. Different post-processing utilities were developed in C++ and MATLAB to handle the large size data.

For the scalability test, the first 100 time-steps were ignored to avoid any influence of start-up time of simulation and the next 100 time-steps were used to characterize the code. Figure 2.4a illustrates the strong scaling behavior for the current problem. The speedup was defined as the ratio of computation time on the reference core (120 in this case) to the computation time on the tested core while the parallel efficiency was defined as the ratio of actual speed to the ideal speedup (in %). The scalability test conducted with reference performance at 120 cores. A superlinear scalability can be seen at lower cores but the performance degrades for larger numbers of cores. A typical simulation with 80 Mio. cells take approximately 150,000 CPU-hours for 10 flow through times in the pipe flow [98].

2.2 Description of fully compressible simulation

A framework is presented in this thesis for the fully-compressible, high-fidelity CFD simulations at supercritical pressure. A relatively new CFD code, Flexi [57], is selected. The code Flexi is a high-order CFD code and it is made open-source under GPL V3.0. This section describes the governing equations, numerical method, equation of states, computational details along with the supporting theory for the analysis for the computational code Flexi.

2.2.1 Integration domain and boundary conditions

In addition to pipe flow, channel flow is the most examined wall-bounded turbulent flow, which is ubiquitous in the power cycle. The simple geometry

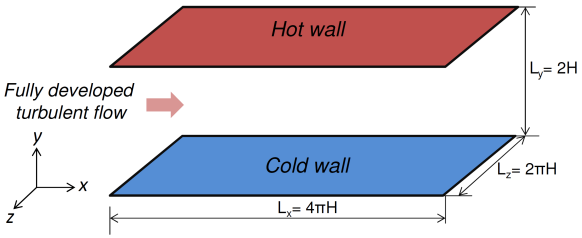

Fig. 2.5 Geometry for fully compressible turbulent channel flow (not to scale)

of the channel provides an opportunity to investigate the complex nature of turbulence in the flow. Therefore, a plane channel flow configuration as depicted in Figure 2.5 is chosen for this work. The streamwise and spanwise directions were considered as homogeneous with the periodic boundary condition and wall-normal direction has the no-slip boundary condition at the two extreme edges. These two walls have isothermal boundary conditions with a different temperature to achieve the effects of variable properties of supercritical CO_2. The channel has dimension $L_x \times L_y \times L_z = 4\pi H \times 2H \times 2\pi H$, with H as the half channel height. The half width of the channel is adjusted to match the desired Reynolds and Mach number. The periodic boundary conditions are employed in the homogeneous streamwise and spanwise directions. The flow in each case including the validation study was initialized with a laminar velocity profile superimposed with random fluctuations as illustrated in Equation (2.6).

$$u_x = u_{x,max}(1-y^2)(1+\Upsilon), u_y = 0, u_z = 0 \tag{2.6}$$

Where $u_{x,max}$ is the maximum velocity in a laminar channel flow and it is fixed to 1.5 of the mean velocity, y is the wall-normal coordinate and Υ is the perturbation function. This perturbation function is defined as; $\Upsilon = A \times random - number$. The constant A can be increased or decreased to speed up the development of turbulent flow in the channel. It is set to 0.5 in the

present study. For other variables (e.g. temperature, density), a uniform value was imposed in the flow field. The computational domain consists of $N_x \times N_y \times N_z = 128 \times 56 \times 128$ with a polynomial degree of 3-5. It results in approximately 58-200 Millions degree of freedom for the domain. This mesh resolution is comparable to Sengupta et al. [119] (used 186 Mio.) and Ma et al. [87] (used 37 Mio.). The mesh resolution was chosen to resolve the Kolmogorov and Batchelor scales.

2.2.2 Governing equations

Fully compressible Navier-Stokes equations were used to describe the flow in this CFD code unlike the low Mach number assumption used in OpenFOAM. Equations 2.7-2.9 are the mass, momentum and energy conservation for the DNS with Flexi, respectively;

$$\frac{\partial \rho}{\partial t} + \nabla \cdot (\rho \mathbf{u}) = 0 \tag{2.7}$$

$$\frac{\partial \rho \mathbf{u}}{\partial t} + \nabla \cdot [\rho \mathbf{u}\mathbf{u} + p\mathbf{I} - \tau] = \zeta \tag{2.8}$$

$$\frac{\partial e}{\partial t} + \nabla \cdot [(e+p)\mathbf{u}] = \nabla \cdot [\tau \cdot \mathbf{u} - \mathbf{q}] + \mathbf{u}\zeta \tag{2.9}$$

$$e = e_i + \frac{1}{2}\rho \mathbf{u} \cdot \mathbf{u}; \quad e_i = f(\rho, p); \quad p = f(\rho, e_i) \tag{2.10}$$

In Equations (2.7)-(2.10), ρ is the density, $\mathbf{u}$ is the velocity vector ($\mathbf{u} = [u, v, w]$), p is the pressure, e is the total energy per unit volume, e_i represents the internal energy per unit volume. The viscous stress is denoted by τ and heat flux by $\mathbf{q}$, defined by equations (2.11) and (2.12), respectively. A source term (ζ) was added to the streamwise momentum and correspondingly to the energy equation to drive the flow. This forcing term is analogous to the pressure gradient in pressure driven flows. The forcing term is applied only in

the streamwise direction and remains constant throughout the domain. But, it varies in time in such a way to keep the mass flux constant. In Eq (2.12), κ is the thermal conductivity.

$$\tau = \mu \left[[\nabla \mathbf{u} + (\nabla \mathbf{u})^T] - \frac{2}{3}(\nabla \cdot \mathbf{u})\mathbf{I} \right] \tag{2.11}$$

$$\mathbf{q} = -\kappa \nabla T \tag{2.12}$$

2.2.3 Numerical method

The CFD solver is based on the discontinuous-Galerkin spectral element method [57]. Due to fully-compressible DNS, a density-based approach for the solution of the Navier-Stokes equations is applied instead of the pressure based approach used earlier with OpenFOAM. A brief description of the solver follows. A typical conservation equation (e.g. Equation 2.7-2.9) is shown in Equation 2.13. Here, $\mathbf{U}$ is the solution vector, $\mathbf{U} = [\rho, \rho u, \rho v, \rho w, \rho e]^T$, the subscript t represents the time derivative and $\mathbf{F}$ is the flux for viscous and heat conduction.

$$\mathbf{U_t} + \mathbf{F}(\mathbf{U}, \nabla \mathbf{U}) = 0 \tag{2.13}$$

During the computation, the whole domain is subdivided into non-overlapping hexahedral elements, followed by a mapping of each element onto the reference cube element, $E = [-1,1]^3$ by a mapping $x(\xi)$, where $\xi = (\xi, \eta, \zeta)$ is the master element coordinate vector. Due to this mapping, equation 2.13 turns to:

$$\mathbf{J U_t} + \varphi(\mathbf{U}, \nabla_\xi \mathbf{U}) = 0 \tag{2.14}$$

Where J is the Jacobian and ∇_ξ is the Nabla operator for the mapped space. As a next step, the solution and fluxes are approximated by a tensor-product basis of 1-D Lagrange interpolating polynomials; volume and surface integrals

are replaced by Gauss-Legendre or Gauss-Legendre-Lobatto quadrature. The evaluation of the numerical fluxes at the element faces is done by formulating a Riemann problem. The time discretization was performed using an explicit fourth-stage Runge-Kutta scheme. The split form DG method [49] was also employed for the robustness of the DNS. Further details about the solver and its implementation can be found in the literature [17, 8, 126].

2.2.4 Equation of state

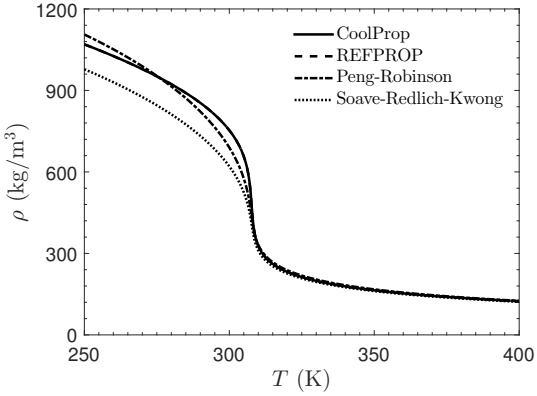

Fig. 2.6 A comparison of density as a function of temperature at a pressure of 8 MPa derived from different equation of states

An equation of state (EoS) described in Equation 2.10 is required for the DNS. In fully-compressible simulations, EoS depends both on pressure and temperature, unlike the low-Mach number simulations described earlier, where properties are a function of temperature only. There are a few fully compressible DNS investigations available in the literature for supercritical fluids but all of them are conducted with the Peng-Robinson EoS, which is a cubic equation of state. This analytical cubic EoS is computationally efficient but it deviates from the standard database. A comparison of two commonly

used cubic EoS (Peng-Robinson [103] and Soave-Redlich-Kwong [112]) with the two different standard databases (REFPROP [81] and CoolProp [18]) is shown for the temperature dependent density. While both the database overlaps as they use the same EoS exclusive to CO_2 [127]. On the other hand, the cubic EoS shows a significant deviation, especially in the subcritical region. The deviation can be as high as approximately 55% for isobaric specific heat [119].

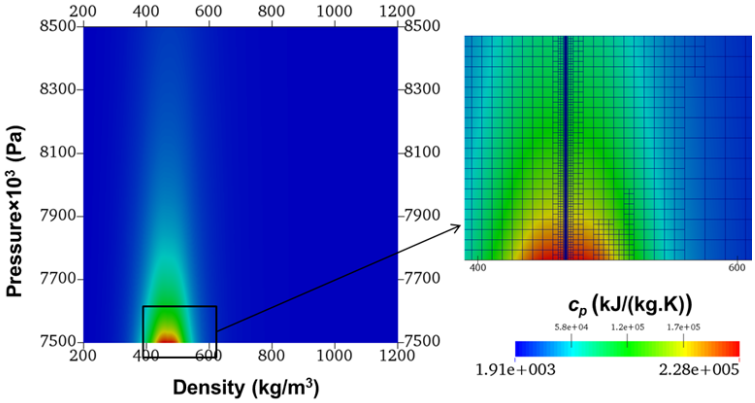

Fig. 2.7 Implementation of EoS library to CO_2 derived from CoolProp [18]

Therefore, the standard database was chosen for this work to provide a high-fidelity framework, which is a foremost requirement and an objective of this work. A Fortran-90 language based library is used for the EoS and it is based on the adaptive tabulation using a quad-tree approach. In this method, the tables for EoS were built prior to the simulations. It relies on interpolation instead of iteration and uses L_2 projection method to calculate the polynomial coefficients [39]. The tool has the capability to derive these tables from typical EoS (e.g. Peng-Robinson, Redlich-Kwong, and ideal gas) and standard database (e.g. CoolProp [18] and REFPROP [81]). Figure 2.7 shows a result of this implementation for carbon dioxide derived from

CoolProp database for the isobaric specific heat as a function of density and pressure. The grids are also shown in the zoomed-in figure to illustrate the adaptive mesh refinement capabilities of the library. The mesh is refined close to the saturation curve where thermophysical properties show drastic variations. But as one moves away from the critical region, cells become larger in size. The mesh refinement is governed by the error level and maximum steps for refinement. As a next step, these EoS tables are supplied to the solver before starting the simulation. During the simulation, an iteration of a specific quantity is replaced by an interpolation of the polynomial basis. The valid cell for the EoS interpolation is found by a grid traversal through the quad-tree until the lowest level is reached [45]. Compared with the analytical EoS (e.g. Peng-Robinson) and the full IAPWS-IF97, this EoS table achieves a high-accuracy combined with acceptable computational costs at the same time. A speedup of three orders of magnitude was reported by Dumbser et al. [39] as compared with the IAPWS-IF97 EoS.

2.2.5 Verification of the code

A verification study which is relevant for the simulated cases (i.e. turbulent channel flow), is provided in this section for constant property flow. Two different DNS databases were selected to verify both low and high Mach number flow. Identical conditions have been used as of the original cases. The low Mach number channel flow corresponding to case M02 in Table 2.2, is validated with the well known incompressible channel flow DNS data of Kim et al. [69] (acronym as KMM). Originally, Kim et al. [69] used incompressible flow (i.e. Ma=0) while here Ma = 0.2 was used to avoid compressibility effects. Figure 2.8 shows the wall-normal profiles for the mean velocity and root mean square velocity fluctuations normalized with the bulk velocity (U_b). In the figures, y represents the distance from the wall of the channel. A fairly good agreement can be observed from Figure 2.8 for the incompressible flow case. For high Mach number case, DNS data of

Table 2.2 Physical and numerical parameter for verification study

Case	Ma	Re	Re_τ	$L_x \times L_y \times L_z$	$N_x \times N_y \times N_z$
KMM	0	2800	178	$4\pi H \times 2H \times \frac{4\pi}{3}H$	$192 \times 129 \times 160$
M02	0.2	2700	181	$4\pi H \times 2H \times \frac{4\pi}{3}H$	$256 \times 112 \times 112$
CKM15	1.5	3000	222	$4\pi H \times 2H \times \frac{4\pi}{3}H$	$144 \times 119 \times 80$
M15	1.5	3000	222	$4\pi H \times 2H \times \frac{4\pi}{3}H$	$256 \times 112 \times 112$

Coleman et al. [32] (acronym as CKM15) were chosen. The authors have performed DNS with power-law dynamic viscosity with an exponent of 0.7. The agreement for high Mach numbers (case M15) is also good with the data of Coleman et al. [32] corresponding to case CKM15. Further validation with variable property flow at supercritical pressure is not presented here due to unavailability of experimental data. A much higher resolution was used for DNS at supercritical pressures as compared to those for a constant property DNSs to have a certainty about the resolving small-scale turbulence motion. Moreover, the code is extensively validated for compressible and incompressible cases including the periodic-hill, NACA 0012 airfoil, spatially-developing supersonic turbulent boundary layer [8]. Additionally, this high-order code has been used to study liquid-vapor flow with phase transition and surface tension [42], two-phase flow [41] and shock-capturing [126].

2.2.6 Computational performance

The computer program for this method is written in Fortran-90. It uses a computationally efficient equation of state based on the adaptive quad-tree data structure. The code is parallelized using OpenMPI and uses the Hierarchical Data Format - 5 (HDF5) library for input and output (I/O) operations. Similar to OpenFOAM, the parallelization is achieved by decomposing the computational domain and allocating each domain to a processor. The domain decomposition is automatically based on space-filling curves. During the

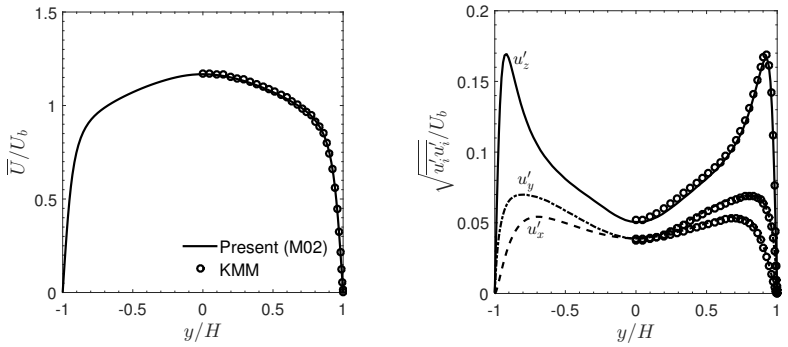

(a) (b)

Fig. 2.8 Verification of code Flexi for turbulent channel flow at low Mach number. (a): mean velocity profile, (b): root mean square fluctuations. Lines: present study, and overlapping symbols: Kim et al. [69]

simulations, the data from all time steps were saved and post-processing was performed at the end. The post-processing utilities were developed within Fortran-90 and Python to handle the big data. In the past, this code has shown massively parallel scalability for ideal gas. But, scaling behavior and calculation time may get adversely affected due to the inclusion of more sophisticated EoS and real gas effects in the supercritical region. Therefore, strong scaling characteristics of the code without multi-threading are tested.

Table 2.3 Computational parameter for parallel-scalability investigation

Case	N_x	N_y	N_z	#Elements	N	#DoF
1	32	14	32	14,336	4	1,792,000
2	128	56	128	917,504	2	24,772,608
3	128	56	128	917,504	5	198,180,864

The simulations were performed on *Hazel Hen* for a range of 96–12,288 physical cores. A representative case is used to characterize the scaling

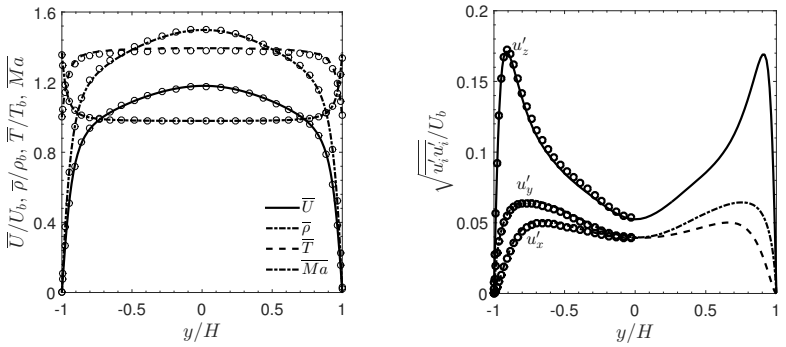

(a) (b)

Fig. 2.9 Verification of code Flexi for turbulent channel flow at high Mach number. (a): mean profile, (b): root mean square fluctuations. Lines: present study, and overlapping symbols: Coleman et al. [32]

behavior of the code at supercritical pressure. For the same, two different domain viz. Low with 32× 14× 32 elements and High with 128× 56× 128 elements were selected with varying degrees of freedom as mentioned in Table 2.3. All cases use the same numerical setup except the number of elements and degree of the polynomial (N) in the mesh. These cases are executed for 200 timesteps and speedup is calculated only for the simulation time without considering the initialization and other I/O. The performance index $\left(PID = \frac{wall-clock-time \cdot \#cores}{\#DOF \cdot \#time-steps \cdot \#Runge\ Kutta-stages}\right)$ is also calculated, which is a measure of the performance of different setup, and it decouples the #DoF, #cores and #time-steps. The computational time per time step is increased by a factor of ≈3.8 compared to calculation for an ideal gas due to the inclusion of the sophisticated EoS.

Figure 2.10 shows the speedup and parallel efficiency for the solver with the representative testcase. A very good scalability of the code at 200 Mio. degrees of freedom can be seen until 1024 nodes with a parallel efficiency of 90-100 %. Interestingly, there is also a slightly super-linear speedup at

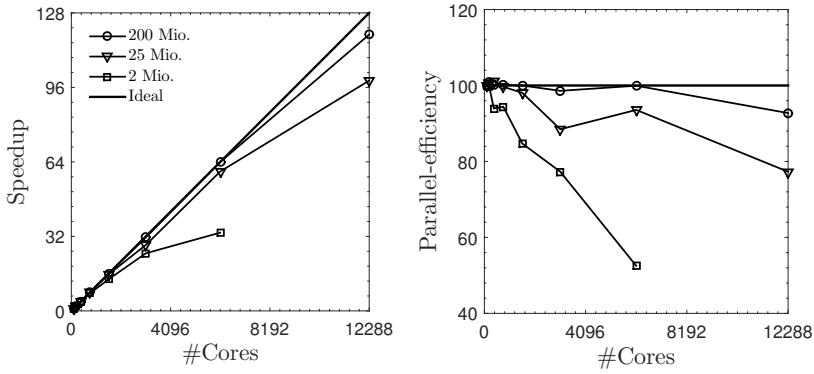

Fig. 2.10 Comparison of strong scaling of the present solver without multi-threading for varying degree of freedom; (a): Speedup (b) Parallel-efficiency

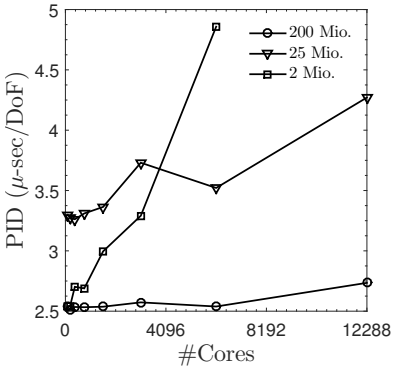

Fig. 2.11 Performance index (PID) for strong scaling of the present solver without multi-threading for varying degree of freedom

192-384 nodes. The efficiency and speedup degrade as the degrees of freedom decrease. But for a realizable DNS of supercritical CO_2 which resolve the small turbulence scale, typical DoF is in the same order of case-1. The performance index (PID) has the least value for 200 Mio DoF case and it

remains nearly constant over the range of employed nodes (refer to Figure 2.11).

Chapter 3

Characterization of the cooling process at supercritical pressure

The present literature shows only few DNS studies pertaining to the heating of supercritical CO_2. But, none of the numerical experiments deal with cooling. Therefore, this chapter includes the results from DNS of cooling of sCO_2 by using OpenFOAM as CFD code. The simulations were conducted with a uniform heat flux imposed at the wall at inlet bulk Reynolds number of 5,400 and 5,238. The aim of this DNS is to understand the role of buoyancy in modulating the turbulence in a flow where properties are spatially varying. Heat transfer deterioration followed by recovery is observed in downward flow while enhancement occurs in upward flow as compared to forced convection. The decomposition of skin friction factor and the Nusselt number was performed by means of FIK identity to understand the role of individual term. The major effects on skin friction factor were brought by the non-uniform body force due to gravity. The turbulent parts equally influence the Nusselt

number as well skin friction factor in supercritical flows. Quadrant analysis and its weighted joint probability density function were analyzed to understand the role of sweep (Q_4) and ejection (Q_2) events. During the heat transfer deterioration, sweep and ejection events are decreased greatly, triggering the reduction in turbulence. The recovery in turbulence is brought by the Q_1 and Q_3 (also known as outward and inward interaction) events, contrary to the conventional belief about turbulence generation. The turbulence anisotropy of the Reynolds stress tensor is investigated showing that the turbulence structure becomes rod-like during the deteriorated heat transfer regime in the downward flow and disc-like for the upward flow.

3.1 Description of the cases

The flow domain, boundary conditions, and mesh resolution were discussed earlier in Section 2.1. The tube diameter is set to 2 mm, which is in the range of the hydraulic diameter of a compact heat exchanger. In the present investigation, 14 distinct cases have been simulated for two different pressures (1.08 and 1.18 time of critical pressure). Through these simulations, all three possibilities in a vertical flow are considered viz. upward, downward flow and forced convection in which gravity is set to zero. The inlet bulk Reynolds number (Re_0) is taken to be 5,400 and 5,238. The Reynolds number in heat exchangers used in the power cycle can be as high as 70,000. But this study is limited to low Reynolds number because of the drastic increase in the computational time contributed by fine mesh requirement and larger axial length. Table 3.1 and 3.2 gives a summary of the conditions simulated here. Here, Gr_0 represents the Grashof number based on heat flux defined as: $\mathrm{Gr}_0 = \frac{g\beta q_w D^4}{\kappa \nu^2}$; where β is the coefficient of thermal expansion and q_w is wall heat flux. The buoyancy number defined as: $\mathrm{Bo}_0 = \frac{\mathrm{Gr}_0}{\mathrm{Re}_0^{3.425}\mathrm{Pr}_0^{0.8}}$.

Table 3.1 A summary of simulation conditions at Re_0=5400, $L_h = 30D$

Case	Direction	$Gr_0 \times 10^8$	$Bo_0 \times 10^{-5}$	p_0 (MPa)	T_0 (K)	q_w (W/m^2)
FC80q1	Forced	0	0	8.0	342.05	-30.87
UC80q1	Mixed (upward)	1.17	1.7	8.0	342.05	-30.87
DC80q1	Mixed (downward)	-1.17	-1.7	8.0	342.05	-30.87
FC80q2	Forced	0	0	8.0	342.05	-61.74
UC80q2	Mixed (upward)	2.34	3.4	8.0	342.05	-61.74
DC80q2	Mixed (downward)	-2.34	-3.4	8.0	342.05	-61.74
FC88q1	Forced	0	0	8.8	342.05	-30.87
UC88q1	Mixed (upward)	1.56	2.1	8.8	342.05	-30.87
DC88q1	Mixed (downward)	-1.56	-2.1	8.8	342.05	-30.87
UC88q2	Mixed (upward)	3.12	4.24	8.8	342.05	-61.74
DC88q2	Mixed (downward)	-3.12	-4.24	8.8	342.05	-61.74

Table 3.2 A summary of simulation conditions at Re_0=5238, $L_h = 60D$

Case	Direction	$Gr_0 \times 10^8$	$Bo_0 \times 10^{-5}$	p_0 (MPa)	T_0 (K)	q_w (W/m^2)
FC80q1Re52	Forced	0	0	8.0	322.18	-30.87
UC80q1Re52	Mixed (upward)	3.0	3.7	8.0	322.18	-30.87
DC80q1Re52	Mixed (downward)	-3.0	-3.7	8.0	322.18	-30.87

The inlet temperature in the cases given in Table 3.1 is 342.05 K, which is the inlet temperature of pre-cooler in the power cycle described in Section 1.1, while the inlet temperature in the remaining 3 cases, corresponding to Table 3.2, is set to 322.18 K so that bulk output temperature is similar as the outlet temperature of pre-cooler.

3.2 Kolmogorov and Batchelor length scale

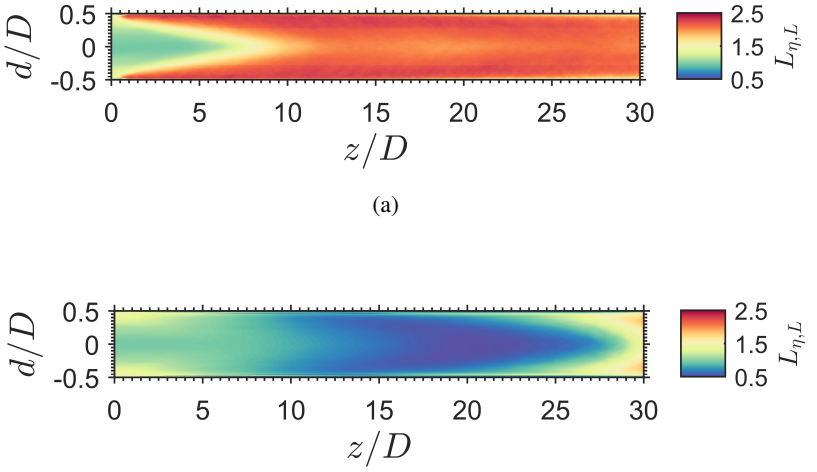

Fig. 3.1 Variation of spatial resolution normalized by Kolmogorov length scale over the length. (a): Case UC80q2, and (b):Case DC80q2

Earlier in Table 2.1, a comparison of the mesh resolution was presented from the past studies in the literature. Pandey et al. [99] quantified the mesh resolution from the viewpoint of small turbulence length scales. The mesh

resolution for pipe in this work intends to resolve the Kolmogorov length scales [1], $\eta = \left[\frac{\bar{\nu}^3}{\varepsilon}\right]^{0.25}$, here ε is the dissipation rate of turbulent kinetic energy per unit mass. Figure 3.1 shows the spatial resolution normalized with the Kolmogorov length scale (say, $L_{\eta,L} = \Delta v/\eta$) for cases UC80q2 and DC80q2. The spatial resolution is defined by taking the cube root of the cell volume, $\Delta v = \sqrt[3]{\Delta r \Delta r \theta \Delta z}$. It can be seen that the normalized spatial resolution varies in between 0.5-2.5, which should be sufficient to capture the small-scale motions (also refer to Figure 3.1a). The minimal thermal scale, defined as $\eta_\theta = \eta/\sqrt{\mathrm{Pr}}$, depends on the ratio of thermal to momentum diffusivity and it is used to normalize the spatial length scale (say, $L_{\eta,T}$). Figure 3.2b shows $L_{\eta,T}$ for three locations along the pipe. At the inlet, the Prandtl number (Pr) is 1.1, therefore, both length and thermal scale have a comparable magnitude. After that, the increase in Prandtl number imposes the restriction to use the fine mesh and the maximum value of $L_{\eta,T}$ is kept below 6.5 in this study. This value denotes that thermal scales are slightly under-resolved. Nevertheless, a grid independence study indicates insignificant variation in first order statistics when the mesh was four times coarse than the mesh used in this study.

3.3 Flow and heat transfer features

Direct numerical simulations were accomplished for cases as mentioned in Table 3.1 and 3.2. The mean statistics were obtained by averaging with respect to time and homogeneous circumferential direction. The averaged statistical analysis was performed using Reynolds and Favre averaging. For a variable, ϕ, Reynolds decomposition is defined as, $\phi = \overline{\phi} + \phi'$, with $\overline{\phi'} = 0$. The Favre averaged quantity can be denoted as $\phi = \tilde{\phi} + \phi''$, with $\overline{\rho\phi''} = 0$. These results were obtained by averaging in time for at least 10 flow through times. From a qualitative discussion point of view, only results from Table 3.1 with wall

[1] Kolmogorov scale are indicative of the smallest eddies present in the flow. At these length scales, viscosity dominates and the turbulent kinetic energy is dissipated into heat.

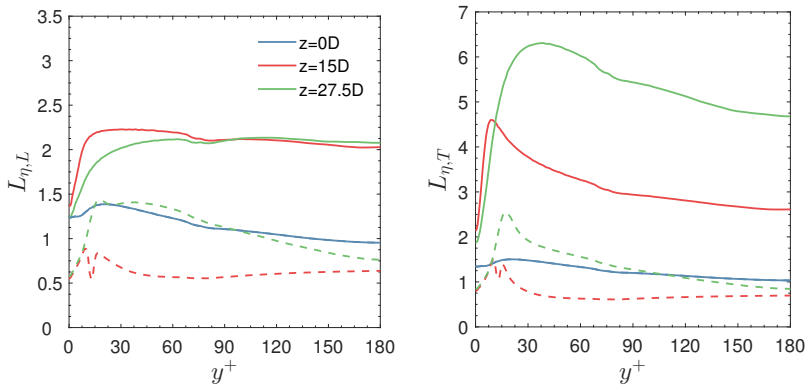

(a) (b)

Fig. 3.2 Radial profiles of (a): velocity scale, and (b): minimal thermal scale; solid lines: case UC80q2 and dashed lines: case DC80q2. Note: Difference in ordinate scales.

heat flux of -61.74 kW/m^2 are discussed here. The rest of the results can be found in Appendix A.1.

Figure 3.3a shows the axial variation of wall shear stress, $\tau_w = \overline{\mu \frac{\partial u_z}{\partial r}}\Big|_{wall}$. At the inlet, all cases show a good agreement with the constant property flow case but as fluid proceeds downstream, hydraulic resistance changes significantly in every case except for the forced convection case because buoyancy is absent here. For the upward flow case, there is a sudden decrease in wall shear stress contributed by a sharp reduction in the streamwise-velocity gradient in the radial direction at the wall shown in Figure 3.3c. Although mean viscosity increases as illustrated in Figure 3.3b but its order of magnitude is very small compared to mean velocity gradient. The downward flow case shows a relatively higher skin friction coefficient which is a result of the favorable velocity gradient. A peculiar behavior can be observed in the upward flow case where the wall shear stress shows negative values at certain axial positions along the pipe.

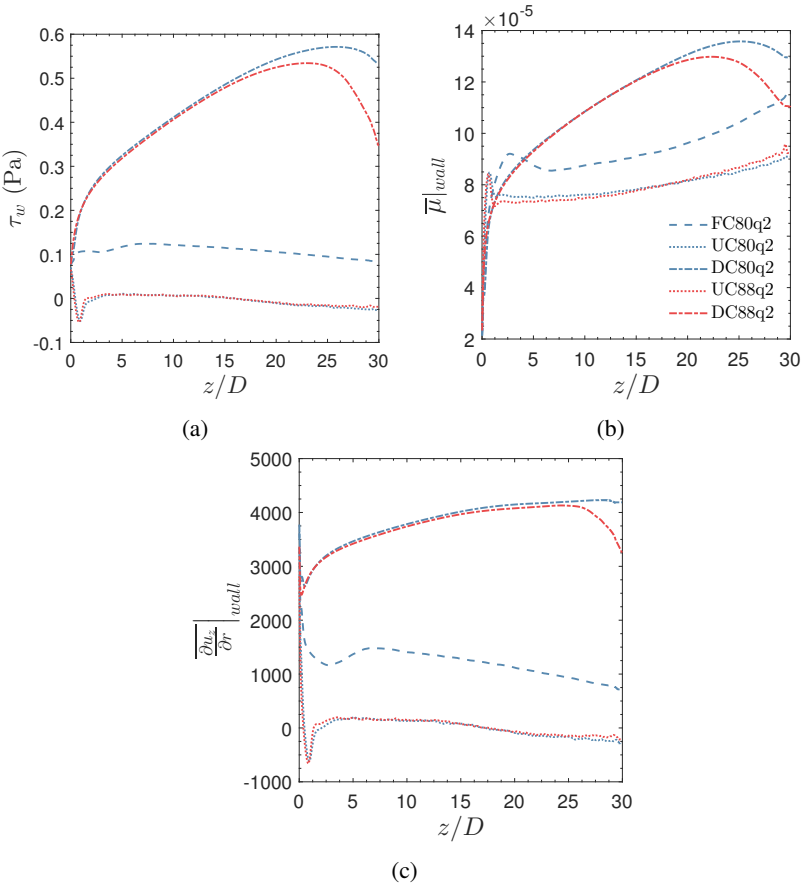

Fig. 3.3 Streamwise hydraulic characteristics for q_w=-61.74 kW/m^2. (a): Wall shear stress, (b): Mean dynamic viscosity, and (c): Mean gradient of velocity at the wall

The streamwise mean velocity profile is shown in Figure 3.4 for case DC80q2, FC80q2, and UC80q2 at different streamwise locations. The velocity profile is same at the inlet ($z = 0D$) for all three cases as they share same inlet

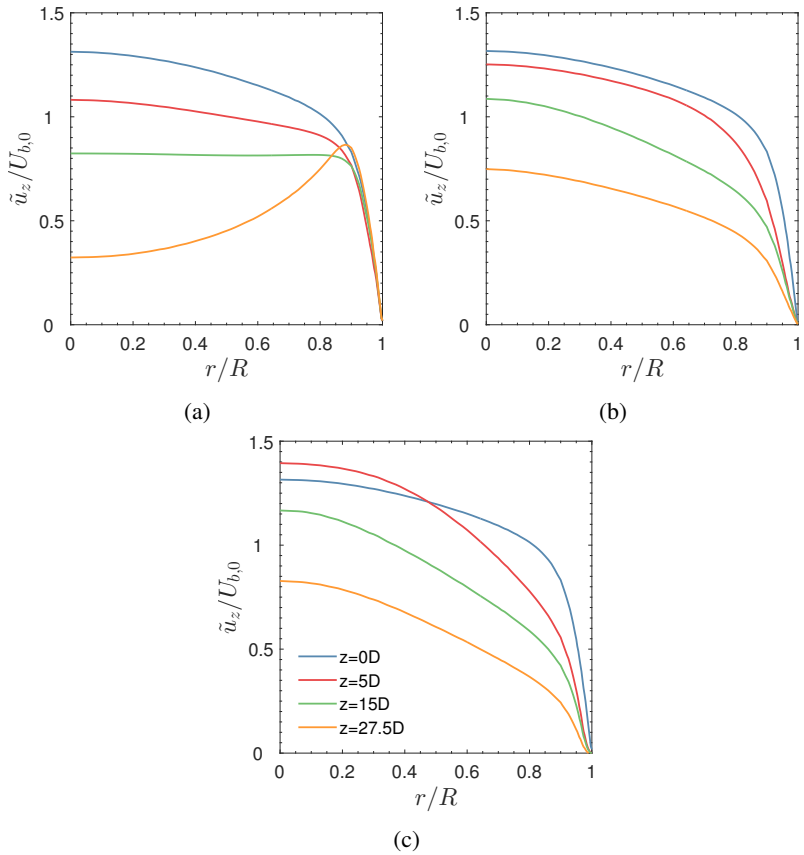

Fig. 3.4 Radial profiles of Favre averaged streamwise velocity for (a): Case DC80q2, (b): Case FC80q2, and (c): Case UC80q2

conditions. In case DC80q2, mean velocity profile flattens out at $z = 15D$ but it deformed into M-shape near to the outlet. A continuous deceleration can also be observed from the inlet to outlet. The velocity profile is distorted significantly in the near-wall region for case UC80q2 (refer to Figure 3.4c). Due to the distorted mean velocity profile in the near-wall region, the radial

velocity gradient (shown in Figure 3.3c) fluctuates around zero along the streamwise direction which leads to a negative wall shear stress at multiple axial locations. In case FC80q2, the mean velocity profile uniformly changes due to deceleration and it is not affected by the buoyancy.

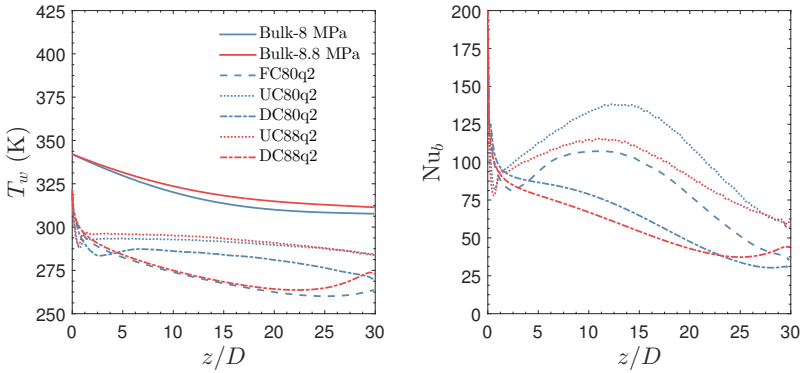

(a) (b)

Fig. 3.5 Streamwise heat transfer characteristics for q_w=-61.74 kW/m^2. (a): Wall temperature, and (b): Bulk Nusselt number

Figure 3.5a shows the variation of wall temperature for all five cases. It is known now that the heat transfer deterioration occurs during the downward flow of supercritical fluids under the cooling conditions. The wall temperature shows a comparatively lower magnitude in downward flow cases and it indicates an increase in temperature difference between wall and bulk fluid resulting in smaller Nusselt numbers $\left(\mathrm{Nu}_b = \frac{q_w D}{\kappa_b (T_w - T_b)}\right.$, where T_b is the bulk temperature and κ_b is the thermal conductivity at $\left.T_b\right)$ as shown in Figure 3.5b. This is a characteristic of deteriorated heat transfer. The main reason for deteriorated heat transfer is the reduction in turbulence until $z \approx 20D$ in downward flow due to the adverse effects of the body force as a result of buoyancy as it is evident from Figure 3.6a, which shows the variation of Reynolds shear stress (RSS=$\overline{\rho u_r'' u_z''}$) in the radial direction for different axial

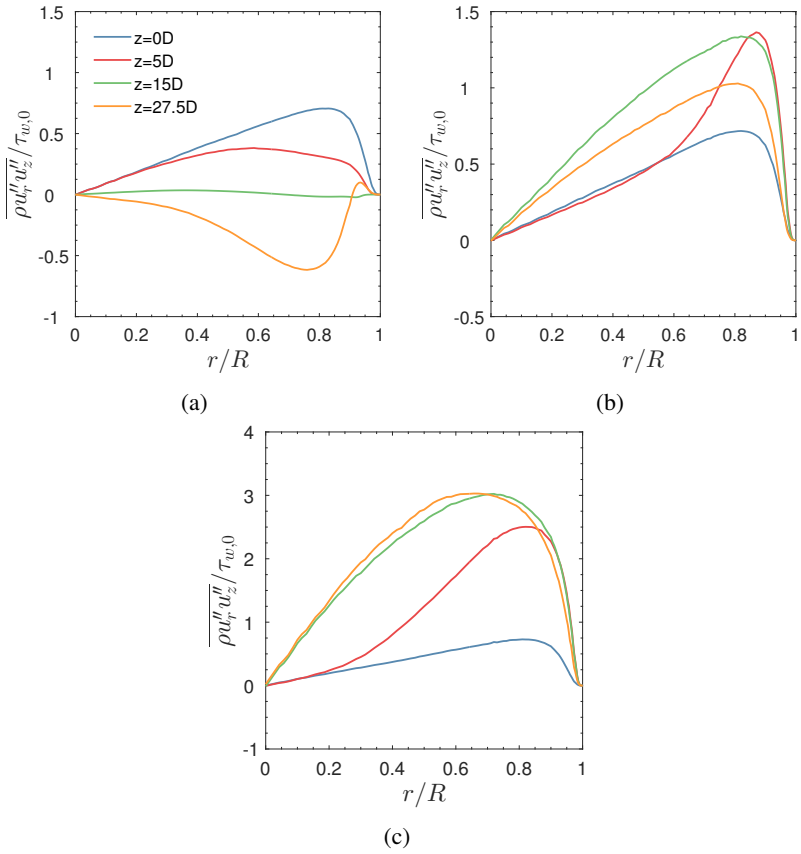

Fig. 3.6 Radial profiles of Reynolds shear stresses at different axial locations for (a): Case DC80q2, (b): Case FC80q2, and (c): Case UC80q2. Note: Difference in ordinate scales

locations. On the other hand, Reynolds shear stress shows an increasing trend for the forced and the upward flow cases. The forced convection case is not affected by buoyancy and it only has the effect of thermal deceleration, which is common to all five cases. The buoyancy force acts as a source term during

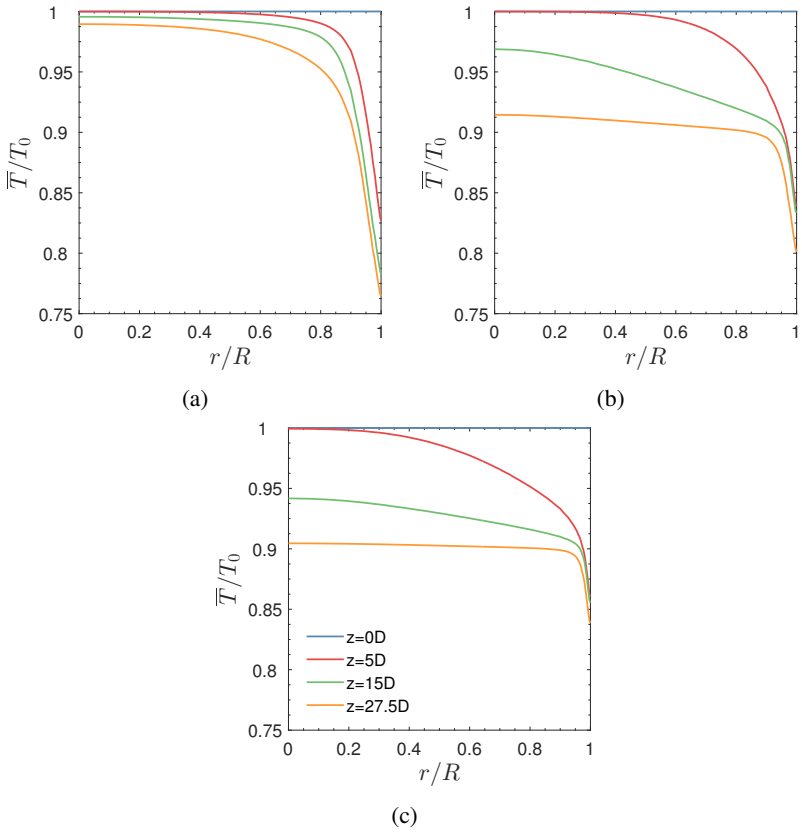

Fig. 3.7 Radial profiles of mean temperature for (a): Case DC80q2, (b): Case FC80q2, and (c): Case UC80q2.

the upward-cooling due to unstable stratification and it also favors turbulence, while in downward flow, buoyancy can act as a source or sink term depending on the streamwise gradient of ρg. The effect of inlet pressure can also be seen in Figure 3.5. During the heat transfer recovery, the mean velocity profile became M-shaped and it leads to a recovery of kinetic production of turbulence

[9]. An early and more intense heat transfer recovery (increase in Nusselt number) can be observed for a higher pressure for downward flow from Figure 3.5b. The peak in the Nusselt number distribution for upward flow decreases with the increase in the pressure shown in Figure 3.5b. This especially stems from the reduction of isobaric specific heat at the pseudocritical point as one moves away from the critical point. Figure 3.7 illustrates mean temperature profiles in the radial direction for different streamwise locations. The mean temperature distributions differ significantly in each case for the same streamwise locations except at the inlet. In downward flow, the higher temperature difference between wall and center leads to higher variations in density which makes buoyancy effects more severe. In case FC80q2 and UC80q2, the wall and centerline temperature difference are less as compared to case DC80q2. Further examinations of impaired and enhanced heat transfer are performed in the next section. While analyzing further, only three cases namely; DC80q2, FC80q2, and UC80q2 are considered as they are more prone to be affected by property variations.

3.4 Turbulence modulation

The deteriorated and enhanced heat transfer to sCO_2 is influenced by the role of turbulence. Figure 3.8 illustrates the radial profile of turbulent kinetic energy (k=0.5$\overline{\rho u_i'' u_i''}$). In case of downward cooling of sCO_2, buoyancy has a negative influence on the turbulence, as can be observed from Figure 3.8a. Buoyancy dampens the turbulence which is evident from the reduced value of TKE from $z = 0D$ to $15D$. At $z = 27.5D$, its magnitude shows an increment at the near-wall region, which is certainly due to positive buoyancy production. In the downward cooling, both stable and unstable stratification can occur, therefore, buoyancy can act as source or sink. In the case of upward-cooling, TKE increased in the streamwise direction depicted in Figure 3.8c. The increase from z=0D to 15D is significant but after that changes are not pronounced. This is due to the radial density difference between the core and

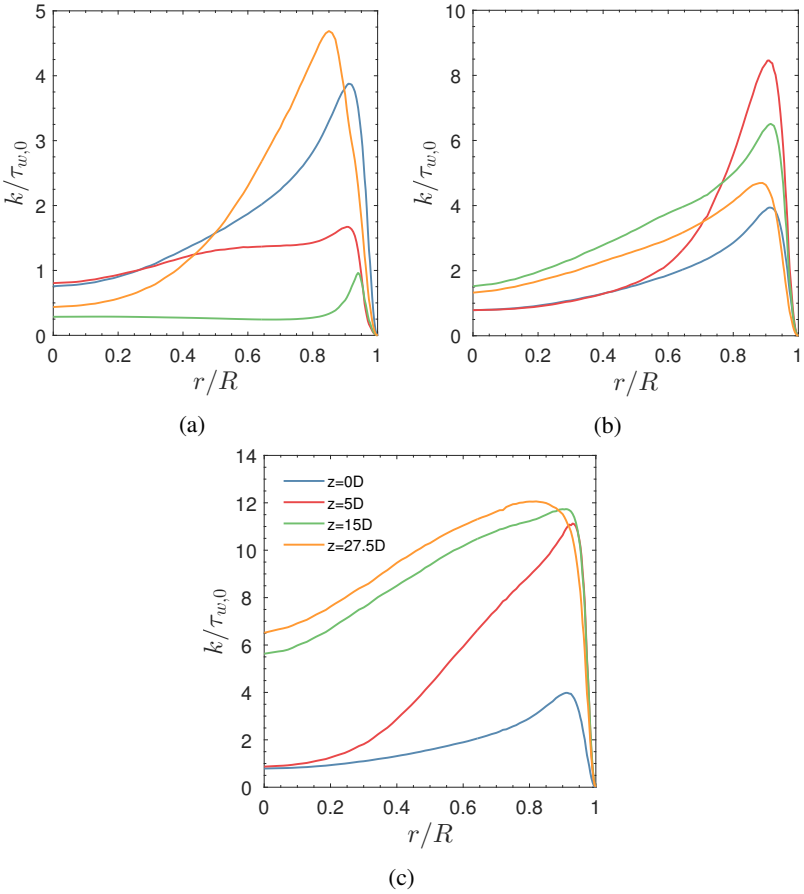

Fig. 3.8 Radial profile of turbulent kinetic energy at different axial locations for (a): Case DC80q2, (b): Case FC80q2, and (c): Case UC80q2. Note: Difference in ordinate scales

the wall. The wall temperature drops very rapidly to the liquid-like region while the core fluid is still in the gas-like region. This sharp density gradient between the wall and core enhances the mixing of fluid radially, and as a

result, all turbulent quantities show rising characteristics up to $15D$. Further to this cross-section, the bulk fluid temperature also approaches the region of liquid-like, which reduces the mixing; thereby the turbulence is decreased relatively. Furthermore, unstable stratification will also act as a source in this case and due to unstable stratification, buoyancy production is also positive. The buoyancy has a drastic effect on heat transfer at supercritical pressure. Therefore, a detailed examination of buoyancy-induced turbulence modulation is performed by means of several statistical tools.

3.4.1 Fukagata, Iwamoto, and Kasagi (FIK) identity

Variable thermophysical properties are proved to be responsible for the dissimilar trend in flow and heat transfer characteristics as seen earlier in the previous section. In this section, an attempt is made to understand the role of individual components, namely laminar, turbulent and inhomogeneous components, by means of the FIK identity. Fukagata et al. [46] derived an expression for the local skin friction coefficient for incompressible turbulent canonical flows, known as FIK identity for the local skin friction factor. The sole aim of this decomposition is to understand the fractional contributions to local skin friction factor and apply different control techniques to reduce the drag [47]. A similar expression was derived for compressible turbulent channel flows by Gomez et al. [51]; for supercritical fluids by Nemati et al. [95] in non-dimensional form which provided a new perception for the inhomogeneous contribution to local skin friction coefficients during flows without the buoyancy force. In addition to this, Nemati et al. [95] decomposed the Nusselt number for supercritical fluids and Lee et al. [77] derived an identity for Stanton number for variable-viscosity flows. These equations were re-derived in dimensional form in this work. Equation 3.1 shows the FIK identity for local skin friction coefficient (C_f) including buoyancy contribution. This equation was derived by double integration of the Favre-averaged streamwise momentum equation followed by the substitutions for the C_f.

$$
\begin{aligned}
C_{f,FIK} = & \underbrace{-\frac{64}{\rho_b U_b^2 D^3}\int_0^R r\overline{\mu}\overline{S}_{rz}rdr}_{C_1} \\
& \underbrace{+\frac{64}{\rho_b U_b^2 D^3}\int_0^R r\overline{\rho u_r'' u_z''}rdr}_{C_2} \\
& \underbrace{+\frac{32}{\rho_b U_b^2 D^3}\int_0^R (R^2-r^2)\left\langle\frac{\partial\overline{p}}{\partial z}\right\rangle rdr}_{C_3} \\
& \underbrace{+\frac{64}{\rho_b U_b^2 D^3}\int_0^R r\overline{\rho}\widetilde{u}_r\widetilde{u}_z rdr}_{C_4} \\
& \underbrace{+\frac{32}{\rho_b U_b^2 D^3}\int_0^R (R^2-r^2)\left\langle\frac{\partial\overline{\rho}\widetilde{u}_z\widetilde{u}_z}{\partial z}\right\rangle rdr}_{C_5} \\
& \underbrace{+\frac{32}{\rho_b U_b^2 D^3}\int_0^R (R^2-r^2)\left\langle\frac{\partial\overline{\rho u_z'' u_z''}}{\partial z}\right\rangle rdr}_{C_6} \\
& \underbrace{-\frac{32}{\rho_b U_b^2 D^3}\int_0^R (R^2-r^2)\left\langle\frac{1}{r}\frac{\partial r\overline{\mu' S'}_{rz}}{\partial r}\right\rangle rdr}_{C_7} \\
& \underbrace{-\frac{32}{\rho_b U_b^2 D^3}\int_0^R (R^2-r^2)\left\langle\frac{\partial\overline{\mu}\overline{S}_{zz}}{\partial z}\right\rangle rdr}_{C_8} \\
& \underbrace{-\frac{32}{\rho_b U_b^2 D^3}\int_0^R (R^2-r^2)\left\langle\frac{\partial\overline{\mu' S'}_{zz}}{\partial z}\right\rangle rdr}_{C_9} \\
& \underbrace{\pm\frac{32}{\rho_b U_b^2 D^3}\int_0^R g(R^2-r^2)\langle\overline{\rho}\rangle rdr}_{C_{10}}
\end{aligned}
\tag{3.1}
$$

In Equation 3.1, the operator $<>$ denotes fluctuations relative to the cross-sectional area and is defined as: $<\phi>=\phi-\frac{2}{R^2}\int_0^R \phi rdr$. The bulk velocity is

represented by U_b and calculated as $U_b = \frac{\int_0^A \rho u dA}{\int_0^A \rho dA}$ with A as the cross sectional area, C_1 is the laminar contribution, C_2 is the turbulent contribution, C_3 to C_9 are inhomogeneous contributions and C_{10} is the buoyancy contribution to the skin friction coefficient. In a fully-developed constant property flow, all terms vanish except C_1 and C_2.

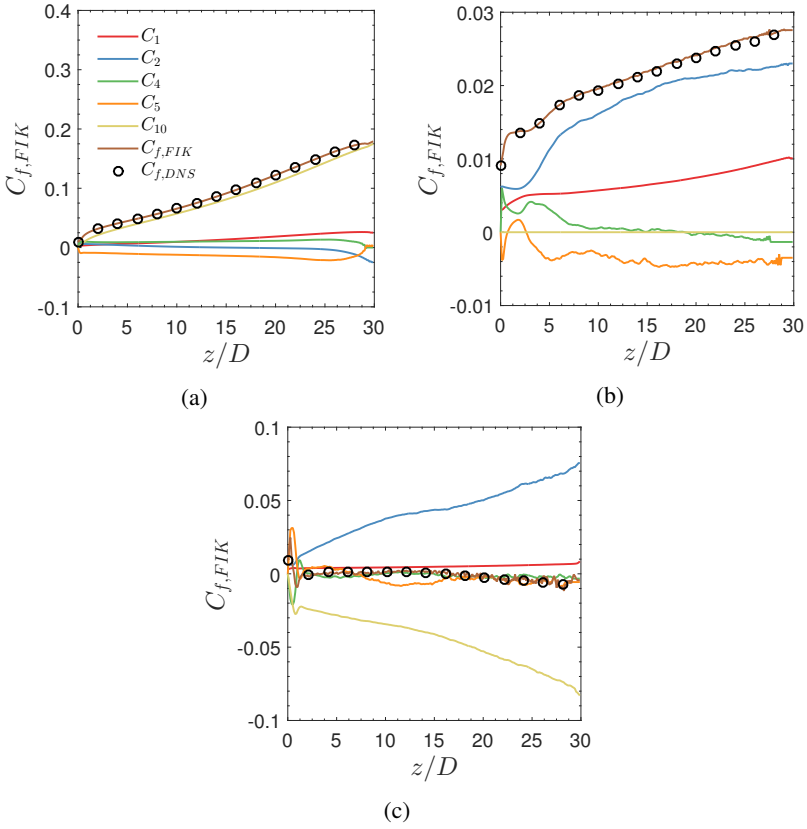

Fig. 3.9 Decomposition of skin friction coefficient for (a): case DC80q2 (b): case FC80q2, and (c): case UC80q2. Note: Difference in ordinate scales

The decomposition of the skin friction coefficient is depicted in Figure 3.9. The variation of the laminar part (C_1), the turbulent part (C_2), the inhomogeneous contributions (C_4, C_5) and the buoyancy part (C_{10}), and their summations ($C_{f,FIK}$) for all three cases can be seen in Figure 3.9; the remaining parts (C_3, C_{6-9}) which are not shown here, have negligible magnitudes. Along with the contributions, the locally computed skin friction factor, $C_{f,DNS} = \frac{2\tau_w}{\rho_b U_b^2}$, from the DNS, is also shown and a good agreement between $C_{f,FIK}$ (brown solid lines) and $C_{f,DNS}$ (overlapping symbols) can be observed for all three cases, which verifies the reliability of the derivation and its implementation. The maximum and minimum error was in between $\pm 3\%$ for all cases. The streamwise variation of C_f closely follows the trend of the wall shear stress. In case DC80q2, the total skin friction factor and its buoyancy contribution have the same trend with the same order of magnitude. A negative shear stress was observed earlier in case UC80q2 in Figure 3.9c and correspondingly negative value can be seen in the skin friction coefficient. This negative value comes out as a result of negative buoyancy contribution (see Figure 3.9c).

In all three cases, the laminar contribution, C_1, shows an increase along the axial direction when compared to the inlet. This is due to the decreasing bulk Reynolds number in the axial direction with cooling, thus flow is approaching the laminar state which gives rise to C_1. Additionally, the mean dynamic viscosity increases due to decreasing temperature in the streamwise direction which further contributes to the increasing C_1. However, the variation of C_2 is different for all cases. For downward flow, the turbulent contribution (C_2) decreases due to the reduction in Reynolds shear stress, as can be seen from Figure 3.6a. However, cases FC80q2 and UC80q2 show increasing trends which originate from the streamwise increase in the turbulent shear stress (refer to Figures 3.6b and 3.6c). The evolution of the streamwise momentum flux directly affects C_5. For larger axial distances, the mean velocity profile becomes steeper in the near-wall region and flatter in the core region for the downward flow. Therefore, the gradient is negative and the gradient turns to be positive again at the outlet with comparatively higher amplitude due

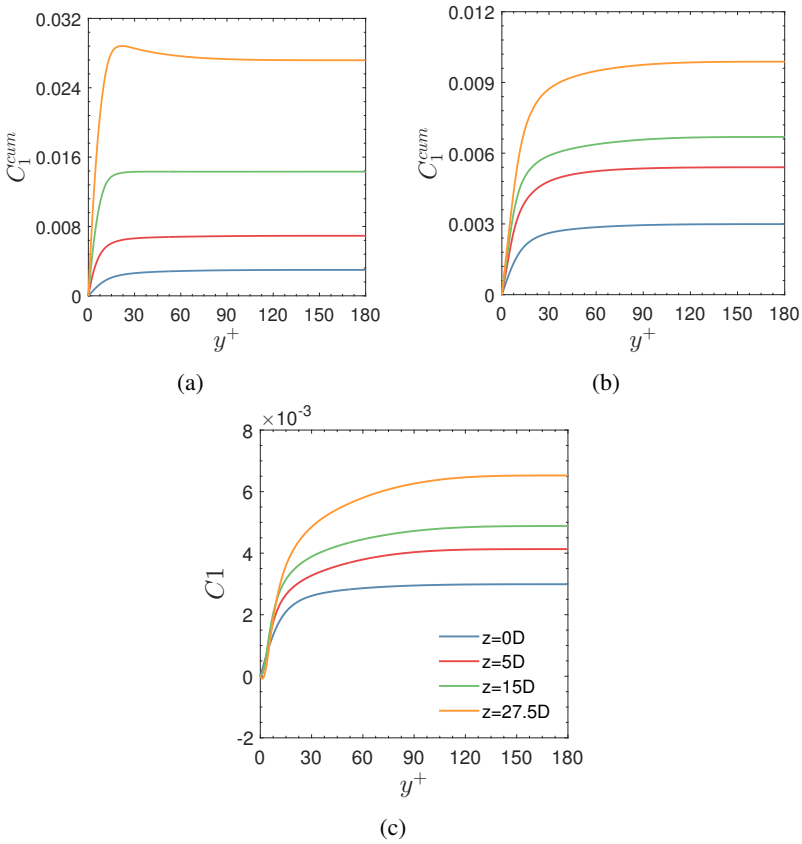

Fig. 3.10 Cumulative contribution of C_1 for (a): case DC80q2 (b): case FC80q2, and (c): case UC80q2. Note: Difference in ordinate scales

to a M-shaped velocity profile. Thus, an increment can be seen at the outlet for C_5 in Figure 3.9a. The term C_4 depends on the mean velocity profiles in radial and axial directions as well as on the mean density. There is a little change in the profile of $\overline{\rho}\widetilde{u}_r\widetilde{u}_z$ in the axial direction in case DC80q2; therefore, an almost constant value in Figure 3.9a can be observe. A similar trend

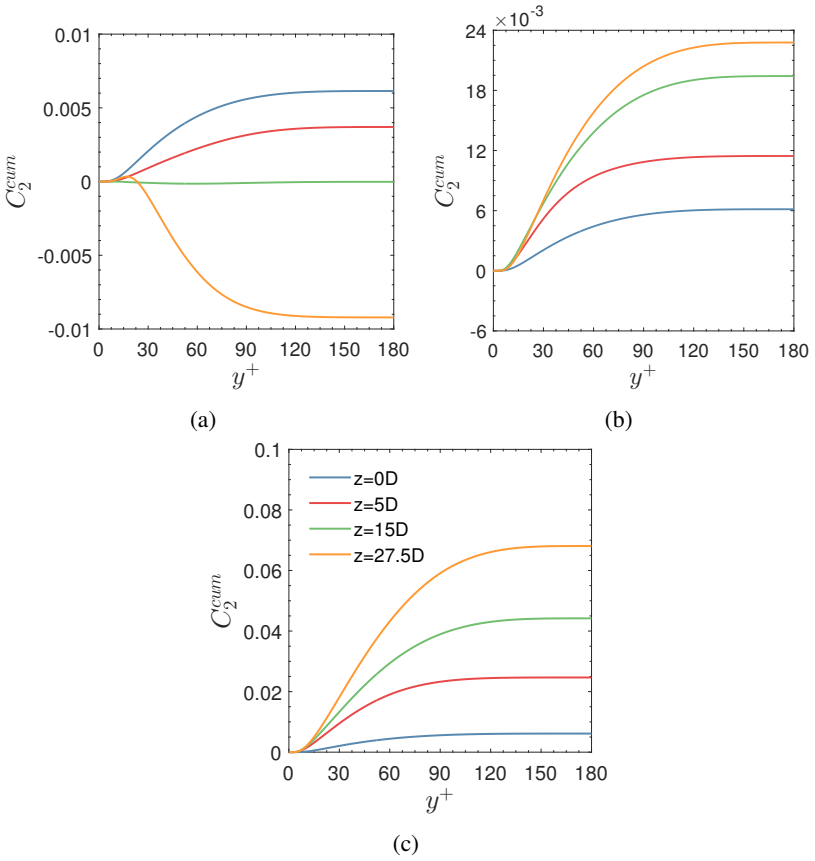

Fig. 3.11 Cumulative contribution of C_2 for (a): case DC80q2 (b): case FC80q2, and (c): case UC80q2. Note: Difference in ordinate scales

was observed for the upward flow except for a peak in the inlet region, in Figure 3.9c. In addition, the buoyancy contribution (C_{10}), has a significant effect on the overall skin friction factor in upward and downward flow. For downward flow, C_{10} has a positive magnitude and is responsible for a major part of the skin friction coefficient. In upward flow, C_{10} shows a similar

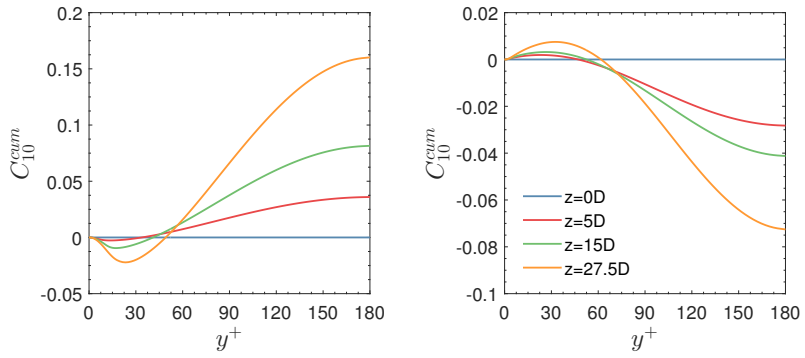

Fig. 3.12 Cumulative contribution of C_{10} for (a): case DC80q2, and (b): case UC80q2. Note: Difference in ordinate scales

trend, but with a negative sign. Forced convection has no gravity, therefore it posses zero contribution from C_{10} and as stated earlier it is responsible for a near-constant magnitude of C_f compared with the buoyancy-affected flow. In a typical turbulent flow without buoyancy effects, C_2 has the maximum contribution as observed for constant property channel flow [46] and heated turbulent boundary layers [76]. However, C_{10} has the major contribution for supercritical fluids affected by the buoyancy (i.e. case DC80q2 and UC80q2). As soon as the effects of buoyancy are neglected (i.e. case FC80q2), C_2 again becomes prominent. This observation is consistent with Lee et al. [76], who reported for heated turbulent boundary layers with temperature dependent viscosity in which density was held constant.

To gain further understanding of the different terms in the FIK identity, an investigation is made for the cumulative variation of the individual terms in the radial direction i.e. their integral from y to R. This cumulative contribution for C_1 is determined as; $C_1^{cum} = -\frac{64}{\rho_b U_b^2 D^3} \int_{1-y}^{R} r\overline{\mu}\overline{S}_{rz} r dr$, with y as distance from the wall. For a better illustration, the data is depicted in terms of non-dimensional distance from the wall based on inlet properties $\left(y^+ = \frac{y u_{\tau,0}}{\nu_0}\right)$.

The cumulative laminar contribution is shown in Figure 3.10, and it can be seen that within 30 wall-units more than 90% of its contribution to the drag is generated, most in the buffer layer (defined as $5 \leq y^+ \leq 30$). In the downward flow, turbulence is attenuated and it gives relatively higher values of C_1 compared with the forced and upward flow. In upward flow, the laminar contribution extends beyond the buffer layer in the downstream, but it is much lower than the downward flow case. The cumulative contribution of Reynolds shear stress (C_2^{cum}) is shown in Figure 3.11 and it is extended into the bulk region, unlike the laminar contribution. The C_2^{cum} becomes almost negligible at $z = 15D$ in case DC80q2, where impaired turbulence was observed and then this contribution increases in the negative direction due to the turbulence recovery. The turbulent shear stress (in Figure 3.6a) showed a negative value near to the outlet and one can observe from Figure 3.11a that the negative contribution comes out away from the wall i.e. after $y^+ \approx 17$. Figure 3.12 demonstrates the variation for C_{10}^{cum} (buoyancy) and it has a similar trend for downward and upward flow with different signs. Another observation is that a point of inflection exist in both cases at $y^+ < 70$ and it moves toward the core. The moving of inflection point is contributed by the density profile expanding more in the wall-normal direction.

Similar to the skin friction coefficient, an expression for the FIK identity for the Nusselt number was obtained by double integrating the Favre-averaged energy equation. Equation 3.2 shows the FIK identity for the Nusselt number (Nu). In Equation 3.2, the subscript 'b' and 'w' denote the bulk and wall, respectively and α represents the thermal diffusivity $\left(\alpha = \frac{\kappa}{\rho c_p},\ c_p \text{ is the isobaric specific heat}\right)$.The nomenclature are similar to the C_f; N_1 represents the laminar contribution, N_2 represents the turbulent contribution and N_3 to N_8 are the inhomogeneous contributions. Here, the buoyancy contribution is not present due to the assumption of low Mach number flow.

This identity was applied to present DNS cases and results are illustrated in Figure 3.13. Firstly, a fairly good qualitative agreement can be seen for Nu_{FIK} (orange solid lines) and the locally computed Nusselt number from the DNS

data (overlapping symbols) in Figure 3.13. The error was approximately $\pm 5\%$ between the locally computed values and FIK identity. All inhomogeneous parts are shown by term N_{3-8} and it is showing a maximum fraction at the inlet in every case.

$$
\begin{aligned}
\mathrm{Nu}_{FIK} = & \underbrace{\frac{32}{\alpha_b(h_b-h_w)D^2}\int_0^R r\overline{\alpha}\frac{\partial \overline{h}}{\partial r}rdr}_{N_1} \\
& \underbrace{-\frac{32}{\alpha_b(h_b-h_w)D^2}\int_0^R r\overline{\rho u_r'' h''}rdr}_{N_2} \\
& \underbrace{-\frac{32}{\alpha_b(h_b-h_w)D^2}\int_0^R r\overline{\rho}\widetilde{u}_r\widetilde{h}rdr}_{N_3} \\
& \underbrace{-\frac{16}{\alpha_b(h_b-h_w)D^2}\int_0^R (R^2-r^2)\left\langle\frac{\partial \overline{\rho}\widetilde{u}_z\widetilde{h}}{\partial z}\right\rangle rdr}_{N_4} \\
& \underbrace{-\frac{16}{\alpha_b(h_b-h_w)D^2}\int_0^R (R^2-r^2)\left\langle\frac{\partial \overline{\rho u_z'' h''}}{\partial z}\right\rangle rdr}_{N_5} \\
& \underbrace{+\frac{16}{\alpha_b(h_b-h_w)D^2}\int_0^R (R^2-r^2)\frac{1}{r}\left\langle\frac{\partial r\overline{\alpha'\frac{\partial h'}{\partial r}}}{\partial r}\right\rangle rdr}_{N_6} \\
& \underbrace{+\frac{16}{\alpha_b(h_b-h_w)D^2}\int_0^R (R^2-r^2)\left\langle\frac{\partial \overline{\alpha}\frac{\partial \overline{h}}{\partial z}}{\partial z}\right\rangle rdr}_{N_7} \\
& \underbrace{+\frac{16}{\alpha_b(h_b-h_w)D^2}\int_0^R (R^2-r^2)\left\langle\frac{\partial \overline{\alpha'\frac{\partial h'}{\partial z}}}{\partial z}\right\rangle rdr}_{N_8}
\end{aligned}
\tag{3.2}
$$

Once again, one can observe that a decrease in the turbulent parts (N_2) seeds the impaired heat transfer characteristics in the downward flow. In downward flow (case DC80q2), the contribution of turbulent heat flux is small

as compared to the other two cases evidently from the variation of the turbulent heat flux in Figure 3.14. The turbulent heat flux increases at $z = 27.5D$ as shown in Figure 3.14a. As a result of it, the turbulent contribution to the Nusselt number (N_2) also increases for downward flow near to outlet (see Figure 3.13a) and it indicates heat transfer recovery as a result of turbulence recovery. In upward flow (case UC80q2), N_2 increases in the downstream, shows a peak at $z \approx 15D$ and after that, it starts decreasing. The N_2 depends on $\frac{1}{\alpha_b(h_b - h_w)}$ and radial turbulent heat flux. The radial turbulent heat flux does not change significantly in case UC80q2 as demonstrated in Figure 3.14b, therefore, N_2 mainly depends on $\frac{1}{\alpha_b(h_b - h_w)}$. This term decreases initially and then starts increasing, therefore, the N_2 varies inversely to it. A similar trend can be seen in Figure 3.13b for forced convection for turbulent contribution (i.e. N_2). The laminar contribution to the Nusselt number (N_1) shows a similar trend for all three cases with the same order of magnitude.

From the cumulative contribution of the laminar part shown in Figure 3.15, one can notice that solely the near-wall region is responsible for the generation of N_1. The buoyancy-opposed-flow (i.e. upward flow) has comparatively smaller magnitude than the buoyancy-favored flow (i.e. downward flow). Also, over 90% of the laminar contribution stems from $y^+ \leq 15$ in upward flow and this region extended to $y^+ \leq 30$ in the downward flow. Figure 3.16 illustrates the cumulative contribution of the turbulent part (N_2^{cum}). As expected, the downward flow has the smallest magnitude as compared to the other two cases and it decreases in the streamwise direction. The direction of body force due to gravity and flow direction are opposed in the upward flow and this creates an unstable flow analogous to downward flow with heating. Hence, this results in values of N_2 for case UC80q2 that is higher as compared to case DC80q2. Through this analysis, one can observe that buoyancy has a significant contribution to skin friction coefficient at supercritical pressure. It is positive for downward flow and negative for upward flow. The turbulent contribution to skin friction changes its trend in all three cases. This variation is quite different than the constant property flow with heat transfer at the

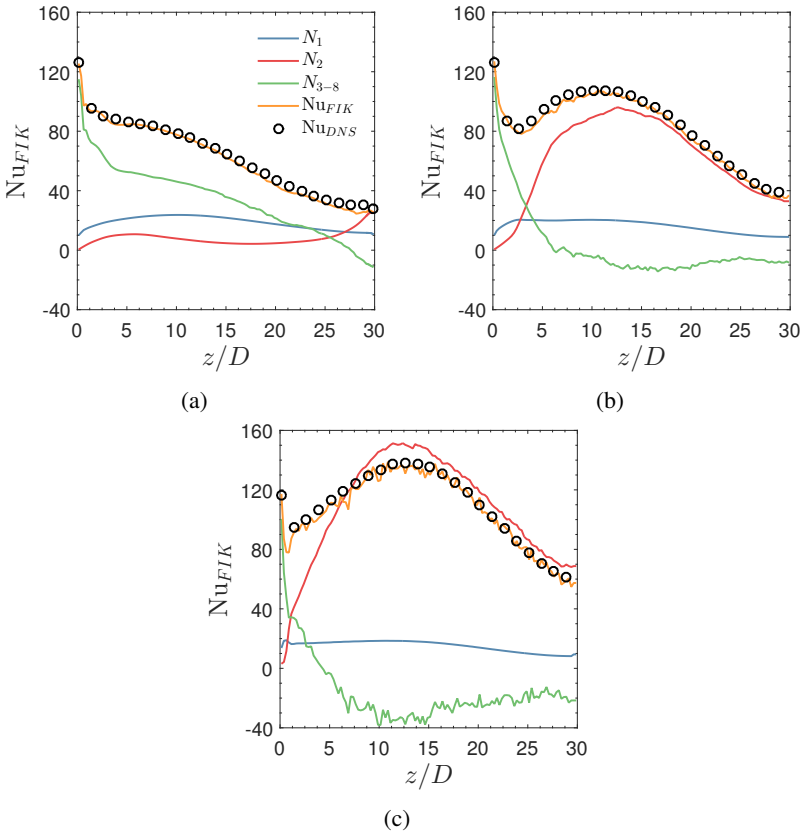

Fig. 3.13 Decomposition of Nusselt number for (a): case DC80q2 (b): case FC80q2, and (c): case UC80q2

same friction Reynolds number reported by Nemati et al. [95] in which laminar and turbulent contribution remains almost constant. The turbulent contribution to the Nusselt number (N_2) plays a major role in determining the enhanced or deteriorated heat transfer. This turbulent contribution is affected by the turbulent shear stress (for C_f) and turbulent heat flux (for Nu), which

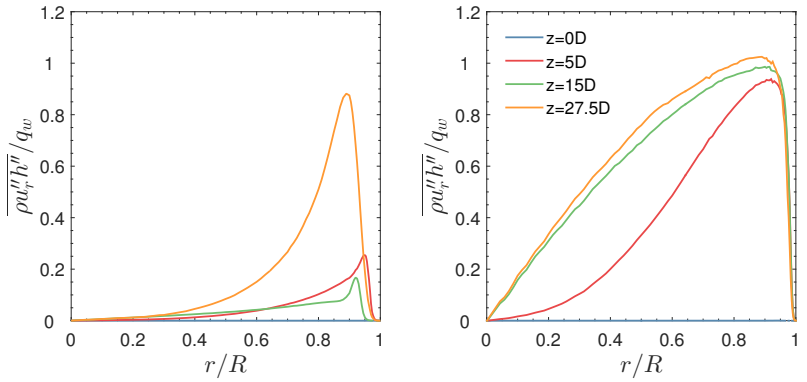

(a) (b)

Fig. 3.14 Radial turbulent heat flux for (a): case DC80q2, and (b): case UC80q2

itself is modulated as a result of buoyancy. Therefore, in next subsection, an examination for the change of both turbulent shear stress and turbulent heat flux is conducted.

3.4.2 Quadrant analysis

Earlier, the Reynolds shear stress and turbulent heat flux was shown in Figures 3.6 and 3.14, respectively. Both showed a different behavior for each case as a result of buoyancy and/or flow deceleration. Quadrant analysis [130, 129] can provide insightful details regarding the constitutional quadrant contribution of Reynolds shear stress and turbulent heat flux which will enable to understand the possible reason for the dissimilar trend. Pandey et al. [97] used this method to illustrate the effect of hot and cold turbulence motion at supercritical pressure. Firstly, this technique is applied to the Reynolds shear stress for all three cases at different axial locations by filtering out the data of $\sqrt{\rho}u_r''$ and $\sqrt{\rho}u_z''$. Figure 3.17 shows the contributions of each quadrant to turbulent shear stress for all three cases. At the inlet, the quadrants Q_2 and

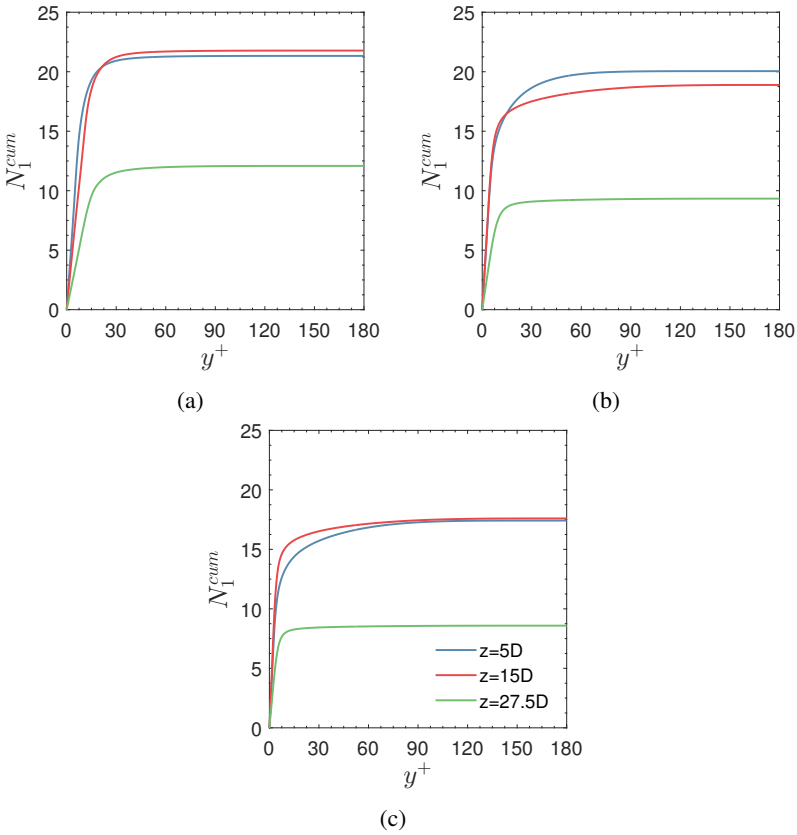

Fig. 3.15 Cumulative contribution of N_1 for (a): case DC80q2 (b): case FC80q2, and (c): case UC80q2

Q_4, commonly known as updraft motion or ejection ($+\sqrt{\rho}u_r''$ and $-\sqrt{\rho}u_z''$) and downdraft motion or sweep ($-\sqrt{\rho}u_r''$ and $+\sqrt{\rho}u_z''$) respectively, have the primary contribution whilst the other two, "outward" (Q_1) and "inward" (Q_3) interaction (relative to the wall) have the smallest contribution. The ejection and sweep events take place near the wall, typically $10 < y^+ < 30$.

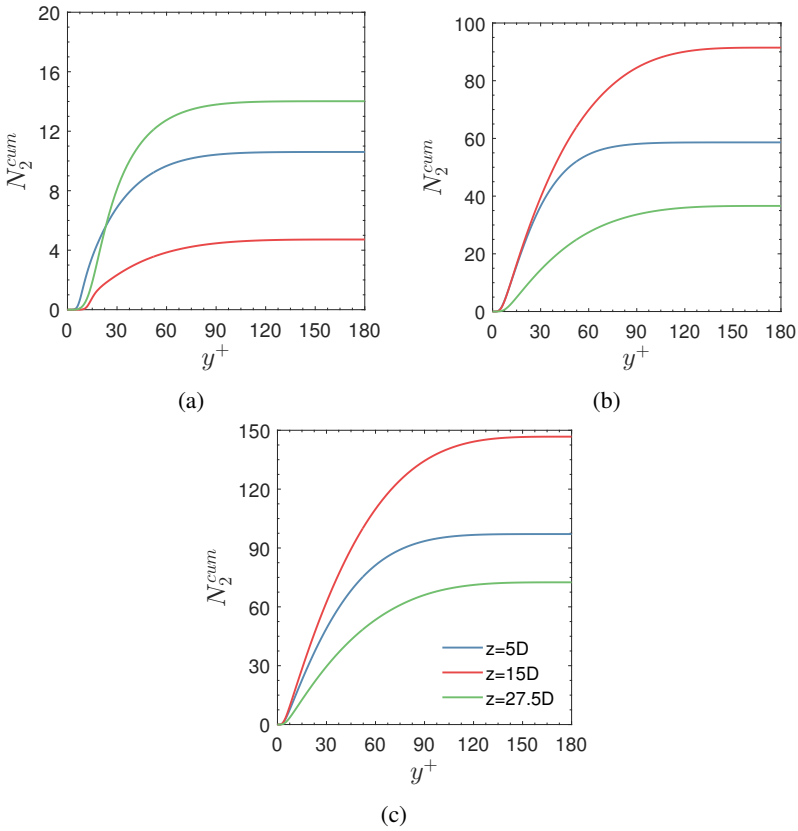

Fig. 3.16 Cumulative contribution of N_2 for (a): case DC80q2 (b): case FC80q2, and (c): case UC80q2. Note: Difference in ordinate scales

During ejection, fluid with low streamwise momentum moves away from the wall with high cross-streamwise momentum as a result of the turbulent bursts, while during the sweep, fluid with high streamwise momentum moves towards the wall with a smaller cross-streamwise momentum. Both events are complementary to each other, ejection is expected after the sweep to replace

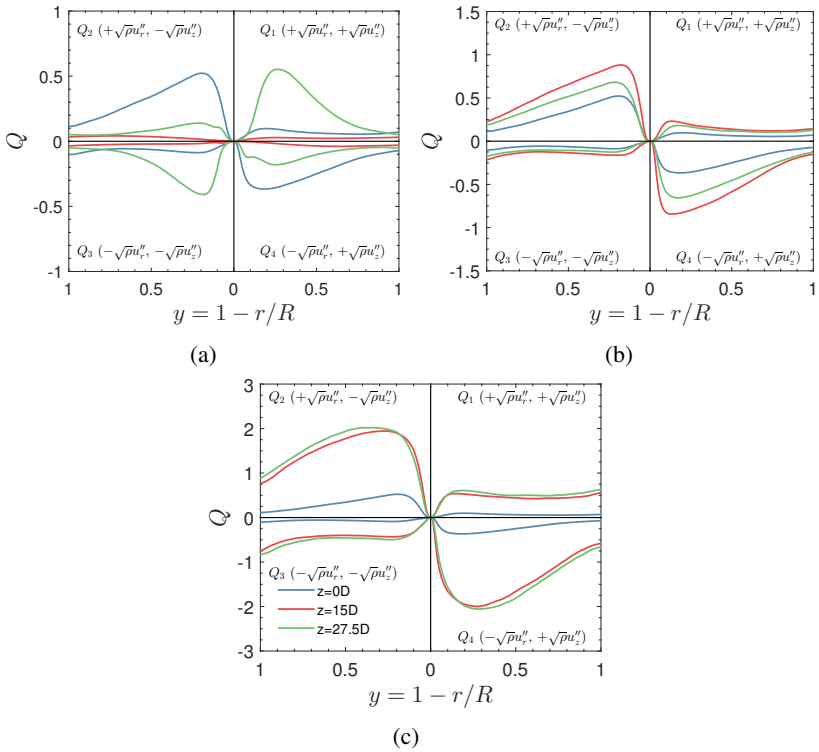

Fig. 3.17 Quadrant analysis for Reynolds shear stress for (a): case DC80q2 (b): case FC80q2, and (c): case UC80q2. Note: Difference in ordinate scales

the fluid which left or vice versa. Turbulence shear stress keeps growing in the streamwise direction in forced and upward flow (see Figures 3.6b and 3.6c). The foremost reason behind this is that the sweep and ejection also show the enhanced magnitude and visible from Figures 3.17b and 3.17c. These events not only play a critical role in Reynolds stress generation but also positively affect the momentum transfer.

The most interesting case is the downward flow (refer to Figure 3.17a), in which turbulence shear stress diminishes in the initial section until $z = 15D$,

but near to the outlet turbulence recovers as can be seen from Figure 3.6a. Contrary to sweep and ejection events, the interaction events (Q_1 and Q_3) are responsible for this recovery. At $z = 27.5D$, the Q_2 and Q_4 are still significant in the near-wall region but away from the wall Q_1 and Q_3 have a much higher contribution. This explains the change of turbulence shear stress from a negative (at core region) to a positive (at near-wall region) value in the downward flow case at the outlet as shown in Figure 3.6a. A possible reason for this quadrants change is the deformation of mean velocity profile into M-shaped shown in figure at $z = 27.5D$. The M-shaped deformation of velocity profile causes the directional change of shear but this reasoning needs to be investigated closely. Typically, a reduction in Q_2 and Q_4 also triggers a reduction in the skin friction in normal flows by virtue of decreasing C_1 and C_2 contributions to C_f (refer to Figures 3.10 and 3.11). But with supercritical fluids, the buoyancy contribution (C_{10}) affects the distribution of C_f (refer to Figures 3.12) and causes a completely opposite trend.

The quadrant analysis provides an absolute averaged magnitude, therefore, to examine the frequency of these events over time, joint probability density functions (JPDF) of $\sqrt{\rho}u_r''$ and $\sqrt{\rho}u_z''$ is examined. The Reynolds shear stress and JPDF are related as: $\overline{\rho u_r'' u_z''} = \int_{+\infty}^{-\infty} \rho u_r'' u_z'' \mathrm{P}(\sqrt{\rho}u_r'', \sqrt{\rho}u_z'') d(\sqrt{\rho}u_r'') d(\sqrt{\rho}u_z'')$. The iso-contour plot of the covariance integrand, better known as weighted JPDF $\left(\rho u_r'' u_z'' \mathrm{P}(\sqrt{\rho}u_r'', \sqrt{\rho}u_z'')\right)$ is shown in Figure 3.18-3.20 for all three cases at $r/R = 0.8$ (correspondingly, $y^+ = 36$) and they are normalized with $\tau_{w,0}$. The data for this analysis were gathered at every 100th time step for at least 10 flow through times. A very first observation from these figures (Figure 3.18-3.20) is that the frequency of occurrence in each quadrant diminished drastically in the downward flow case and increased in the forced and the upward flow case as compared to the inlet (refer to Figure 3.18a, same for all three cases). In the deteriorated heat transfer regime in case DC80q2 ($z \approx 15D$, shown in Figure 3.18b), each event has negligible magnitude along with the reduced occurrence during the entire sampling time. Each quadrant comparatively has higher magnitude of $\sqrt{\rho}u_z''$ than $\sqrt{\rho}u_r''$ at $z = 15D$. But in

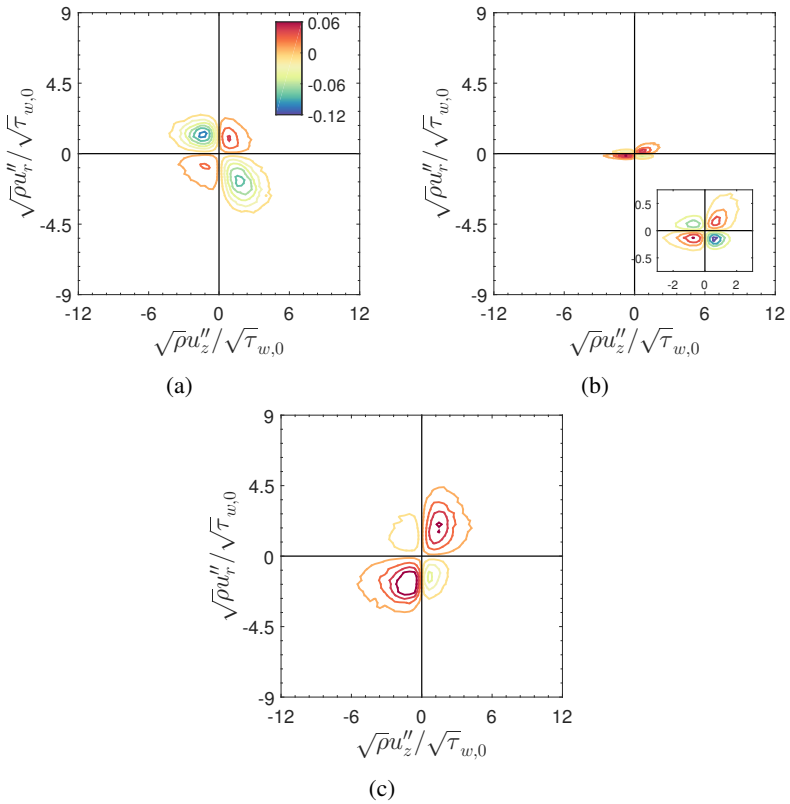

Fig. 3.18 Contours of weighted joint probability density functions of Reynolds shear stress for case DC80q2 at $r/R = 0.8$ along the pipe length. (a): $z = 0D$, (b): $z = 15D$ with inset figure showing the zoomed view, and (c): $z = 27.5D$

the recovery regime ($z \approx 27.5D$, shown in Figure 3.18c), inward and outward quadrants (Q_1 and Q_3) become more energetic and they contribute to the generation of turbulent shear stress and, consequently, in the recovery of heat transfer. Although the frequency is approximately the same in Q_4 but the magnitude is incomparable to Q_1 and Q_3 as shown in Figure 3.18c. The other two

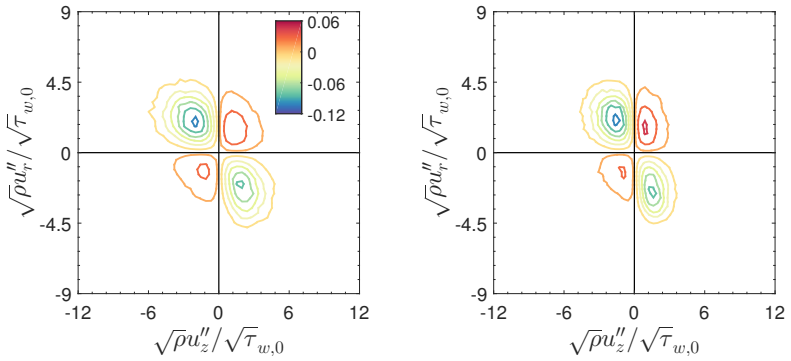

(a) (b)

Fig. 3.19 Contours of weighted joint probability density functions of Reynolds shear stress for case FC80q2 at $r/R = 0.8$ along the pipe length. (a): $z = 15D$, and (b): $z = 27.5D$

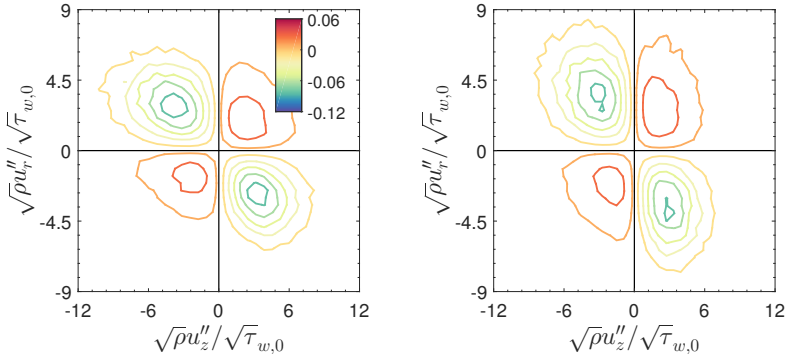

(a) (b)

Fig. 3.20 Contours of weighted joint probability density functions of Reynolds shear stress for case UC80q2 at $r/R = 0.8$ along the pipe length. (a): $z = 15D$, and (b): $z = 27.5D$

cases (case FC80q2 and UC80q2) are shown in Figures 3.19 and 3.20, exhibit

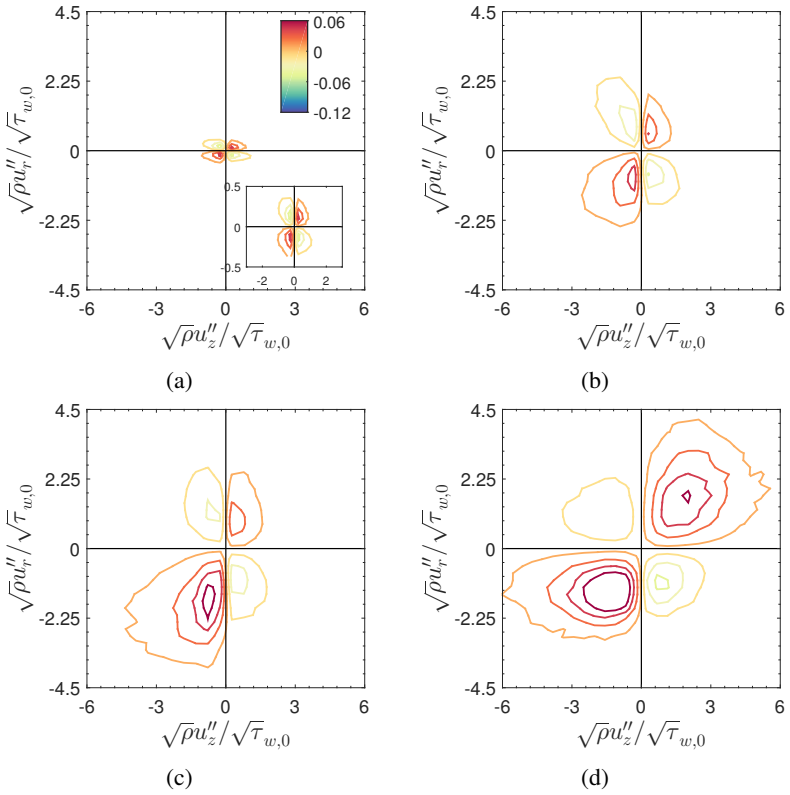

Fig. 3.21 Contours of weighted joint probability density functions of Reynolds shear stress for case DC80q2 at $z = 27.5D$ along the radial direction. (a): $r/R = 0.975$ with inset figure showing the zoomed view, (b): $r/R = 0.935$, (c): $r/R = 0.91$, and (d): $r/R = 0.77$

similar qualitative characteristics to each other with an amplitude difference. Figure 3.19 shows the weighted JPDF for forced convection and both Q_2 and Q_4 shrink particularly with respect to the $\sqrt{\rho}u_z''$-axis. This shrink suggests that the strength of low and high-speed streaks decreased at $z = 27.5D$ as compared to $z = 15D$ and this reduces the Reynolds shear stress at the outlet

(see Figure 3.6b). Figure 3.20 shows the contour plot for upward flow. Both ejection and sweep events become stronger as one proceeds downstream and also the contours of every event elongate especially in the $\sqrt{\rho}u_r''$-axis. This elongation implies intense wall-normal motions to both high and low-speed streaks.

In Figure 3.6a, for the downward flow (case DC80q2), an inflection point can be seen near to the outlet (at $z = 27.5D$) at a radial location of $r/R = 0.91$ in the distribution of turbulent shear stress, along with minima and maxima at $r/R = 0.77$ and $r/R = 0.935$, respectively. To investigate this unusual trend, JPDFs for the turbulent shear stress at these locations are shown in Figure 3.21. In the vicinity of the wall (refer to Figure 3.21a), the Reynolds shear stress has negligible magnitude. The frequency of interaction events (Q_1 and Q_3) is of the same order of magnitude of the ejection and sweep events (Q_2 and Q_4). The Q_1 and Q_3 expand more in the radial direction as compared to the streamwise direction as one moves away from the wall (from $r/R = 0.975$ to $r/R = 0.91$). The expansion indicates that the near-wall interactions have more fluctuations towards wall and lower streamwise fluctuations and, as a result, low-speed streaks sink-down quickly. Similarly, high-speed streaks lift-up rapidly in Q_1 in the near wall region. However, during the transition of turbulent shear stress from 0 at $r/R = 0.91$ (corresponding Figure 3.21c) to the negative peak at $r/R = 0.77$ (corresponding Figure 3.21d), these contours widen relatively more in the streamwise direction and it indicates that the streaks increase in strength.

Earlier, it was highlighted that how the motions in each quadrant affect the turbulent shear stress in each case and it provided a new understanding of the role of interaction events in the recovery regime. Therefore, it is also important to look into the nature of turbulent heat flux. Figures 3.22 and 3.23 depict the iso-contours of the weighted JPDF for cases DC80q2 and UC80q2 for both streamwise and radial turbulent heat flux. The specific enthalpy is normalized with $\sqrt{\rho_0}h_{\tau,0}$ where $h_{\tau,0} = q_w/(\rho_0 u_{\tau,0})$. Figures 3.22a and 3.22c show the wall-normal turbulent heat flux at $z = 5D$ and $27.5D$ for case DC80q2. At

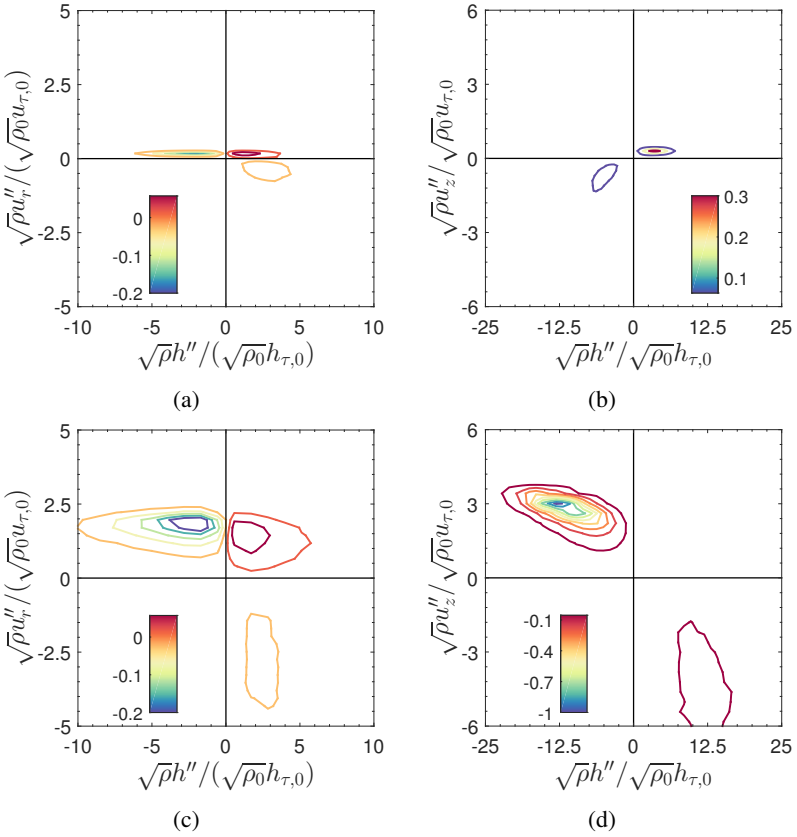

Fig. 3.22 Contours of (a): $\rho u_r'' h'' \mathrm{P}(\sqrt{\rho}u_r'', \sqrt{\rho}h'')$ at $z = 5D$, (b): $\rho u_z'' h'' \mathrm{P}(\sqrt{\rho}u_z'', \sqrt{\rho}h'')$ at $z = 5D$, (c): $\rho u_r'' h'' \mathrm{P}(\sqrt{\rho}u_r'', \sqrt{\rho}h'')$ at $z = 27.5D$, and (d): Contours of $\rho u_z'' h'' \mathrm{P}(\sqrt{\rho}u_z'', \sqrt{\rho}h'')$ at $z = 27.5D$ for case DC80q2 at $r/R = 0.8$

$z = 5D$ hot and cold wall-normal motions are responsible for the generation of turbulent heat flux in the wall normal direction. Interestingly, the transition of quadrants from Q_2, Q_4 to Q_1, Q_3 is not observed during the turbulent recovery at $z = 27.5D$ as observed earlier in Figure 3.21c for Reynolds shear stress.

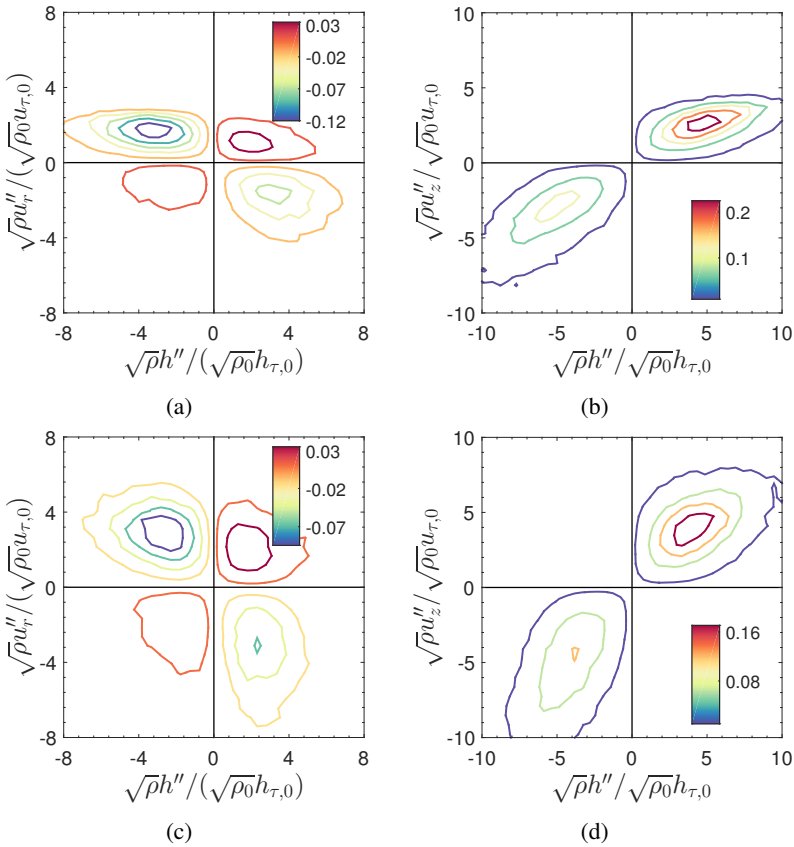

Fig. 3.23 Contours of (a): $\rho u_r'' h'' \mathrm{P}(\sqrt{\rho}u_r'', \sqrt{\rho}h'')$ at $z = 5D$, (b): $\rho u_z'' h'' \mathrm{P}(\sqrt{\rho}u_z'', \sqrt{\rho}h'')$ at $z = 5D$, (c): $\rho u_r'' h'' \mathrm{P}(\sqrt{\rho}u_r'', \sqrt{\rho}h'')$ at $z = 27.5D$, and (d): Contours of $\rho u_z'' h'' \mathrm{P}(\sqrt{\rho}u_z'', \sqrt{\rho}h'')$ at $z = 27.5D$ for case UC80q2 at $r/R = 0.8$

Instead, the contributions of existing quadrants become stronger downstream with increasing radial velocity. The streamwise turbulent heat flux suffers from attenuated turbulence and the amplitude of it is suppressed significantly

as can be seen from Figure 3.22b. But during the recovery region at $z = 27.5D$, the second and the fourth quadrant appear instead of the first and the third quadrants as illustrated in Figure 3.22d. Thus, it is clear that the radial heat flux remains in the same quadrant but a transition occurs in the streamwise flux.

Figures 3.23a and 3.23c illustrate the turbulent heat flux in the radial direction for upward flow (i.e. case UC80q2). A typical behavior can be observed, where the highest probabilities stem from Q_2 and Q_4. It implies that cold fluid lifts up from the cooled wall with higher radial momentum while hot fluid comes down with a lower radial momentum. Further downstream, both hot and cold fractions expand in $\sqrt{\rho}u_r''$- axis, which suggests that Q_2 and Q_4 lift-up and fall-down strongly. The characteristics of streamwise heat flux remain the same in terms of quadrant contributions with the main difference of increased magnitude in the downstream direction. Moreover, one can observe from Figures 3.23b and 3.23d that contours of streamwise momentum fluctuations become broader and contours of enthalpy fluctuations slightly narrower in the downstream flow.

3.4.3 Anisotropy

Until now, turbulence modulation was shown by means of the FIK identity and quadrant analysis. However, no attention was given to the anisotropic nature of turbulence. Therefore, in this section, turbulence anisotropy is investigated using the Reynolds stress anisotropy tensor (b_{ij}) defined as: $b_{ij} = \frac{\overline{\rho u_i'' u_j''}}{\overline{\rho u_k'' u_k''}} - \frac{1}{3}\delta_{ij}$; with δ_{ij} is the Kronecker delta. A similar approach as that of Antonia et al. [7] is followed by employing the invariants of anisotropy tensor to quantify the anisotropy in a flow. Characteristically, the first invariant (I_b) is zero while the second invariant (II_b) is calculated as $-(b_{ij}b_{ji})/2$, and the third invariant (III_b) is defined as: $(b_{ij}b_{jk}b_{ki})/3$. The second invariant indicates the degree of anisotropy and the third invariants has the information regarding the nature of the anisotropy. The third invariant has a negative value for the

disk-like structure (oblate structure) of turbulence and a positive value when the turbulence has the rod-like structure (prolate structure). Figure 3.24 shows the evolution of $-II_b$ and III_b at three axial locations for case UC80q2 (solid-lines) and DC80q2 (dashed-lines). Both invariants show peaks close to the wall, $7 \leq y^+ \leq 11$, which reaffirm that most of the anisotropy always exists in the near-wall region for wall-bounded flows. Moreover, invariants have a two-layer feature with different characteristics close to the wall ($0 \leq y^+ \leq 60$) and in the core region $60 \leq y^+ \leq 180$. For the case UC80q2, the second invariant decreases at close to the wall (see figure 3.24a), it suggests that anisotropy also decreases in the streamwise direction and is similar to the common trend of decreasing anisotropy with an increase in Reynolds number (or turbulence) [7]. On the other hand, anisotropy has a maximum value at $z = 15D$ for DC80q2 close to the wall. This was the location where deteriorated heat transfer and turbulence was observed. The increase in the anisotropy indicates the increase in the overlap between the energy-containing large eddies and

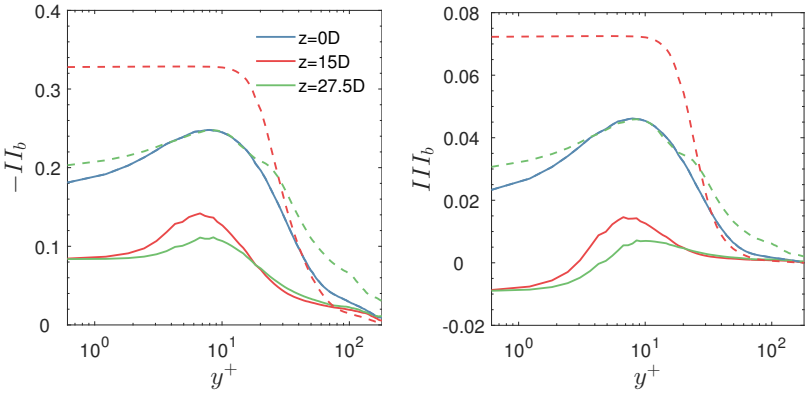

Fig. 3.24 Radial distribution of invariants (a): $-II_b$, and (b): III_b. Solid lines: case UC80q2, and dashed line: case DC80q2. Note: Difference in ordinate scales

the dissipative small scales [7]. As soon as this peak decreased at $z = 27.5D$, turbulence recovery was noticed. The variation of the third invariant shown in figure 3.24b and its trend changes downstream for both cases. In case UC80q2, this parameter becomes negative close to the wall and it indicates that turbulence structure is becoming disk-like in which two principal stresses have significant magnitudes. Due to this disk-like feature, turbulence structure is stretched in two directions and squeezed in the other direction. As expected, the downward flow (case DC80q2) has a completely different turbulence close to the wall compared to the upward flow (case UC80q2). At $z = 15D$, the third invariant has a positive value which indicates that turbulence became rod-like, i.e., elongated in one direction only. A transition back to the normal state can be seen at $z = 27.5D$ where the turbulence recovery was observed. The turbulent state remains anisotropic in the near-wall region for both the cases, while at the center of the pipe, turbulence becomes isotropic.

For the deteriorated case DC80q2, Lumley triangle [85] is also drawn which graphically visualize the degree of anisotropy and the characteristic shape of the anisotropy, thus, combines the second and third invariants. Lumley triangle uses η and ξ to illustrates the anisotropy, and they are define as: $\eta^2 = (\lambda_1^2 + \lambda_1\lambda_2 + \lambda_2^2)/3$, and $\xi^3 = (-\lambda_1\lambda_2(\lambda_1 + \lambda_2))/2$; where λ represent the eigenvalue of the b_{ij}. Figure 3.25a shows the mapping of η and ξ, the area bounded by the black line is known as the Lumley triangle. The vertex of this triangle at the origin is corresponding to the isotropic turbulence, the top right vertex is corresponding to the 1-dimensional turbulence and the left top vertex indicates the 2-dimensional axisymmetric turbulence. At the inlet, turbulence structure is 2-dimensional in near-wall region, while in the core region turbulence has prolate structure. Figure 3.25b shows the Lumely triangle for the deteriorated heat transfer at $z = 15D$. One can see that turbulent structure become 1-component (or rod-like) in the near-wall while in the core region turbulence structure remains the same. As soon as the heat transfer recovers at $z = 27.5D$, a transition back to the 2-component can be observed in the Figure 3.25c.

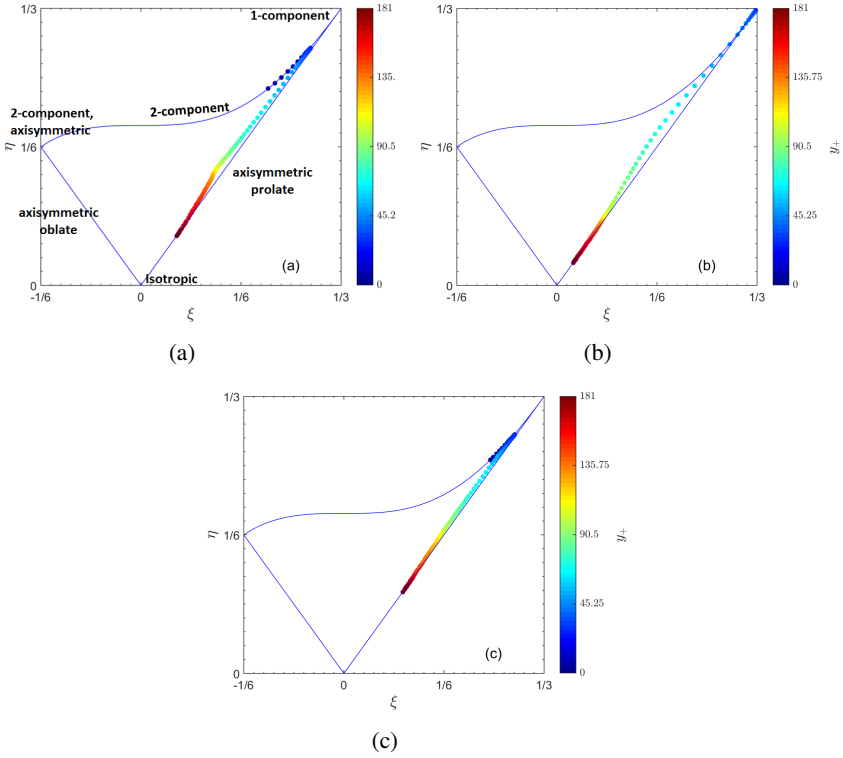

Fig. 3.25 Lumely triangle to visualize the anisotropy of Reynolds stress tensor in the flow for Case DC80q2 at (a): $z = 0D$, (b): $z = 15D$, and (c): $z = 27.5D$

3.4.4 Flow visualization

The enhanced and deteriorated heat transfer has a clear effect of near-wall streaks. In this subsection, turbulent streaks were visualized by $\sqrt{\rho}u_z''$. Figure 3.26 shows the streaks for case DC80q2 at three different wall-normal locations in the circumferential plane. The formation and breakdown of streaks can be observed in the inlet section ($z \approx 0-5D$) at all three positions with a

reduction in the strength. In the first $5D$ section, streaks start stretching close to the wall (refer to Figure 3.26a) and this elongation later spreads to the bulk region (refer to Figure 3.26c). Moreover, the intensity of the streaks decreases significantly. The low-speed streaks disappear from the flow in the deteriorated heat transfer regime ($z \approx 10 - 22.5D$) especially in the viscous sub-layer as depicted in Figure 3.26a. Additionally, the high-speed streaks elongate, particularly in the streamwise direction indicating 'rod-like'turbulence structures in the near-wall area for deteriorated heat transfer. The turbulent shear stress decreases significantly in this region (as noticed earlier in Figure 3.6a). The high-speed streaks become intense in their magnitude and ultimately start breaking down into small scales in the buffer layer (see Figures 3.26b and 3.26c at $z \approx 20D$). The low-speed streaks reappear after $z \approx 20D$ and hinder the further growth of the high-speed streaks. Both high- and low-speed streaks are present in the recovery zone in the near wall region. In the buffer-layer, streaks grow in the circumferential direction and their magnitude also increases. The recovery phase is extended into the bulk region and it shifts the peak in Reynolds shear stress from the near-wall region.

Figure 3.27 shows iso-surfaces of low- and high-speed streaks along with the iso-surface of λ_2 to visualize coherent turbulent structures [62]. Here, λ_2 is the second eigenvalue of the symmetric tensor $s^2 + \omega^2$ with, s and ω as the symmetric and antisymmetric part of instantaneous velocity gradient tensor. The observations regarding the high-speed streaks elongation and low-speed streaks disappearance are consistent with the Figure 3.26. The λ_2 vortex (shown in red in Figure 3.27) starts reducing in the downstream direction and coherent structures start shifting away from the wall. The low-speed streaks (iso-surface in blue color in Figure 3.27) are suppressed and strength of the coherent structure also reduced significantly. Moreover, high-speed streaks (shown by green color in Figure 3.27) survive in the flow in the deteriorated heat transfer regime and they are stretched out in the streamwise direction in the near-wall region as observed earlier Figure in 3.26. After the reappearance of low-speed streaks at $z \approx 15D$, λ_2 vortex also starts increasing

and interestingly the coherent structures are superimposed mainly on the high-speed streak as highlighted with black circles.

Contrary to case DC80q2, upward flow does not have the elongated streaks in the streamwise direction. Figure 3.28 illustrates the streaks with the same scale as of figure 3.26. Both low- and high-speed streaks remain in the flow throughout the pipe at all three depicted locations. Due to the buoyancy and deceleration effects, the intensity of these streaks also increases in the streamwise direction. These streaks also widen in the circumferential direction as compared to the case DC80q2. Furthermore, both low- and high-streaks are more intense in upward flow. Figure 3.29 demonstrates streaks for case FC80q2 which only has the effect of deceleration. These streaks have more intensity as compared to the case DC80q2 and their characteristic follows the case UC80q2.

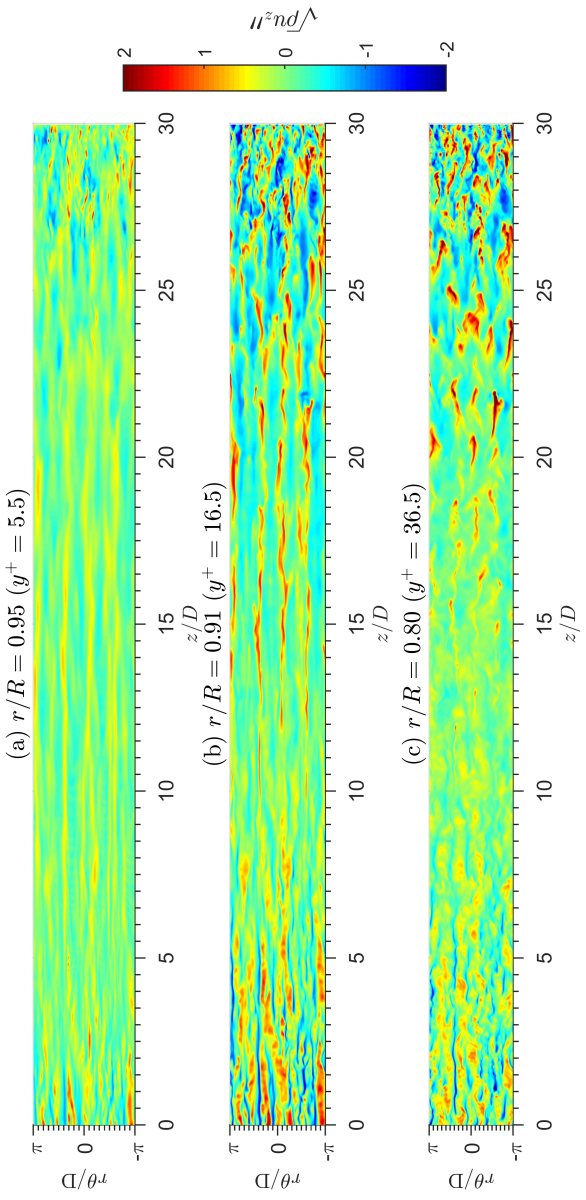

Fig. 3.26 Visualization of the instantaneous streaks for case DC80q2 at different wall normal locations by contours of $\sqrt{\bar{\rho}}u_z''$

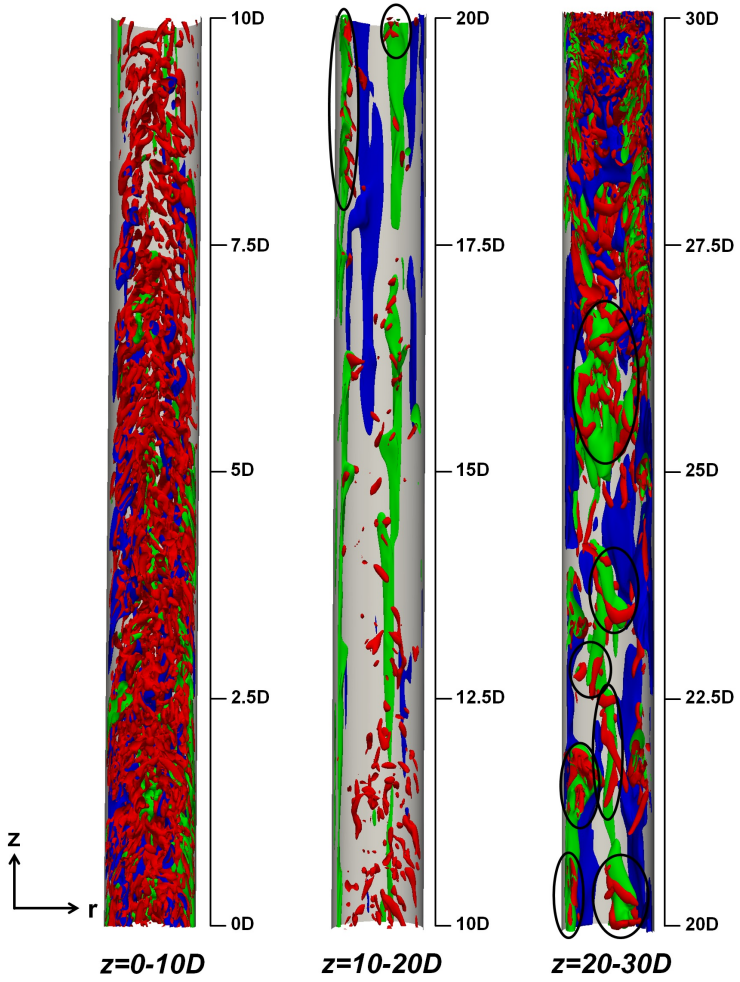

Fig. 3.27 Iso-surfaces of streaks and vortex structure along the pipe for case DC80q2; blue: low-speed streaks; green: high-speed streaks; red: λ_2. For low- and high-speed streak iso-surfaces are correspond to $\sqrt{\rho}u_z'' = \mp 0.5$ and for λ_2 a threshold value of $-20,000$ is chosen. The black lines highlight the high-speed streak surrounded by the coherent structures.

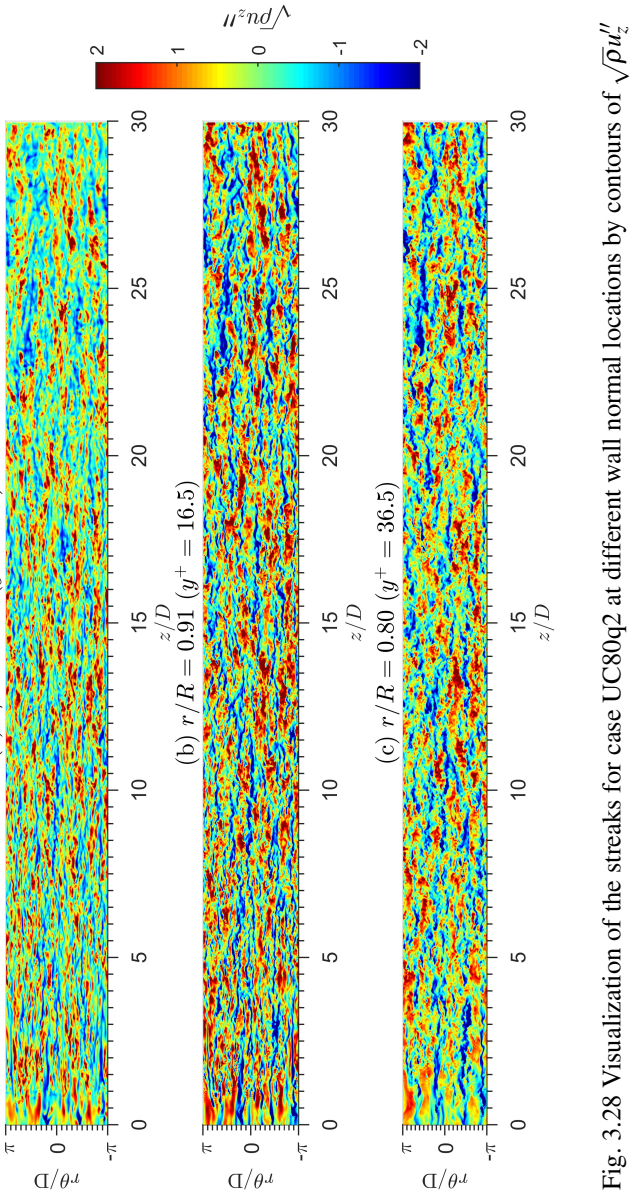

Fig. 3.28 Visualization of the streaks for case UC80q2 at different wall normal locations by contours of $\sqrt{\rho}u_z''$

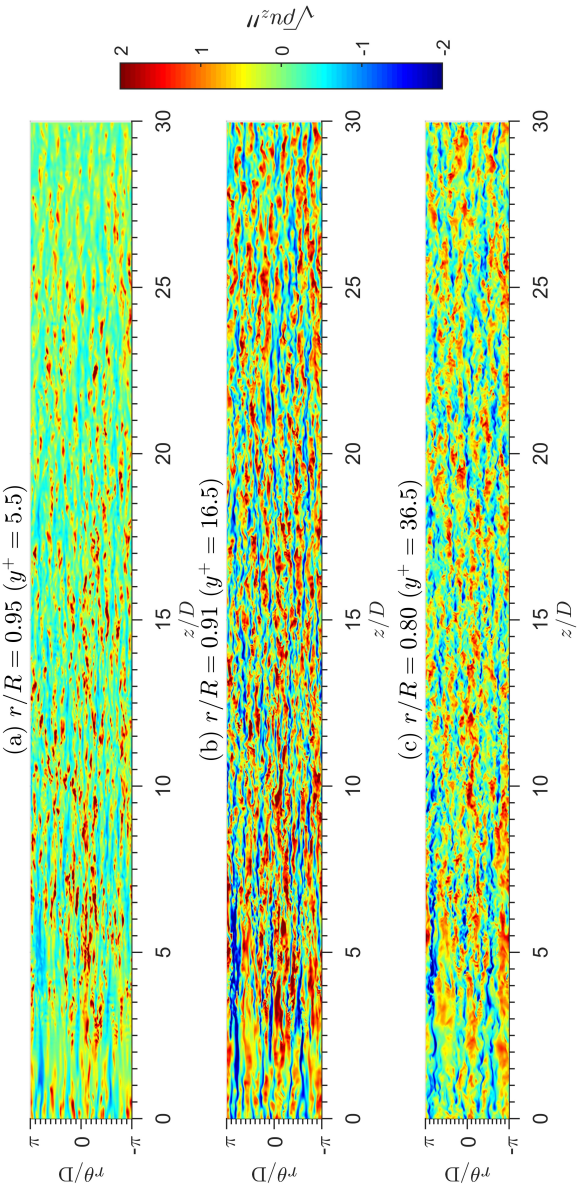

Fig. 3.29 Visualization of the streaks for case FC80q2 at different wall normal locations by contours of $\sqrt{\rho}u_z''$

Chapter 4

A framework for using high-order methods

Earlier DNS investigations of heat transfer at supercritical pressure were conducted by employing the low Mach number approximation, which is a valid assumption, especially in heat exchangers. With the advancement of computational power and improvement of numerical methods applied to CFD, several fully-compressible DNS studies have emerged out. An important remark from the fully-compressible DNS that the effects of compressibility are significant, predominantly in transcritical flow even at low Mach numbers [119]. All fully-compressible DNS studies in the literature were conducted at low Mach numbers with Peng-Robinson as the equation of state by using finite volume method. The Peng-Robinson equation is computationally less expensive but it deviates from the standard database such as REFPROP by NIST [81]. Therefore, in this study, a framework to simulate supercritical flow is presented using discontinuous-Galerkin spectral element method (DGSEM), which inherently has high-order accuracy. This framework will also be benefi-

cial for the DNS investigations aimed toward the high Mach number flow for other application.

4.1 Description of the cases

To demonstrate the capability of this CFD code (discussed in Section 2.2), three distinct cases are simulated, which correspond to different bulk Mach numbers as shown in Table 4.1. The friction Reynolds number (Re_τ) is based on half channel height. The simulated cases are for CO_2 with variation in Mach number. These cases have a bulk Reynolds number of 2800 based on half channel height, bulk velocity and viscosity at reference condition at 8 MPa pressure and 340 K temperature. The wall temperature is fixed to 335 K for the bottom wall and 345 K for the top wall. With the increase in Mach number, the wall-normal temperature profile will differ from the incompressible flow and it shows the effect of non-linear fluid property change. The simulations were performed with $128\times56\times128$ elements in streamwise, wall-normal and spanwise direction. The polynomial order was varied between 2-5, which resulted in a degree of freedom of 24-198 Millions. All three cases used the EoS derived from the CoolProp database as described in Section 2.2.4. The target error level was set to 10^{-6} and maximum refinement level was set to the 15 for all EoS tables. In the simulated region, all EoS tables achieves convergence to targeted error level. The combination of highly accurate EoS, high-order characteristics of the solver, and fully-compressible DNS warrants the high-fidelity simulation.

4.2 Mean flow parameters

The simulations were initialized with the random perturbation and after the development of fully developed turbulent flow data were gathered. Time averaging (also knows as Reynolds averaging) was done using the data for

Table 4.1 A summary of simulation conditions; reference conditions are at $p = 8$ MPa, $T = 340$ K

Case	Ma	Re	Re_τ	T_{up} (K)	T_{bottom} (K)	p_b (MPa)
CM02R28	0.2	2800	190			8.020
CM05R28	0.5	2800	190	345	335	8.189
CM07R28	0.7	2800	190			8.394

10 flow through times. Figure 4.1 illustrates the mean velocity, temperature, and density profiles for all three cases shown in Table 4.1. The mean velocity, mean density and mean pressure were normalized with the respective bulk values while the temperature is normalized by a reference temperature. The peak in mean velocity shifted upward with the increase in Mach number while there is no change in the profile close to the wall. The wall-normal mean temperature profiles vary significantly as depicted in Figure 4.1b. At the low Mach number, the profile is S-shaped which is typically observed in hot-cold channel flows (for instance in Sengupta et al. [119]). With the increase in Mach number, the temperature profiles changes. The maximum value in temperature occurs near to the hot wall, but not exactly at the hot-wall.

The effects of Mach number can also be seen on mean density profiles in Figure 4.1c. In these DNS, same Reynolds number and the same bulk density (corresponding to the reference conditions of 8 MPa and 340 K) is maintained for the isothermal wall. With increasing Mach number, the pressure increases to enforce the constant bulk density calculated at the reference condition. Therefore, the values of density differ at $y = -H$ and $y = H$ (i.e. at the no-slip walls). This procedure differs from that of Kim et al. [70] in which the authors have kept the same bulk pressure while varied the bulk density for different cases. Figure 4.1d illustrates the variation of mean pressure along the y/H. The mean pressure is symmetric, unlike the other variables. As expected, pressure fluctuations increase with increasing Mach numbers. But, the fluctuations in mean pressure are insignificant quantitatively and it also

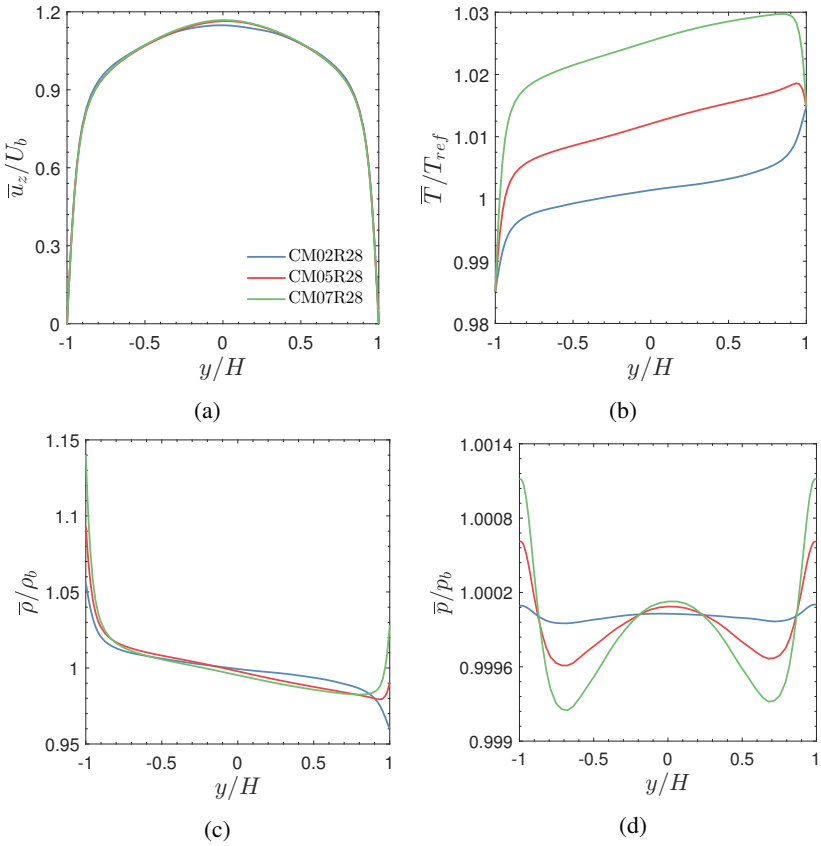

Fig. 4.1 Normalized Reynolds averaged quantities as a function of the vertical coordinate. (a): Mean velocity profile, (b): mean temperature profile, (c): mean density profile, and (d): mean pressure profile

supports the applicability of the low Mach assumption in earlier investigations employed earlier for the cooling characterization in a spatially developing pipe flow.

4.3 Instantaneous flow

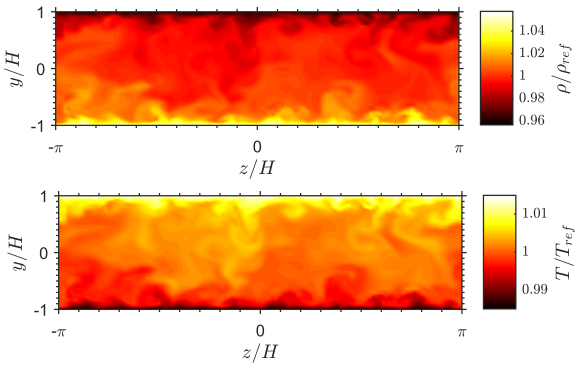

Fig. 4.2 Instantaneous contours; top: density and, bottom: temperature for case Ma02Re28

In this section, instantaneous flow fields are visualized in the $y-z$ plane for two extreme cases. Figure 4.2 demonstrates the contours of the instantaneous field. At the low Mach number, density varies by almost ± 5 % from the reference value while the temperature variations are within ± 1.5 %. A sharp change in both variables is observed in the near-wall region while the core region has almost the same magnitude. As soon as Mach number increases, this trend changes as can be observed in Figure 4.3 for case Ma07Re28. The fluctuations around the reference value also increase as compared to the low Mach number case. The change in temperature in the near-wall region is more pronounced. This leads, of course, to change in the density.

To further analyze the turbulence in the near-wall region, the instantaneous fluctuations of velocity for the high Mach number case (i.e. case Ma07Re28) are examined. Figure 4.4 shows the velocity streaks in $x-z$ plane in the near-wall region (corresponding to $y^+ = 25$, based on the reference values). It is worth to mention here that semi-local scaling is not employed here because the variation in properties is not drastic in this range. Low and high speed

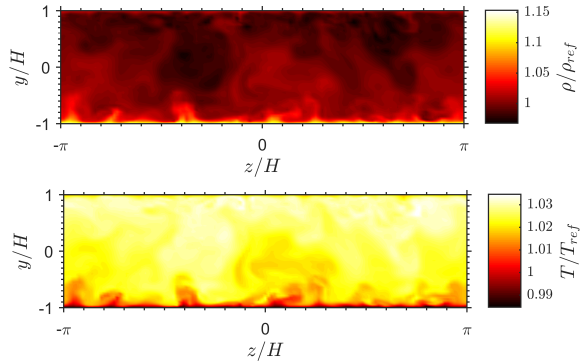

Fig. 4.3 Instantaneous contours; top: density, and bottom: temperature for case Ma07Re28

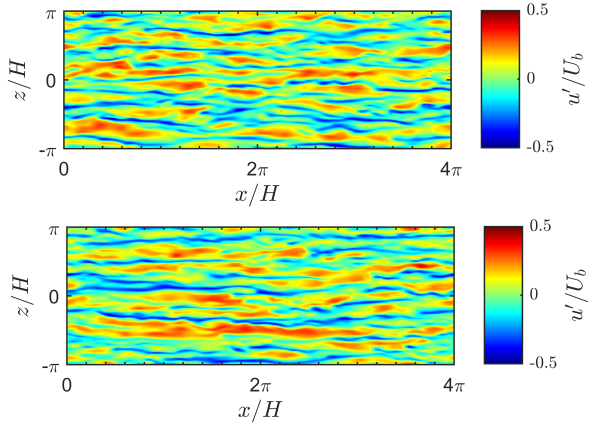

Fig. 4.4 Instantaneous contours of the streamwise velocity fluctuations at $y^+ = 25$; top: hot wall, and bottom: cold wall for case Ma07Re28

streaks are present near both walls. Both the streaks are comparatively longer near to the cold wall while streaks are shorter and thicker in near the hot wall.

4.4 Turbulence statistics

The wall normal variation of turbulent shear stress ($\widetilde{\overline{\rho}u''v''}$) is depicted in Figure 4.5a for all three cases considered. It represents the strength of turbulence in a flow. As expected, the increase in Mach number increases the turbulent shear stress in the flow. In addition, the hot and cold wall also affect the turbulent shear stress as can be seen by the asymmetric profiles. The profile of turbulent kinetic energy $\left(\frac{1}{2}\widetilde{\overline{\rho}u_i''u_i''}\right)$ is also shown in Figure 4.5b. The peak in the turbulent kinetic energy at close to the wall increases with the increase in the Mach number due to the increase in fluctuations.

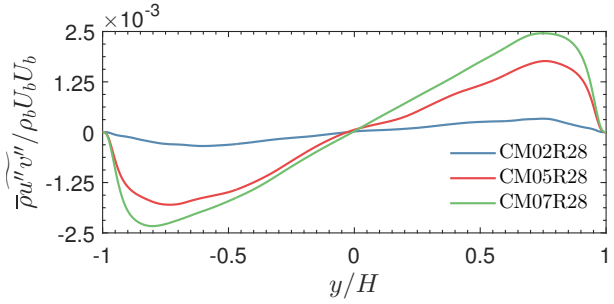

(a)

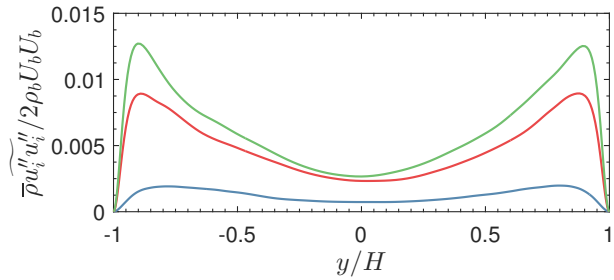

(b)

Fig. 4.5 Wall normal profile for (a): turbulent shear stress, and (b): turbulent kinetic energy

In this chapter, results from channel flow simulation are presented, which were conducted at different Mach number in the supercritical range. This successful implementation opens the avenue for further research and provides an opportunity to exploit the high-order accuracy for conducting under-resolved DNS (also know as implicit large eddy simulation). Gassner and Beck [48] highlighted that the superior discretization properties of high-order approximations (such as DG method used here) are retained even for under-resolved simulations, which is not true for the low-order approximation because of the unacceptable numerical discretization errors.

Chapter 5

Computationally light heat transfer and hydraulic model

Heat transfer deterioration not only reduces the thermal efficiency but also presents a threat to the safety of the power plant. Prior identification of deteriorated heat transfer will help the engineers to mitigate it. DNS proved to be a reliable and accurate numerical tool, however, the main downside of the DNS is the heavy computational burden. It is noted that DNS is limited to the cases with relatively low Reynolds number, due to the spatial and temporal resolution requirement. This situation can be slightly improved with the development of high-performance computing and highly parallel scalable code. Nevertheless, a less-computational intensive model is a foremost requirement. The DNS has the ability to provide useful information regarding the flow physics. In addition, DNS data also serve as a reliable source for different statistics such as the radial profile of several parameters, which can be readily used for benchmarking of newly developed turbulence models. In the past,

DNS data for heating were used for turbulence model benchmarking by He et al. [56], Pucciarelli and Ambrosini [109] and Bae et al. [11, 12]. Pandey et al. [100, 101] derived a semi-analytical model and made an attempt to empirically fit with the three DNS cases of heating, which has provided a good agreement with the experimental data (refer to Appendix B for details). To support the modeling, a comprehensive DNS database is delivered in this chapter for the heating of supercritical CO_2. Earlier in Section 1.2.2, incapability of correlations and RANS simulation were highlighted. Therefore, a different and relatively new data-driven approach is adopted instead of conventional turbulence modeling. This section is divided into two parts, the first section discusses the DNS database along with a brief explanation and the second section describes the DNN model followed by obtained results.

5.1 DNS database

To demonstrate the capability of machine learning based algorithms, a DNS database for heating of supercritical carbon dioxide has been prepared by performing DNS of pipe flow using OpenFOAM [29]. The integral domain and boundary conditions in the implemented DNS are identical to Section 2.1.1, except a positive heat flux on a pipe length of $60D$. Considering the massive computational resource requirement to construct the database, the grid resolution is reduced from the earlier work, yet still comparable to the classical DNS work from Bae et al. [9]. It is noted that a grid independence study shows that the resolution has a negligible effect on the mean statistics considered here. That is, the low-resolution DNS makes no difference from high-resolution DNS on the development of wall temperature T_w and wall shear stress τ_w as shown in Figure 5.1.

The coarse grid resolution opted for this database, is equivalent to approximately $70 \times 120 \times 260$ (radial r, circumferential θ near the wall and axial z direction) for the inflow domain and $70 \times 120 \times 1500$ for the heated domain, when converted from the Cartesian to the cylindrical coordinates.

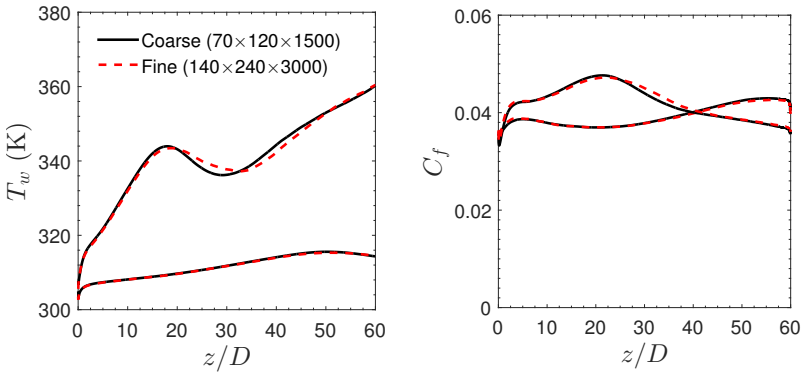

(a) (b)

Fig. 5.1 Mesh sensitivity study for case 1 and 3 from Table 5.1. (a): Wall temperature and (b): Skin friction coefficient

The grid is uniformly spaced in the axial direction, and refined near the wall in the radial direction with a stretching ratio of about 18. The dimensionless resolution in wall units, i.e., $y^+ = yu_\tau/\nu$, where $u_\tau = \sqrt{|\tau_w|/\rho}$ at the inlet reads as $0.17\,(\text{wall}) < \Delta y^+ < 3\,(\text{center})$, $(R\Delta\theta)^+ \approx 9$, $\Delta z^+ = 14$ based on the inlet Reynolds number $\text{Re}_0 = 5400$. The dimensionless time step $\Delta t^+ = \Delta t/t^+ = 4 \times 10^{-4}$, where $t^+ = D/u_\tau$. The flow bulk temperature T_b rises in the downstream direction with the input of wall heat flux. Accordingly, the bulk Reynolds number $\text{Re}_\text{b} = 4G/(\mu_b \pi D)$ based on the bulk fluid properties will increase. However, no significant difference can be found in T_w and τ_w along the pipe.

The database generated with DNS includes 36 cases in total [1]. Only upward flow is considered for this database because it suffers from the heat transfer deterioration. One case takes approximately 12,000 core-hours on *Hazel Hen* supercomputer. It means that a total of about 500,000 core-hours

[1]This DNS database can be accessed by visiting: https://www.ike.uni-stuttgart.de/forschung/sco2/dns/

Table 5.1 Parameters for DNS for the database. In each cell, the upper number indicates the case index. The lower bracket represents (D, q_w, T_0, p_0). The pipe diameter D is in mm, the wall heat flux q_w is in kW/m^2, the inlet temperature T_0 is in K and the inlet pressure p_0 is in MPa.

1 (2,10,301.15,8)	2 (2,20,301.15,8)	3 (2,30,301.15,8)
4 (2,10,288.15,8)	5 (2,20,288.15,8)	6 (2,30,288.15,8)
7 (2,10,301.15,8.8)	8 (2,20,301.15,8.8)	9 (2,30,301.15,8.8)
10 (2,10,288.15,8.8)	11 (2,20,288.15,8.8)	12 (2,30,288.15,8.8)
13 (5,5,301.15,8)	14 (5,10,301.15,8)	15 (5,20,301.15,8)
16 (5,5,288.15,8)	17 (5,10,288.15,8)	18 (5,20,288.15,8)
19 (5,5,301.15,8.8)	20 (5,10,301.15,8.8)	21 (5,20,301.15,8.8)
22 (5,5,288.15,8.8)	23 (5,10,288.15,8.8)	24 (5,20,288.15,8.8)
25 (10,5,301.15,8)	26 (10,10,301.15,8)	27 (10,20,301.15,8)
28 (10,5,288.15,8)	29 (10,10,288.15,8)	30 (10,20,288.15,8)
31 (10,5,301.15,8.8)	32 (10,10,301.15,8.8)	33 (10,20,301.15,8.8)
34 (10,5,288.15,8.8)	35 (10,10,288.15,8.8)	36 (10,20,288.15,8.8)

is necessary to complete all the cases in the database. Each case represents one particular set of condition. A complete description of the experimental conditions used in the simulation is shown in Table 5.1. The database covers 3 values of pipe diameter ($D = 2, 5, 10$ mm), 4 values of the wall heat flux ($q_w = 5, 10, 20, 30$ kW/m^2), 2 values of inlet temperature ($T_0 = 288.15, 301.15$ K) and 2 values of inlet pressure ($p_0 = 8, 8.8$ MPa). The number of values is constrained due to the limited computational resources. The mass flux G $\left(\text{kg}/(\text{m}^2\cdot\text{s})\right)$ is adjusted accordingly to keep the inlet Reynolds number fixed at $\text{Re}_0 = 5400$. The inlet pressures p_0 are set higher than the critical

pressure $p_c = 7.38$ MPa. Both the inlet temperatures T_0 are set lower than the pseudo-critical temperature to demonstrate the potential peculiar heat transfer deterioration. Unlike the rest input parameters to the DNN, there is a large number of values available for the bulk specific enthalpy h_b due to a large number of discretization points in the pipe streamwise direction. Among them, 60 samples of h_b values were taken in each case, with one from every diameter length interval. Therefore, in total there are $35 \times 60 = 2100$ data points.

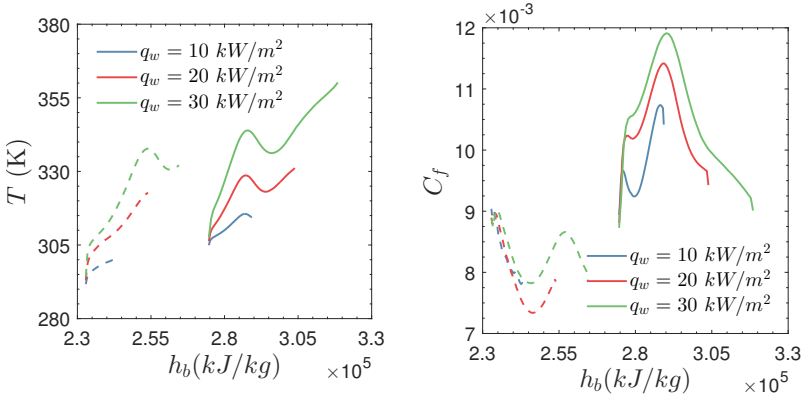

Fig. 5.2 Variation of (a): wall temperature and (b): skin friction coefficient, for cases 1-6. Dashed lines: T_0=288 K, solid lines: T_0=301 K

Figure 5.2 -5.7 depict the variation of wall temperature and skin-friction coefficient for all 36 cases. Due to the heat addition, the mean wall temperature rises along the length of the pipe. In high heat flux cases, a peak in the wall temperature can be seen, denotes deteriorated heat transfer (e.g. green curve in Figure 5.2a). This peak in wall temperature increases with an increase in wall heat flux, indicating the intense heat transfer deterioration. With the increase in the wall heat flux, the variations of properties increases and it negatively affect the heat transfer to sCO_2. This is attributed to the buoyancy

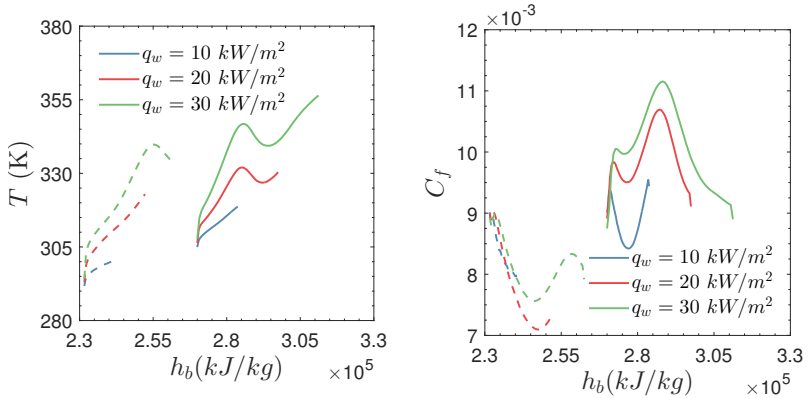

Fig. 5.3 Variation of (a): wall temperature and (b): skin friction coefficient, for cases 7-12. Dashed lines: T_0=288 K, solid lines: T_0=301 K

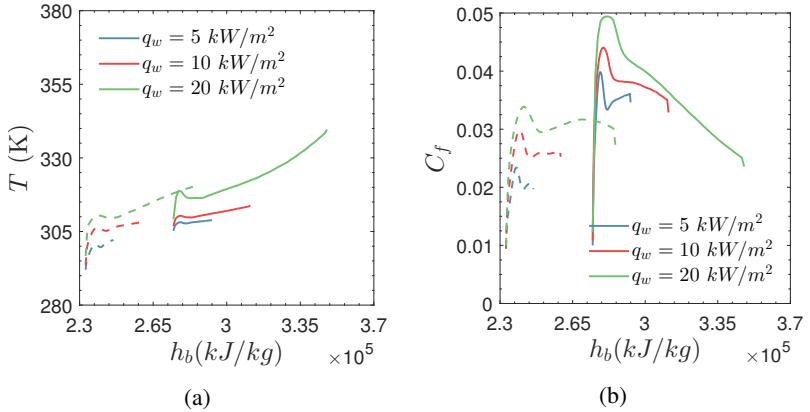

Fig. 5.4 Variation of (a): wall temperature and (b): skin friction coefficient, for cases 13-18. Dashed lines: T_0=288 K, solid lines: T_0=301 K

and acceleration [9, 94]. Also, one can compare from Figure 5.2a that heat transfer deterioration is delayed with a decrease in the inlet temperature, which

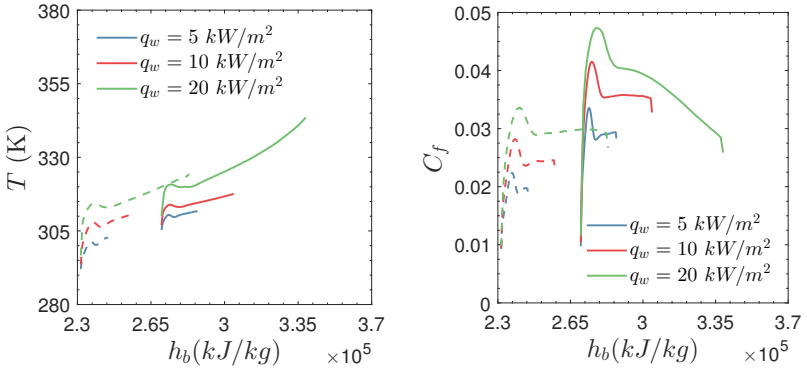

(a) (b)

Fig. 5.5 Variation of (a): wall temperature and (b): skin friction coefficient, for cases 19-24. Dashed lines: T_0=288 K, solid lines: T_0=301 K

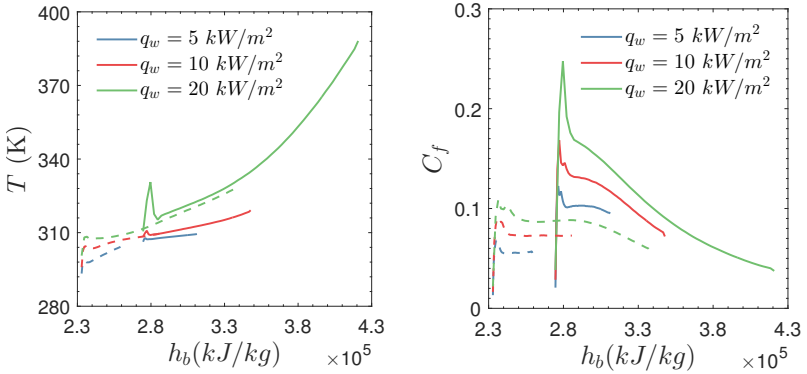

(a) (b)

Fig. 5.6 Variation of (a): wall temperature and (b): skin friction coefficient, for cases 25-30. Dashed lines: T_0=288 K, solid lines: T_0=301 K

is obvious due to the fact that it is far away from the pseudo-critical point. In most of the cases, heat transfer recovery can be seen after the deterioration.

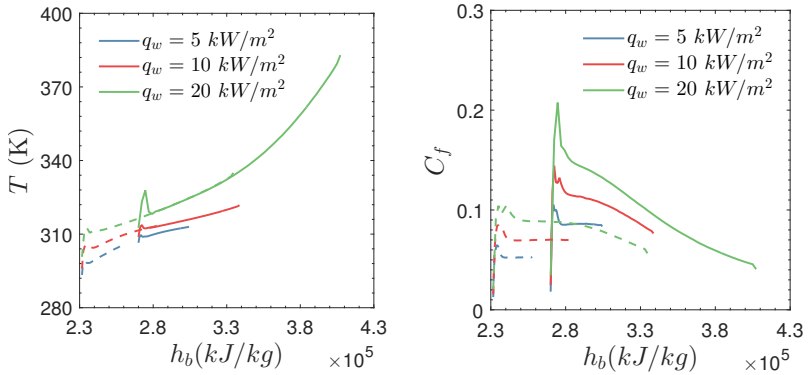

(a) (b)

Fig. 5.7 Variation of (a): wall temperature and (b): skin friction coefficient, for cases 31-36. Dashed lines: T_0=288 K, solid lines: T_0=301 K

This recovery is brought by the inward and wall-normal motions instead of sweep and ejection events of turbulent shear stress generation.

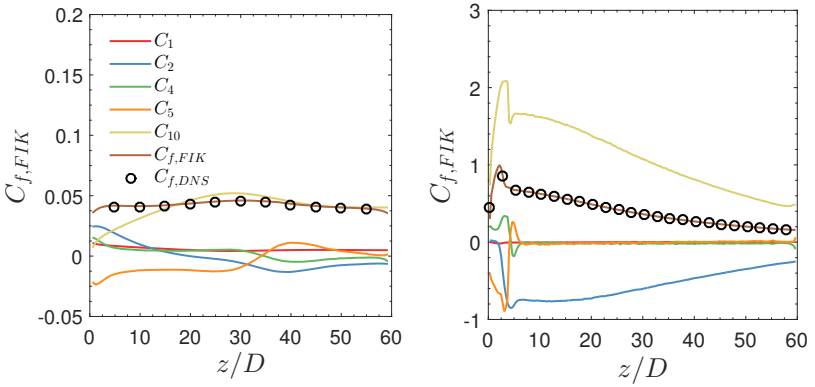

(a) (b)

Fig. 5.8 Decomposition of skin friction coefficient for case (a): case 2 (2,20,301.15,8) and (b): case 27 (10,20,301.15,8)

With the increase in the pipe diameter, skin friction rises drastically (see Figure 5.2b and 5.4b).The local peak of it reduces by a factor of 2.5 when the inlet temperature is much lower than the pseudocritical temperature. With the increase in pipe diameter and wall heat flux, friction loss increases due to an increase of the buoyancy effects and it contributes positively to skin friction. To quantify the effects of pipe diameter, FIK identity as given in Equation 3.1, is applied to two cases. Figure 5.8 illustrates the decomposed skin friction coefficient for two cases with the same boundary conditions except for the diameter. The variation of C_1, C_2, C_4, C_5, and C_{10} can be seen; the remaining parts which are not shown here have negligible magnitude. Figure 5.8a corresponds to the D=2 mm and Figure 5.8b corresponds to D=10 mm. One can observe from both figures that C_{10} which is the buoyancy part has the highest contribution to the skin friction factor. With a larger diameter, the effects of buoyancy are more severe. The peak in the skin friction in Figure 5.8b is solely due to the buoyancy effects.

5.2 Machine learning based model

In this work, a novel approach to link DNS to DNN in modeling the heat transfer and hydraulic characteristics of supercritical fluids is proposed. This work aimed to show that a combination of DNS and DNN can maintain the modeling accuracy that DNS alone has, and significantly reduce the computational load.

5.2.1 Deep neural network

A general DNN consists of one input layer, more than one hidden layers, and one output layer. Each layer has a number of neurons. A fully-connected DNN with two hidden layers is shown in Figure 5.9 as an example. In this work, for a given pipe diameter, inlet pressure, heat flux, inlet temperature, and bulk specific enthalpy (five input parameters), the wall temperature and wall shear

stress (two output parameters) are expected to be known. Therefore, there are five neurons in the input layer, corresponding to the five input parameters. There are two neurons in the output layer, corresponding to the two output parameters.

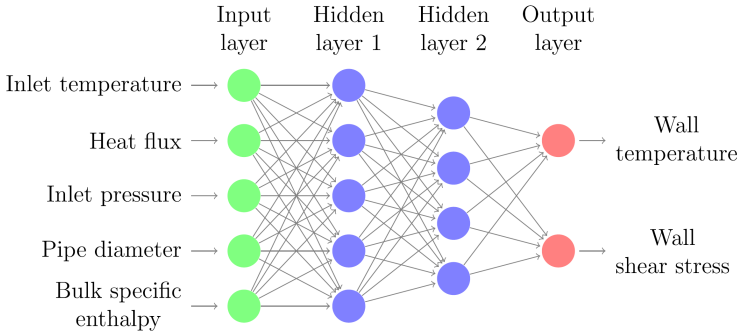

Fig. 5.9 A representative deep neural network

Every neuron has a weight vector $\mathbf{w} = (w_1, w_2, \ldots, w_m)$, if the input is $\mathbf{r} = (r_1, r_2, \ldots, r_m)$, where m is the number of inputs to the neuron. For example, the neuron in the first hidden layer in Figure 5.9 has $m = 5$. The neuron operation has two steps. First,

$$z = \mathbf{w} \cdot \mathbf{r} + b, \tag{5.1}$$

where b is the bias of the neuron and $\cdot$ represents the dot product of two vectors. Different neurons may have different weight vectors and biases. In the second step, a non-linearity is introduced,

$$\sigma = \frac{1}{1 + e^{-z}}, \tag{5.2}$$

where σ is the output of the neuron. Clearly, the range of Equation (5.2) is $[0, 1]$. This enables the DNN to capture the non-linear features in the data.

In this work, each data point used for training has an input vector (five parameters) and an output vector (two parameters). The quadratic cost function of the DNN is,

$$C(\mathbf{W},\mathbf{b}) = \frac{1}{2n}\sum_{\mathbf{x}} ||\mathbf{y}(\mathbf{x}) - \mathbf{a}(\mathbf{x},\mathbf{W},\mathbf{b})||^2, \tag{5.3}$$

where $\mathbf{W}$ and $\mathbf{b}$ represent the weight vectors and biases of all the neurons in the DNN, respectively. The input vector and the output vector of a training data point are denoted by $\mathbf{x}$ and $\mathbf{y}(\mathbf{x})$, respectively. The predicted output given by the DNN is $\mathbf{a}(\mathbf{x},\mathbf{W},\mathbf{b})$. The number of data points for training is n. This cost function in Equation (5.3) computes the mean squared error (MSE) of the DNN for all the training data. The goal in the DNN training is to find the weight vectors ($\mathbf{W}$) and biases ($\mathbf{b}$) that minimize the cost function.

In this work, the output vector $\mathbf{y}$ has two elements y_1 and y_2 with two different physical meanings (i.e. wall temperature and the wall shear stress). Therefore, normalization needs to be performed on one element. Without loss of generalization, it is assumed that y_2 is normalized to be y_2' as follows:

$$y_2' = (y_2 - y_2^{\min}) \times \frac{y_1^{\max} - y_1^{\min}}{y_2^{\max} - y_2^{\min}} + y_1^{\min} \tag{5.4}$$

It can be seen that when y_2 takes the minimum value $y_2^{\min}$, $y_2' = y_1^{\min}$. When y_2 takes the maximum value $y_2^{\max}$, $y_2' = y_1^{\max}$ The output vector is then,

$$\mathbf{y} = [y_1 \;\; y_2']. \tag{5.5}$$

Clearly, the range of y_2 is mapped to the range of y_1, so that they are equally valued in the cost function.

For the ease of understanding, $\mathbf{v} = (v_1, v_2, \ldots, v_l)$ is employed to denote all the variables of the cost function C in Equation (5.3), including all the weights and biases of the DNN. The $\mathbf{v}$ can be iteratively updated towards the minimum value of C. The change ΔC in C produced by a small change

$\Delta \mathbf{v} = (\Delta v_1, \Delta v_2, \ldots, \Delta v_l)^T$ is,

$$\Delta C \approx \nabla C \cdot \Delta \mathbf{v}, \tag{5.6}$$

where the gradient ∇C of the cost function is,

$$\nabla C = (\frac{\partial C}{\partial v_1}, \frac{\partial C}{\partial v_2}, \ldots, \frac{\partial C}{\partial v_l}) \tag{5.7}$$

Let assume that,

$$\Delta \mathbf{v} = -\eta \nabla C, \tag{5.8}$$

where η is a small rate to ensure that $\Delta \mathbf{v}$ is small. Then, accounting for Equation (5.6),

$$\Delta C \approx -\eta ||\nabla C||^2 \leq 0, \tag{5.9}$$

which ensures that the cost function C iteratively decreases (non-increasing, to be exact). The update on $\mathbf{v}$ is then,

$$\mathbf{v}' = \mathbf{v} - \eta \nabla C \tag{5.10}$$

Then, for any weight w_i or bias b_j in $\mathbf{v}$,

$$\begin{aligned} w_i' &= w_i - \eta \frac{\partial C}{\partial w_i}, \\ b_j' &= b_j - \eta \frac{\partial C}{\partial b_j} \end{aligned} \tag{5.11}$$

The gradient ∇C of the cost function is computed with the standard backpropagation algorithm [25]. It should be noted that the gradient descent method reaches the local minimum of the cost function. The cost function C in Equation (5.3) is a sum of components from all the data points. The gradient computation can be very time-consuming when the number of training data points n is large. Therefore, in this work, the stochastic gradient descent is utilized. That is, at each iteration, a small number of data points are used to

approximate the gradient. For instance, if n is 1000, at the first iteration, 10 data points are randomly chosen for the gradient computation. Then, at the second iteration, 10 data points again selected randomly from the remaining 990 data points. This process is continued until all the 1000 data points have been used, which completes one epoch. In the second epoch, the same process as of first epoch is repeated. The training is terminated when either the cost function does not further decrease or the number of epochs reaches the set limit.

Overfitting, which means that the DNN fits a portion of the data comparatively too closely, should be prevented. If only the idiosyncrasies of the data used in the training process are captured, and the global features (the general heat transfer and hydraulic characteristics of sCO_2 in this work) are lost, overfitting occurs and the trained DNN is practically not very useful. Bayesian regularization [88] is implemented to counter overfitting. A term on the weight vectors is added to the cost function so that the weights are also minimized. Smaller weights tend to improve the generalization quality of the DNN.

5.2.2 Modeling results

The proposed DNN has two hidden layers. There are 50 neurons in each of the hidden layers. In general, a DNN with a larger number of hidden layers, on one hand, has the potential to achieve better performance. On the other hand, it has a more complicated structure and is thus more difficult to train. Among 36 cases, 35 cases (except case 8) were selected for the training and blind testing. It results in the 2100 data points, and 80% (i.e., 1680 data points) are randomly selected and used for training. For each data point, the error percentage is defined as,

$$\text{error percentage} = \frac{|a_k(\mathbf{x}) - y_k(\mathbf{x})|}{y_k(\mathbf{x})}, \tag{5.12}$$

where a_k represents the kth output generated by the DNN and y_k represents the kth output of the data point.

For the first output wall temperature, the mean error percentage for the training data points is 0.08%, and the error percentage standard deviation is 0.17%. For the second output wall shear stress, the mean error percentage for the training data points is 1.23%, and the error percentage standard deviation is 4.20%. The performance of the DNN for the training data points, i.e., how closely the output generated by the DNN matches the output of the data, is shown in Figure 5.10. Training of this DNN takes 249 epochs and 1239 s on a regular computer with an Intel® i7 processor running at 2.6 GHz and 8 GB RAM.

The rest 20% of the 2100 data points (i.e. 420 data points) are used for validation and strictly separated from the training data points. That is, the validation data points are hidden in the training process, and only visible to the DNN after the training is completed. Strictly separating the validation data from the training data enables objective and fair evaluation of the performance of the DNN.

For the first output wall temperature, the mean error percentage for the validation data points is 0.07%, and the error percentage standard deviation is 0.13%. For the second output wall shear stress, the mean error percentage for the validation data points is 1.02%, and the error percentage standard deviation is 1.98%. The performance of the DNN for the validation data points, i.e., how closely the output generated by the DNN matches the output of the data, is shown in Figure 5.11. According to the statistics reported in Table 5.2 and Table 5.3, the performance of the DNN on the validation data is even better than that on the training data. Evidently, the DNN is successful in counter-overfitting and has achieved general applicability under the experimental conditions covered by the database. Evaluating the wall temperature and the wall shear stress with a given experimental condition and bulk specific enthalpy takes 5.4 ms on average on a regular computer with an Intel® i7 processor running at 2.6 GHz and 8 GB RAM.

Table 5.2 Performance of the DNN for the wall temperature on the training and validation data

	Mean error percentage	Error percentage standard deviation
Training	0.08%	0.17%
Validation	0.07%	0.13%

Table 5.3 Performance of the DNN for the wall shear stress on the training and validation data

	Mean error percentage	Error percentage standard deviation
Training	1.23%	4.20%
Validation	1.02%	1.98%

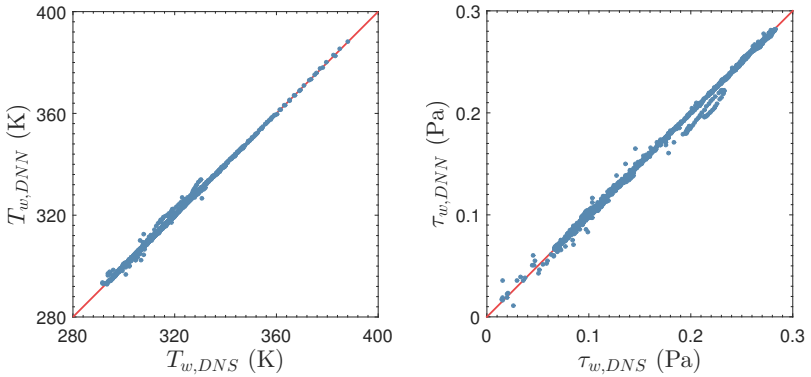

Fig. 5.10 Performance of the DNN on the training data. (a): wall temperature and (b): wall shear stress. Note: straight line indicates perfect matching.

Furthermore, the trained DNN is tested on an experimental condition out of the database (i.e. the case 8). The pipe diameter D is 2 mm. The wall heat flux q_w is 20 kW/m^2. The inlet temperature T_0 is 301.15 K. The inlet pressure p_0 is 8.8 MPa. Both the wall temperature T_w and the wall shear stress τ_w are evaluated with the DNN and then compared with the results from DNS.

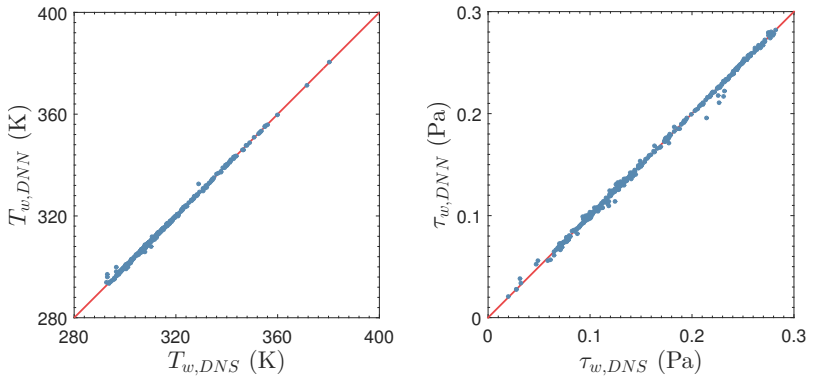

(a) (b)

Fig. 5.11 Performance of the DNN on the validation data. (a): wall temperature and (b): wall shear stress. Note: straight line indicates perfect matching.

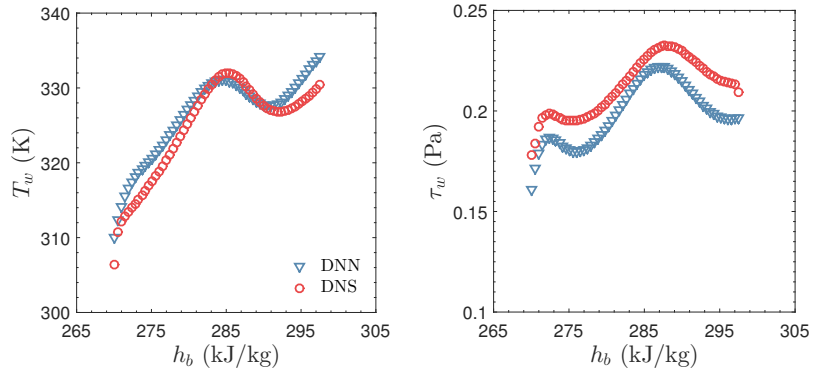

(a) (b)

Fig. 5.12 Test performance of the DNN on case 8 which was not used in training and validation. (a): wall temperature and (b): wall shear stress.

As presented in Figure 5.13, DNN still closely follows DNS. The training, validation, and testing results reported in this section show that DNN is a

computationally light approach for heat transfer and hydraulic characteristics modeling of supercritical fluids. A combination of DNS and DNN is able to maintain the modeling accuracy that DNS alone has, and significantly reduce the computational load.

5.2.3 Comparison of different machine learning algorithms

Earlier, a model was presented for machine learning by using DNN only, which has shown a superior prediction capability. However, in the field of supervised learning, there are several machine learning algorithms are available viz. decision tree (DT), gradient boosting (GB), random forest (RF) along with deep neural network (DNN) [73].

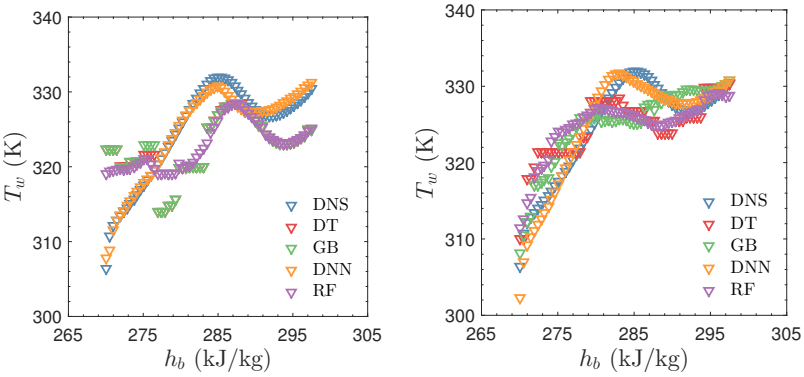

Fig. 5.13 Test performance of the different machine learning algorithm for wall temperature on case 8. (a): With 5 features (b): With 10 features.

A comparison between different algorithms was made by employing TensorFlow [1] within the Python programming language. For the sake of simplicity, only the wall temperature was chosen as a label (output) and two different configurations for features (input) were used. In the first configuration, five features were used (inlet temperature, heat flux, inlet pressure,

pipe diameter, and bulk fluid enthalpy). In the second configuration, ten features (inlet temperature, heat flux, inlet pressure, pipe diameter, bulk fluid enthalpy, bulk temperature, Reynolds number, bulk velocity, mass flux and distance from the inlet) were employed to observe the effect of features on the performance of machine learning. Similar to Section 5.2.1, 35 cases were selected (except case 8) for training and testing, and case 8 was completely hidden from the process. Figure 5.13 shows the performance of selected 4 machine learning algorithms on case 8 with two configurations. The DNN outperform every other method in terms of higher prediction capability. With the increase in features, the performance of each method improves slightly. With more features, other algorithms can also be an alternative, which requires much lesser time to train compared to the DNN.

Chapter 6

Conclusions and future directions

6.1 Conclusions

Supercritical fluids have shown a great potential in terms of higher thermal efficiency in power plants. The power cycle using supercritical carbon dioxide (sCO_2) are already under development. Nevertheless, the technology suffers from a few disadvantages as well. Among them, heat transfer deterioration and its prediction are chief concerns at the moment. Experiments, correlations, analytical model and computational fluid dynamics analysis are the most studied methods in the literature for supercritical fluids. Direct numerical simulation (DNS) proved to be a high-fidelity approach for examining the physics behind the peculiar heat transfer at supercritical pressure. With the advancement of computational power, several DNS investigation has been emerged out in the literature for turbulent pipe flow, all of them focused towards the heating characterization of sCO_2. Therefore, DNS of developing pipe flows has been performed to investigate the buoyancy induced turbulence

modulation in the pipe flow at supercritical pressure under cooling conditions. The inlet pressure was close to the critical pressure, and inlet temperature was applied in a way to capture the strong variation of the properties. The basic attributes show that turbulence is impaired in the downward flow and it results in poor heat transfer and vice versa for the upward flow. The flow without buoyancy, i.e., forced convection, lies in between the spectra with extremes as upward and downward flow cases. Further analysis was conducted using the FIK identity which decomposes the skin friction factor and Nusselt number, and it reveals that the turbulent contribution decreases in the downward flow. It was also found out that the buoyancy has a crucial impact on the skin friction coefficient and it results in negative shear stress at the certain section in upward flow. The cumulative contribution of laminar contribution shows that approximately 90% of the laminar drag is generated within 30 wall-units in all cases. The Nusselt number budget indicated that declination in the turbulent contribution seeds the impaired heat transfer characteristics in the downward flow. The downward flow case has a low heat transfer rate and high drag at the same time. The low- and high-speed streaks were visualized and we observed that low-speed streaks disappeared and high-speed streaks elongated in the deteriorated heat transfer region. While during the recovery low-speed structures reappear and start growing in the circumferential direction. The high-speed streaks were surrounded by coherent structures. Quadrant analysis provided details regarding the fractional contribution of Reynolds shear stress. It has shown that ejection and sweep events are responsible for the majority of turbulence generation in any normal turbulence flow. The reduction in sweep (Q_4) and ejection (Q_2) events resulted in turbulence attenuation in the downward flow. At the onset of turbulence recovery, the inward (Q_3) and outward (Q_1) interactions grow rapidly contrary to the usual trend. Both ejection and sweep events became stronger in the streamwise direction in the upward flow and each event elongated in the $\sqrt{\rho}u_r''$-axis and it implied more lift to both high and low-speed streaks. In the downward flow, streamwise turbulent heat flux suffers from attenuated turbulence and

the amplitude of it is suppressed during the deterioration regime but as soon as flow recovers, second and fourth quadrant appear instead of first and third quadrants. This analysis also conveys that the streamwise turbulent heat flux is affected significantly as compared to the radial turbulent heat flux and quadrant transition appears in streamwise turbulent heat flux only in downward flow during the recovery. The anisotropy is quantified by using the invariants of the Reynolds stress tensor. The upward flow attempt to acquire a disk-like turbulence structure in the near-wall region in which two principal stresses have significant magnitude, much larger than the third. In contrast, turbulence became rod-like in the deteriorated region in which one principal stress has an incomparable magnitude than the other two. This study affirms the past findings and provided new knowledge regarding the flow.

In addition to DNS of low Mach number turbulent pipe flow, a new framework for direct numerical simulations using a fully-compressible high-order computational code based on the discontinuous Galerkin spectral element method is also presented. The high-performance capability combined with the high-order accuracy is illustrated by DNS of turbulent channel flow of sCO_2. The bulk Reynolds number was set to 2800 based on the channel half-width and Mach number was varied in the range of 0.2 to 0.7 with a temperature difference of 10 K. The degree of freedom was in between 58-200 Millions. to resolve the small-scale turbulence motions. For the equation of state, a computationally robust and highly accurate approach has been used based on the quadtree tabulation method. Three distinct cases were examined with supercritical channel flow while varying the Mach number. The mean velocity profile is not affected much by the Mach number variations. On the other hand, mean density and mean temperature profiles change significantly along the wall-normal direction. The fluctuations of density and temperature also increase around the mean with the increase in the Mach number. The low and high-speed streaks are comparatively longer near to the cold wall.

In the end, a computationally light alternative, DNN, is proposed, and it builds the link from DNS to DNN. The validation and test results show that

the performance of the DNN is significantly better than the well-established correlations, which are conventionally used for the heat transfer prediction. The prediction with the DNN takes negligible time. The database generated with DNS can be used not only with DNN, but also other methods like Reynolds-averaged Navier-Stokes (RANS).

6.2 Recommendation for future work

This work aimed towards the characterization of the cooling process of supercritical CO2, extension of a framework for the high-fidelity methods and development of simpler prediction method. The present work opens up avenues for future work and they can be categorized as follows:

- The DNS investigations were limited to the fluid domain in present work. It will be interesting to see the effect of the solid domain by conducting conjugate heat transfer analysis.
- A framework is delivered by this work for fully compressible, high fidelity DNS. Further simulations should seek the answer to the effect of moderately high Reynolds number and Mach number. How will the compressibility affect the turbulence and thereby the heat transfer.
- The low-computer intensive model have shown exemplary results. However, they were limited to low Reynolds number. Future work should combine the database from DNS and experiments.

References

[1] Abadi, M., Agarwal, A., Barham, P., Brevdo, E., Chen, Z., Citro, C., Corrado, G. S., Davis, A., Dean, J., Devin, M., Ghemawat, S., Goodfellow, I., Harp, A., Irving, G., Isard, M., Jia, Y., Jozefowicz, R., Kaiser, L., Kudlur, M., Levenberg, J., Mané, D., Monga, R., Moore, S., Murray, D., Olah, C., Schuster, M., Shlens, J., Steiner, B., Sutskever, I., Talwar, K., Tucker, P., Vanhoucke, V., Vasudevan, V., Viégas, F., Vinyals, O., Warden, P., Wattenberg, M., Wicke, M., Yu, Y., and Zheng, X. (2015). TensorFlow: Large-scale machine learning on heterogeneous systems.

[2] Ackerman, J. (1970). Pseudoboiling heat transfer to supercritical pressure water in smooth and ribbed tubes. *Journal of Heat transfer*, 92(3):490–497.

[3] Ahn, Y., Bae, S. J., Kim, M., Cho, S. K., Baik, S., Lee, J. I., and Cha, J. E. (2015). Review of supercritical CO2 power cycle technology and current status of research and development. *Nuclear Engineering and Technology*, 47(6):647 – 661.

[4] Anderson, J. D. (2005). Ludwig Prandtl′s boundary layer. *Physics Today*, 58(12):42–48.

[5] Anonymous (2017a). International Energy Outlook 2017. Technical report, U.S. Energy Information Administration.

[6] Anonymous (2017b). World Energy Outlook-2017 special report: Energy access outlook. Technical report, International Energy Agency.

[7] Antonia, R. A., Djenidi, L., and Spalart, P. R. (1994). Anisotropy of the dissipation tensor in a turbulent boundary layer. *Physics of Fluids*, 6(7):2475–2479.

[8] Atak, M., Beck, A., Bolemann, T., Flad, D., Frank, H., and Munz, C.-D. (2016). High fidelity scale-resolving computational fluid dynamics using

the high order discontinuous Galerkin spectral element method. In *High Performance Computing in Science and Engineering´ 15*, pages 511–530. Springer.

[9] Bae, J. H., Yoo, J. Y., and Choi, H. (2005). Direct numerical simulation of turbulent supercritical flows with heat transfer. *Physics of Fluids*, 17(10).

[10] Bae, J. H., Yoo, J. Y., and McEligot, D. M. (2008). Direct numerical simulation of heated CO2 flows at supercritical pressure in a vertical annulus at Re=8900. *Physics of Fluids*, 20(5).

[11] Bae, Y.-Y., Kim, E.-S., and Kim, M. (2017a). Assessment of low-Reynolds number k-ε turbulence models against highly buoyant flows. *International Journal of Heat and Mass Transfer*, 108(Part A):529 – 536.

[12] Bae, Y.-Y., Kim, E.-S., and Kim, M. (2017b). Numerical simulation of upward flowing supercritical fluids using buoyancy-influence-reflected turbulence model. *Nuclear Engineering and Design*, 324:231 – 249.

[13] Bae, Y.-Y. and Kim, H.-Y. (2009). Convective heat transfer to CO2 at a supercritical pressure flowing vertically upward in tubes and an annular channel. *Experimental Thermal and Fluid Science*, 33(2):329 – 339.

[14] Bae, Y.-Y., Kim, H.-Y., and Kang, D.-J. (2010). Forced and mixed convection heat transfer to supercritical CO2 vertically flowing in a uniformly-heated circular tube. *Experimental Thermal and Fluid Science*, 34(8):1295 – 1308.

[15] Bailly, C. and Comte-Bellot, G. (2015). *Wall-Bounded Turbulent Flows*, pages 51–83. Springer International Publishing, Cham.

[16] Banuti, D. T., Raju, M., and Ihme, M. (2017). Similarity law for Widom lines and coexistence lines. *Phys. Rev. E*, 95:052120.

[17] Beck, A. D., Bolemann, T., Flad, D., Frank, H., Gassner, G. J., Hindenlang, F., and Munz, C.-D. (2014). High-order discontinuous Galerkin spectral element methods for transitional and turbulent flow simulations. *International Journal for Numerical Methods in Fluids*, 76(8):522–548.

[18] Bell, I. H., Wronski, J., Quoilin, S., and Lemort, V. (2014). Pure and pseudo-pure fluid thermophysical property evaluation and the open-source thermophysical property library coolprop. *Industrial & Engineering Chemistry Research*, 53(6):2498–2508.

[19] Bishop, A., Sandberg, R., and Tong, L. (1964). Forced-convection heat transfer to water at near-critical temperatures and supercritical pressures. Technical report, Westinghouse Electric Corporation, Pittsburgh.

[20] Bringer, R. and Smith, J. (1957). Heat transfer in the critical region. *AIChE Journal*, 3(1):49–55.

[21] Cai, J., Renault, C., and Gou, J. (2014). Supercritical Water-Cooled Reactors. *Science and Technology of Nuclear Installations*.

[22] Cao, X., Rao, Z., and Liao, S. (2011). Laminar convective heat transfer of supercritical CO2 in horizontal miniature circular and triangular tubes. *Applied Thermal Engineering*, 31(14-15):2374–2384.

[23] Chalmers, H. and Gibbins, J. (2007). Initial evaluation of the impact of post-combustion capture of carbon dioxide on supercritical pulverised coal power plant part load performance. *Fuel*, 86(14):2109 – 2123.

[24] Chang, W., Chu, X., Fareed, A. F. B. S., Pandey, S., Luo, J., Weigand, B., and Laurien, E. (2018). Heat transfer prediction of supercritical water with artificial neural networks. *Applied Thermal Engineering*, 131:815 – 824.

[25] Chauvin, Y. and Rumelhart, D. (1995). *Backpropagation: theory, architectures, and applications*. Psychology Press.

[26] Chen, H., Goswami, D., Rahman, M., and Stefanakos, E. (2011). A supercritical Rankine cycle using zeotropic mixture working fluids for the conversion of low-grade heat into power. *Energy*, 36(1):549 – 555.

[27] Cheng, L., Ribatski, G., and Thome, J. R. (2008). Analysis of supercritical CO2 cooling in macro- and micro-channels. *International Journal of Refrigeration*, 31(8):1301 – 1316.

[28] Chu, X. (2016). *Direct numerical simulation of heat transfer to supercritical carbon dioxide in pipe flows*. PhD thesis. Institute of Nuclear Technology and Energy Systems, University of Stuttgart.

[29] Chu, X., Chang, W., Pandey, S., Luo, J., Weigand, B., and Laurien, E. (2018). A computationally light data-driven approach for heat transfer and hydraulic characteristics modeling of supercritical fluids: From DNS to DNN. *International Journal of Heat and Mass Transfer*, 123:629 – 636.

[30] Chu, X. and Laurien, E. (2016a). Direct numerical simulation of heated turbulent pipe flow at supercritical pressure. *Journal of Nuclear Engineering and Radiation Science*, (2).

[31] Chu, X. and Laurien, E. (2016b). Flow stratification of supercritical CO2 in a heated horizontal pipe. *The Journal of Supercritical Fluids*, 116:172 – 189.

[32] Coleman, G. N., Kim, J., and Moser, R. D. (1995). A numerical study of turbulent supersonic isothermal-wall channel flow. *Journal of Fluid Mechanics*, 305:159–183.

[33] Dang, C. and Hihara, E. (2004). In-tube cooling heat transfer of supercritical carbon dioxide. part 1. experimental measurement. *International Journal of Refrigeration*, 27(7):736 – 747.

[34] Deng, L. and Yu, D. (2014). Deep learning: Methods and applications. *Foundations and Trends® in Signal Processing*, 7(3–4):197–387.

[35] Dhanuskodi, R., Kaliappan, R., Suresh, S., Anantharaman, N., Arunagiri, A., and Krishnaiah, J. (2015). Artificial neural networks model for predicting wall temperature of supercritical boilers. *Applied Thermal Engineering*, 90:749–753.

[36] Dostal, V., Driscoll, M., and Hejzlar, P. (2004). A supercritical carbon dioxide cycle for next generation nuclear reactors. Technical report, MIT.

[37] Du, Z., Lin, W., and Gu, A. (2010). Numerical investigation of cooling heat transfer to supercritical CO2 in a horizontal circular tube. *The Journal of Supercritical Fluids*, 55(1):116 – 121.

[38] Duarte, A. R. C., Mano, J. F., and Reis, R. L. (2009). Supercritical fluids in biomedical and tissue engineering applications: a review. *International Materials Reviews*, 54(4):214–222.

[39] Dumbser, M., Iben, U., and Munz, C.-D. (2013). Efficient implementation of high order unstructured WENO schemes for cavitating flows. *Computers & Fluids*, 86(Supplement C):141 – 168.

[40] El Khoury, G. K., Schlatter, P., Noorani, A., Fischer, P. F., Brethouwer, G., and Johansson, A. V. (2013). Direct numerical simulation of turbulent pipe flow at moderately high Reynolds numbers. *Flow, Turbulence and Combustion*, 91(3):475–495.

[41] Fechter, S. and Munz, C.-D. (2015). A discontinuous Galerkin-based sharp-interface method to simulate three-dimensional compressible two-phase flow. *International Journal for Numerical Methods in Fluids*, 78(7):413–435. fld.4022.

[42] Fechter, S., Munz, C.-D., Rohde, C., and Zeiler, C. (2017). Approximate Riemann solver for compressible liquid vapor flow with phase transition and surface tension. *Computers & Fluids*.

[43] Feichi, Z., Bonart, H., Zirwes, T., Habisreuther, P., Bockhorn, H., and Zarzalis, N. (2015). Direct numerical simulation of chemically reacting flows with the public domain code openfoam. In Nagel, W. E., Kröner, D. H., and Resch, M. M., editors, *High Performance Computing in Science and Engineering '14*, pages 221–236, Cham. Springer International Publishing.

[44] Flaig, W., Mertz, R., and Starflinger, J. (2018). Setup of the supercritical co2 test facility "SCARLETT" for basic experimental investigations of a compact heat exchanger for an innovative decay heat removal system. *Journal of Nuclear Engineering and Radation Science*, 4(3):031004–031004–11.

[45] Föll, F., F., S., Hitz, T., and Munz, C.-D. (2017). Near critical jet simulations with a dg method and tabulated general equations of state. In *The 3rd International Conference on Numerical Methods in Multiphase Flows*.

[46] Fukagata, K., Iwamoto, K., and Kasagi, N. (2002). Contribution of Reynolds stress distribution to the skin friction in wall-bounded flows. *Physics of Fluids*, 14(11):L73–L76.

[47] Fukagata, K. and Kasagi, N. (2003). Drag reduction in turbulent pipe flow with feedback control applied partially to wall. *International Journal of Heat and Fluid Flow*, 24(4):480 – 490.

[48] Gassner, G. J. and Beck, A. D. (2013). On the accuracy of high-order discretizations for underresolved turbulence simulations. *Theoretical and Computational Fluid Dynamics*, 27(3):221–237.

[49] Gassner, G. J., Winters, A. R., and Kopriva, D. A. (2016). Split form nodal discontinuous galerkin schemes with summation-by-parts property for the compressible euler equations. *Journal of Computational Physics*, 327:39 – 66.

[50] Glushchenko, L., Kalachev, S., and Gandzyuk, O. (1972). Determining conditions of existence of deteriorated heat-transfer at supercritical pressures of medium. *Thermal Engineering*, 19(2):107–111.

[51] Gomez, T., Flutet, V., and Sagaut, P. (2009). Contribution of Reynolds stress distribution to the skin friction in compressible turbulent channel flows. *Phys. Rev. E*, 79:035301.

[52] Grigull, S. E. E. U. (1946). Heat transfer by liquids near the critical state.

[53] Habchi, C. and Antar, G. (2015). Direct numerical simulation of electromagnetically forced flows using openfoam. *Computers & Fluids*, 116:1 – 9.

[54] Harald, G. (1995). *Untersuchungen zur Thermohydraulik innenberippter Verdampferrohre*. PhD thesis, Technische Universität München.

[55] He, S., He, K., and Seddighi, M. (2016). Laminarisation of flow at low Reynolds number due to streamwise body force. *Journal of Fluid Mechanics*, 809:31–71.

[56] He, S., Kim, W., and Bae, J. (2008). Assessment of performance of turbulence models in predicting supercritical pressure heat transfer in a vertical tube. *International Journal of Heat and Mass Transfer*, 51(19):4659 – 4675.

[57] Hindenlang, F., Gassner, G. J., Altmann, C., Beck, A., Staudenmaier, M., and Munz, C.-D. (2012). Explicit discontinuous Galerkin methods for unsteady problems. *Computers & Fluids*, 61:86–93.

[58] Issa, R. (1986). Solution of the implicitly discretised fluid flow equations by operator-splitting. *Journal of Computational Physics*, 62(1):40 – 65.

[59] Jackson, J. (2002). Consideration of the heat transfer properties of supercritical pressure water in connection with the cooling of advanced nuclear reactors. In *Pacific Basin Nuclear Conference*.

[60] Jackson, J. and Fewster, J. (1975). Forced convection data for supercritical pressure fluids. Technical report, HTFS.

[61] Jackson, J. D. (2017). Models of heat transfer to fluids at supercritical pressure with influences of buoyancy and acceleration. *Applied Thermal Engineering*, 124:1481–1491.

[62] Jeong, J. and Hussain, F. (1995). On the identification of a vortex. *Journal of Fluid Mechanics*, 285:69–94.

[63] Jiang, P., Zhang, Y., Xu, Y., and Shi, R. (2008). Experimental and numerical investigation of convection heat transfer of CO2 at supercritical pressures in a vertical tube at low Reynolds numbers. *International Journal of Thermal Sciences*, 47(8):998–1011.

[64] Jiang, P.-X., Zhao, C.-R., Shi, R.-F., Chen, Y., and Ambrosini, W. (2009). Experimental and numerical study of convection heat transfer of CO2 at super-critical pressures during cooling in small vertical tube. *International Journal of Heat and Mass Transfer*, 52(21):4748 – 4756.

[65] Kawai, S., Terashima, H., and Negishi, H. (2015). A robust and accurate numerical method for transcritical turbulent flows at supercritical pressure with an arbitrary equation of state. *Journal of Computational Physics*, 300:116 – 135.

[66] Kays, W. M., Crawford, M. E., and Weigand, B. (2012). *Convective heat and mass transfer*. Tata McGraw-Hill Education.

[67] Kim, D. E. and Kim, M.-H. (2011). Experimental investigation of heat transfer in vertical upward and downward supercritical CO2 flow in a circular tube. *International Journal of Heat and Fluid Flow*, 32(1):176 – 191.

[68] Kim, H., Bae, Y., Kim, H., Soong, J., and Cho, B. (2006). Experimental investigation on the heat transfer characteristics on a vertical upward flow of supercritical CO2. In *Proc. ICAPP, Reno, NV*.

[69] Kim, J., Moin, P., and Moser, R. (1987). Turbulence statistics in fully developed channel flow at low Reynolds number. *Journal of Fluid Mechanics*, 177:133–166.

[70] Kim, K., Hickey, J.-P., and Scalo, C. (2017). Pseudophase-Change Effects in Turbulent Channel Flow under Transcritical Temperature Conditions. *ArXiv e-prints*.

[71] Kirillov, P., Pomet'ko, R., Smirnov, A., Grabezhnaia, V., Pioro, I., Duffey, R., and Khartabil, H. (2005). Experimental study on heat transfer to supercritical water flowing in 1-and 4-m-long vertical tubes. In *Proceedings of GLOBAL*.

[72] Kirillov, P. L. (2008). Supercritical water cooled reactors. *Thermal Engineering*, 55(5):361–364.

[73] Kotsiantis, S. B., Zaharakis, I., and Pintelas, P. (2007). Supervised machine learning: A review of classification techniques. *Emerging artificial intelligence applications in computer engineering*, 160:3–24.

[74] Krasnoshchekov, E. and Protopopov, V. (1960). About heat transfer in flow of carbon dioxide and water at supercritical region of state parameters. *Thermal Engineering*, 94(10).

[75] Laurien, E. (2016). Implicit model equation for hydraulic resistance and heat transfer including wall roughness. *Journal of Nuclear Engineering and Radiation Science*, 2(2).

[76] Lee, J., Jung, S. Y., Sung, H. J., and Zaki, T. A. (2013). Effect of wall heating on turbulent boundary layers with temperature-dependent viscosity. *Journal of Fluid Mechanics*, 726:196–225.

[77] Lee, J., Jung, S. Y., Sung, H. J., and Zaki, T. A. (2014). Turbulent thermal boundary layers with temperature-dependent viscosity. *International Journal of Heat and Fluid Flow*, 49:43 – 52. 8th Symposium on Turbulence & Shear Flow Phenomena (TSFP8).

[78] Lee, R. and Haller, K. (1974). Supercritical water heat transfer developments and applications. In *Proceedings of the 5th International Heat Transfer Conference, Tokyo, Japan, September*, pages 3–7.

[79] Lei, Y. and Chen, Z. (2018). Numerical study on cooling heat transfer and pressure drop of supercritical CO2 in wavy microchannels. *International Journal of Refrigeration*, 90:46 – 57.

[80] Lele, S. K. (1994). Compressibility effects on turbulence. *Annual Review of Fluid Mechanics*, 26(1):211–254.

[81] Lemmon, E., Huber, M., and McLinden, M. (2013). NIST standard reference database 23: Reference fluid thermodynamic and transport properties-refprop, version 9.1.

[82] Liao, S. and Zhao, T. (2002). A numerical investigation of laminar convection of supercritical carbon dioxide in vertical mini/micro tubes. *Progress in Computational Fluid Dynamics, an International Journal*, 2(2-4):144–152.

[83] Liu, Z.-B., He, Y.-L., Qu, Z.-G., and Tao, W.-Q. (2015). Experimental study of heat transfer and pressure drop of supercritical CO2 cooled in metal foam tubes. *International Journal of Heat and Mass Transfer*, 85:679 – 693.

[84] Liu, Z.-B., He, Y.-L., Yang, Y.-F., and Fei, J.-Y. (2014). Experimental study on heat transfer and pressure drop of supercritical CO2 cooled in a large tube. *Applied Thermal Engineering*, 70(1):307 – 315.

[85] Lumley, J. L. and Newman, G. R. (1977). The return to isotropy of homogeneous turbulence. *Journal of Fluid Mechanics*, 82(1):161–178.

[86] Lund, T. S., Wu, X., and Squires, K. D. (1998). Generation of turbulent inflow data for spatially-developing boundary layer simulations. *J. Comput. Phys.*, 140(2):233–258.

[87] Ma, P. C., Yang, X. I. A., and Ihme, M. (2018). Structure of wall-bounded flows at transcritical conditions. *Phys. Rev. Fluids*, 3:034609.

[88] MacKay, D. (1992). Bayesian interpolation. *Neural Computation*, 4(3):415–447.

[89] McAdams, W. (1942). *Heat transmission*. McGraw-Hill, New York, NY, USA, 2nd edition.

[90] McEligot, D., Coon, C., and Perkins, H. (1970). Relaminarization in tubes. *International Journal of Heat and Mass Transfer*, 13:431 – 433.

[91] McEligot, D. M. and Laurien, E. (2015). Insight from simple heat transfer models. In *The 7th International Symposium on Supercritical Water-Cooled Reactors(ISSCWR-7), Helsinki, Finland.*

[92] Miropol'skii, Z., L. and Shitsman, M., E. (1958). Investigation of heat transfer to water and steam at pressures up to 280 ATA (in Russian). In *Investigation of Heat Transfer to Steam and Water Boiling in Tubes at High Pressures*.

[93] Narasimha, R. and Sreenivasan, K. R. (1973). Relaminarization in highly accelerated turbulent boundary layers. *Journal of Fluid Mechanics*, 61(3):417–447.

[94] Nemati, H., Patel, A., Boersma, B. J., and Pecnik, R. (2015). Mean statistics of a heated turbulent pipe flow at supercritical pressure. *International Journal of Heat and Mass Transfer*, 83:741 – 752.

[95] Nemati, H., Patel, A., Boersma, B. J., and Pecnik, R. (2016). The effect of thermal boundary conditions on forced convection heat transfer to fluids at supercritical pressure. *Journal of Fluid Mechanics*, 800:531–556.

[96] OpenFOAM (2015). *OpenFOAM. The Open Source CFD Toolbox. User Guide*. OpenFOAM Foundation Ltd.

[97] Pandey, S., Chu, X., and Laurien, E. (2017a). Investigation of in-tube cooling of carbon dioxide at supercritical pressure by means of direct numerical simulation. *International Journal of Heat and Mass Transfer*, 114:944 – 957.

[98] Pandey, S., Chu, X., and Laurien, E. (2018a). Numerical analysis of heat transfer during cooling of supercritical fluid by means of direct numerical simulation. In Nagel, W. E., Kröner, D. H., and Resch, M. M., editors, *High Performance Computing in Science and Engineering ' 17*, pages 241–254, Cham. Springer International Publishing.

[99] Pandey, S., Chu, X., Laurien, E., and Weigand, B. (2018b). Buoyancy induced turbulence modulation in pipe flow at supercritical pressure under cooling conditions. *Physics of Fluids*, 30(6):065105.

[100] Pandey, S. and Laurien, E. (2016). Heat transfer analysis at supercritical pressure using two layer theory. *Journal of Supercritical Fluids*, 109:80–86.

[101] Pandey, S., Laurien, E., and Chu, X. (2017b). A modified convective heat transfer model for heated pipe flow of supercritical carbon dioxide. *International Journal of Thermal Sciences*, 117:227 – 238.

[102] Peeters, J. W. R., Pecnik, R., Rohde, M., van der Hagen, T., and Boersma, B. J. (2016). Turbulence attenuation in simultaneously heated and cooled annular flows at supercritical pressure. *Journal of Fluid Mechanics*, 799:505–540.

[103] Peng, D.-Y. and Robinson, D. B. (1976). A new two-constant equation of state. *Ind. Eng. Chem. Fund.*, 15(1):59–64.

[104] Pesteei, S. and Mehrabi, M. (2010). Modeling of convection heat transfer of supercritical carbon dioxide in a vertical tube at low Reynolds numbers using artificial neural network. *International Communications in Heat and Mass Transfer*, 37(7):901–906.

[105] Petukhov, B. (1970). Heat transfer and friction in turbulent pipe flow with variable physical properties. volume 6 of *Advances in Heat Transfer*, pages 503 – 564. Elsevier.

[106] Pioro, I., Khartabil, H., and Duffey, R. (2004). Heat transfer to supercritical fluids flowing in channels – empirical correlations (survey). *Nuclear Engineering and Design*, 230(1-3):69–91.

[107] Pioro, L. and Pioro, I. (1997). *Industrial two-phase thermosyphons*. Begell House.

[108] Pitla, S. S., Groll, E. A., and Ramadhyani, S. (2001). Convective heat transfer from in-tube cooling of turbulent supercritical carbon dioxide: Part 2-experimental data and numerical predictions. *HVAC&R Research*, 7(4):367–382.

[109] Pucciarelli, A. and Ambrosini, W. (2017). Improvements in the prediction of heat transfer to supercritical pressure fluids by the use of algebraic heat flux models. *Annals of Nuclear Energy*, 99:58 – 67.

[110] Pucciarelli, A., Borroni, I., Sharabi, M., and Ambrosini, W. (2015). Results of 4-equation turbulence models in the prediction of heat transfer to supercritical pressure fluids. *Nuclear Engineering and Design*, 281:5 – 14.

[111] Rahman, M., Jahan, N., and Zhao, J. (2017). Critical analysis of supercritical water cooled reactors (scwrs) and nuclear marine vessels for application of scwr in ship. In *International Conference on Fast Reactors and Related Fuel Cycles: Next Generation Nuclear Systems for Sustainable Development*.

[112] Redlich, O. and Kwong, J. N. S. (1949). On the thermodynamics of solutions. v. an equation of state. fugacities of gaseous solutions. *Chem. Rev.*, 44(1):233–244.

[113] Scalabrin, G. and Piazza, L. (2003). Analysis of forced convection heat transfer to supercritical carbon dioxide inside tubes using neural networks. *International Journal of Heat and Mass Transfer*, 46(7):1139–1154.

[114] Schaffel-Mancini, N., Mancini, M., Szlek, A., and Weber, R. (2010). Novel conceptual design of a supercritical pulverized coal boiler utilizing high temperature air combustion (HTAC) technology. *Energy*, 35(7):2752 – 2760.

[115] Schmidhuber, J. (2015). Deep learning in neural networks: An overview. *Neural Networks*, 61:85–117.

[116] Schoppa, W. and Hussain, F. (2000). Coherent structure dynamics in near-wall turbulence. *Fluid Dynamics Research*, 26(2):119 – 139.

[117] Schulenberg, T., Starflinger, J., Marsault, P., Bittermann, D., Maraczy, C., Laurien, E., Nijeholt, J., Anglart, H., Andreani, M., Ruzickova, M., and Toivonen, A. (2011). European supercritical water cooled reactor. *Nuclear Engineering and Design*, 241(9):3505–3513.

[118] Schuster, A., Karellas, S., and Aumann, R. (2010). Efficiency optimization potential in supercritical organic Rankine cycles. *Energy*, 35(2):1033 – 1039. ECOS 2008.

[119] Sengupta, U., Nemati, H., Boersma, B. J., and Pecnik, R. (2017). Fully compressible low-mach number simulations of carbon-dioxide at supercritical pressures and trans-critical temperatures. *Flow, Turbulence and Combustion*, 99(3):909–931.

[120] Sharabi, M., Ambrosini, W., He, S., and Jackson, J. (2008). Prediction of turbulent convective heat transfer to a fluid at supercritical pressure in square and triangular channels. *Annals of Nuclear Energy*, 35(6):993 – 1005.

[121] Shehata, A. and McEligot, D. M. (1998). Mean structure in the viscous layer of strongly-heated internal gas flows. Measurements. *International Journal of Heat and Mass Transfer*, 41(24):4297 – 4313.

[122] Shenoy, A. (1987). Effects of buoyancy on heat transfer during turbulent flow on drag reducing fluids in vertical pipes. *Heat and Mass Transfer*, 21(1):15–18.

[123] Shiralkar BS, G. P. (1969). Deterioration in heat transfer to fluids at supercritical pressure and high heat fluxes. (91):27–36.

[124] Shitsman, M. (1963). Impairment of the heat transmission at supercritical pressures(heat transfer process examined during forced motion of water at supercritical pressures). *High temperature*, 1:237–244.

[125] Shitsman, M. (1968). Temperature conditions in tubes at supercritical pressures. *Thermal Engineering*, 15(5):72–77.

[126] Sonntag, M. and Munz, C.-D. (2017). Efficient parallelization of a shock capturing for discontinuous Galerkin methods using finite volume sub-cells. *Journal of Scientific Computing*, 70(3):1262–1289.

[127] Span, R. and Wagner, W. (1996). A new equation of state for carbon dioxide covering the fluid region from the triple-point temperature to 1100 K at pressures up to 800 MPa. *Journal of Physical and Chemical Reference Data*, 25(6):1509–1596.

[128] Tanaka, H., Nishiwaki, N., and Hirata, M. (1967). Turbulent heat transfer in vertical tubes at supercritical pressures. pages 127–134.

[129] Wallace, J. M. (2016). Quadrant analysis in turbulence research: History and evolution. *Annual Review of Fluid Mechanics*, 48(1):131–158.

[130] Wallace, J. M., Eckelmann, H., and Brodkey, R. S. (1972). The wall region in turbulent shear flow. *Journal of Fluid Mechanics*, 54(1):39–48.

[131] Wang, K.-Z., Xu, X.-X., Liu, C., Bai, W.-J., and bin Dang, C. (2017). Experimental and numerical investigation on heat transfer characteristics of supercritical CO2 in the cooled helically coiled tube. *International Journal of Heat and Mass Transfer*, 108:1645 – 1655.

[132] X. Zhang, H. Yamaguchi, D. U. (2007). Experimental study on the performance of solar rankine system using supercritical CO2. *Renewable Energy*, 32(15):2617 – 2628.

[133] X. Zhang, H. Y. (2008). An experimental study on evacuated tube solar collector using supercritical CO2. *Applied Thermal Engineering*, 28(10):1225 – 1233.

[134] Xu, R.-N., Luo, F., and Jiang, P.-X. (2017). Buoyancy effects on turbulent heat transfer of supercritical CO2 in a vertical mini-tube based on continuous wall temperature measurements. *International Journal of Heat and Mass Transfer*, 110:576 – 586.

[135] Yamagata, K., Nishikawa, K., Hasegawa, S., Fujii, T., and Yoshida, S. (1972). Forced convective heat transfer to supercritical water flowing in tubes. *International Journal of Heat and Mass Transfer*, 15(12):2575 – 2593.

[136] Yang, M. (2016). Numerical study of the heat transfer to carbon dioxide in horizontal helically coiled tubes under supercritical pressure. *Applied Thermal Engineering*, 109, Part A:685 – 696.

[137] Yang, Y., Wang, L., Dong, C., Xu, G., Morosuk, T., and Tsatsaronis, G. (2013). Comprehensive exergy-based evaluation and parametric study of a coal-fired ultra-supercritical power plant. *Applied Energy*, 112:1087 – 1099.

[138] Yoo, J. Y. (2013). The turbulent flows of supercritical fluids with heat transfer. *Annual review of fluid mechanics*, 45:495–525.

[139] Zhang, G.-W., Hu, P., Chen, L.-X., and Liu, M.-H. (2018). Experimental and simulation investigation on heat transfer characteristics of in-tube supercritical CO2 cooling flow. *Applied Thermal Engineering*.

Appendix A

Supplementary results from the DNS of turbulent pipe flow

This section briefly discusses the results from few more cases for turbulent pipe flow simulation conducted using OpenFOAM.

A.1 Effects of wall heat flux and inlet temperature

Earlier, only fives cases were discussed in details in Chapter 3 from the qualitative discussion point of view. The results from the rest of the cases are presented here. The results presented in this section follow a similar trend to what was discussed in Section 3.3. Therefore, these results are only shown in graphical form without any further discussion to avoid redundant information.

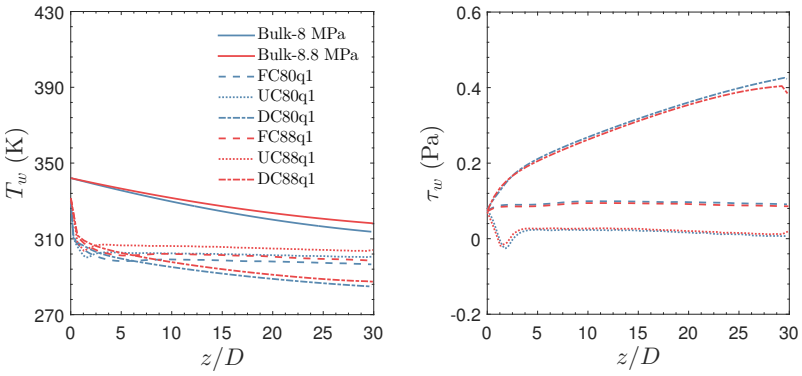

(a) (b)

Fig. A.1 Streamwise variation of (a): wall temperature, and (b): wall shear stress for q_w=-30.87 kW/m^2, T_i= 342.05 K, corresponding to Table 3.1

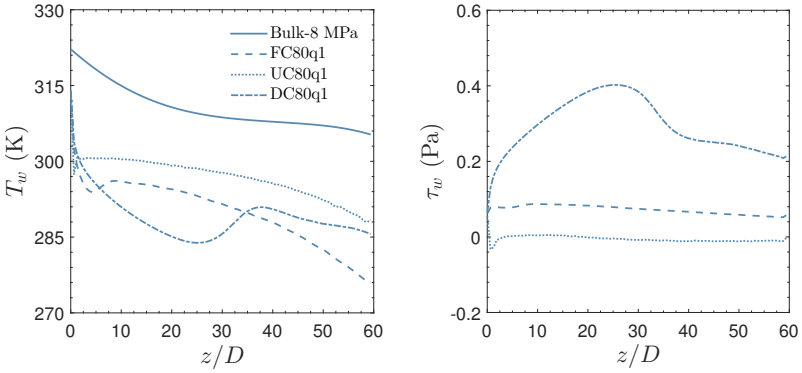

(a) (b)

Fig. A.2 Streamwise variation of (a): wall temperature, and (b): wall shear stress for q_w=-30.87 kW/m^2, T_i= 322.18 K, corresponding to Table 3.2

A.2 Effects of non-uniform wall heat flux

Most of the DNS investigations including the present one is made with a uniform wall heat flux imposed at the wall. However, in practical, the wall heat flux may vary along circumferentially or axially or both, for e.g. in concentrated solar thermal power plants. Few studies are present in the literature with inhomogeneous wall heat flux but mostly employed turbulence modeling which is not a reliable option for such complex flows. Therefore, an investigation is also made within this thesis for non-uniform wall heat flux.

For the DNS, six distinct cases were selected which correspond to the variation in imposed wall heat flux profile. Table A.1 shows the simulation conditions. All cases have same inlet condition with an inlet temperature of 301.15 K and inlet pressure of 8 MPa. The inlet bulk Reynolds number is 5400 and it results in a friction Reynolds number of 180. The first case has a uniform heat flux profile and it serves as a reference case and remaining case has the variable heat flux in either axial or circumferential direction.

Table A.1 A summary of simulation conditions for DNS with non-uniform heat flux

Case	q_w	$q_{w,min}$	$q_{w,max}$	Re_0
Uni	15	15	15	2800
AxSin	$15+5Sinz$	10	20	2800
AxCos	$15+5Cosz$	10	20	2800
AxLin	$10+10z$	10	20	2800
CirSin	$15+5Sin\theta$	10	20	2800
CirCos	$15+5Cos\theta$	10	20	2800

Figure A.3 depicts the variation of the wall heat flux and wall temperature for all six cases. There exists a slight difference in case AxLin, AxSin, AxCos and Uni due to the different magnitude of wall heat flux. The area averaged wall heat flux follows the uniform heat flux in the streamwise

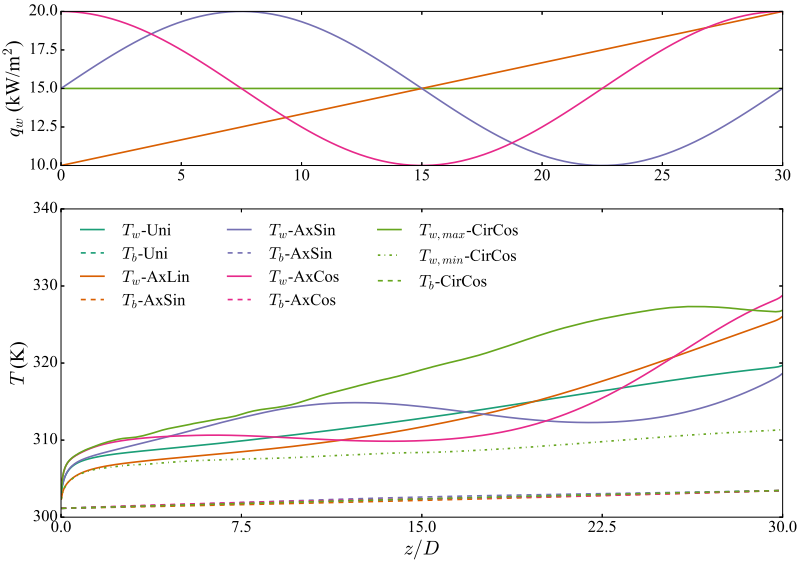

Fig. A.3 Axial variations of (a) wall heat flux and (b) temperature

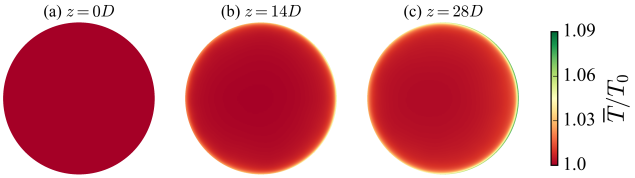

Fig. A.4 Development of mean temperature field for case 15CirCos1

direction for case CirCos because of $q_w = \int_0^{2\pi}(15+5Cos\theta)d\theta = 15$. The bulk temperature monotonically increases from inlet to outlet in all cases. The profile of bulk temperature completely overlaps for cases Uni, CirSin

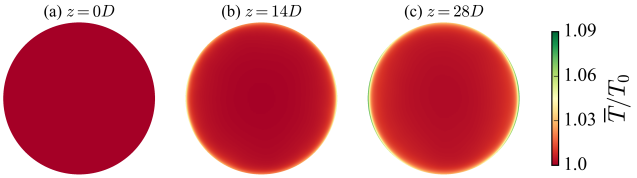

Fig. A.5 Development of mean temperature field for case 15CirCos2

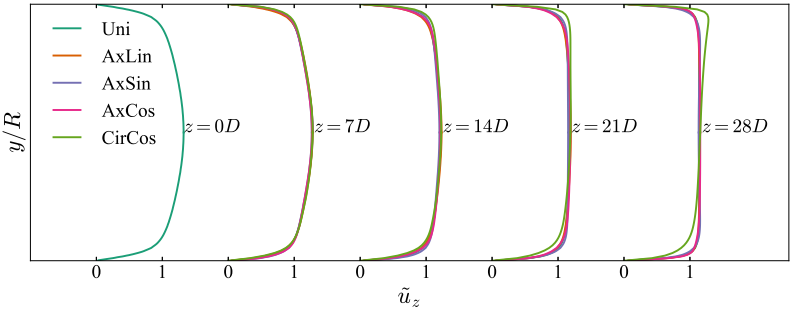

Fig. A.6 Favre averaged streamwise velocity profile

and CirCos because of the equal heat flux along the cross section. The wall temperature increases intensely compared to the bulk temperature and it significantly differs in every case. The variation of wall temperature closely follows the heat flux variations, showing peak and valley corresponding to the heat flux. Moreover, the maximum and minimum wall temperature for cases CirSin and CirCos also overlap, however, their position in separated by $\pi/2$ along the circumference. The difference between the maximum and minimum heat flux is kept 10 kW/m^2 for case CirCos. It induces temperature variations along the circumferential direction. As a result of buoyancy, effects of thermal stratification arises. These thermal stratification characteristics

are quite different than the horizontal flow of supercritical CO_2, which was observed by Chu and Laurien [31]. On the other hand, in case CirCos, thermal stratification is a result of non-uniform heat flux along the circumference and it will exist even gravity is absent. The stratification can be visualized in Figure A.4 and A.5. Figure A.6 depicts the deformed velocity profile along the streamwise direction.

Appendix B

Semi-analytical model employing DNS data

In Chapter 5, a purely data-driven model was discussed which was based on the machine learning based algorithm. A different approach for using DNS data has been shown in this chapter which is based on the physics based model. This model is based on the famous two layer model pioneered by Ludwig Prandtl [4] for constant-property turbulent flow. Prandtl assumed that turbulent flow in a pipe consists of two layers, namely (i) a laminar sub-layer and (ii) a turbulent core layer, as shown in Fig. B.1a. In laminar sub-layer, only molecular transport is significant while in the turbulent core layer, turbulent transport plays a significant role in momentum transfer. These two layers are distinguished by velocity profiles and thickness of the viscous sub-layer is determined by the intersection of the velocity profile of different region as shown in Fig. B.1b. In viscous sub-layer, $u^+ = y^+$ is valid (blue colored in Fig. B.1b) while in turbulent core layer u^+ is directly proportional to the logarithmic of the distance from the wall (red colored in Fig. B.1b). Here superscript '+ 'represents the non-dimensional form as: $u^+ = u/u_\tau$ and

$y^+ = \frac{yu_\tau}{\nu}$. It is a well-established model for constant properties and already been attempted by Petukhov [105] for variable properties.

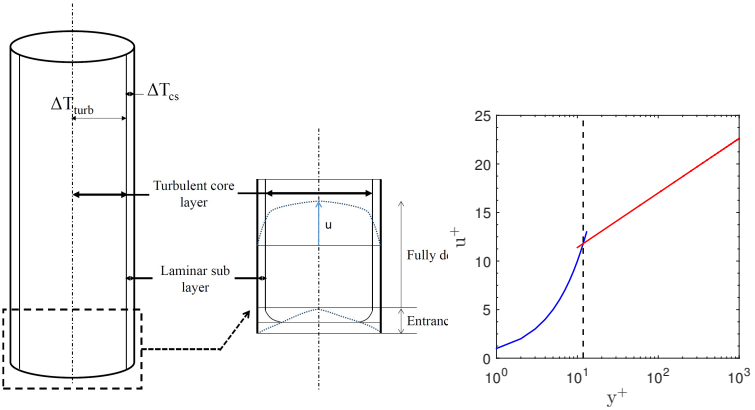

(a) (b)

Fig. B.1 (a): A graphical representation of two layer model (not to scale), and (b): Velocity profile in wall units for constant properties in two layer

For variable properties, the temperature difference across these layers can be found out by the logarithmic law of the wall and/or thermal resistance offered by different layers (refer McEligot and Laurien [75, 91] for a detailed derivation). First, the temperature difference across the turbulent core layer (ΔT_{turb}) is estimated while approximating the centre line temperature ($\overline{T_{cl}}$) and the bulk temperature (T_b) and it is calculated by utilizing the bulk shear velocity (u_{τ_b}), wall heat flux (q_w), bulk density (ρ_b), isobaric specific heat calculated at bulk temperature (C_{pb}), turbulent Prandtl number (Pr_T), von-Kármán constant (κ), dimensionless radius (R^{+b}), thickness of conducting sub-layer (y_{cs}^{+b}), dynamic viscosity (μ) and Prandtl number (Pr).

$$\Delta T_{turb} = T_{cs} - \overline{T_{cl}} = \frac{\mathrm{Pr_T}}{\kappa}\left(lnR^{+w} - lny_{cs}^{+b}\right)\left(\frac{q_w}{u_{\tau b}\rho_b C_{pb}}\right) \tag{B.1}$$

Where,

$$u_\tau = \sqrt{\frac{|\tau_w|}{\rho}} \;\; ; \;\; R^+ = \frac{\rho R u_\tau}{\mu} \;\; ; \;\; y_{cs}^{+b} = \frac{y_{vs}^+}{\mathrm{Pr}_{cs}^{\frac{1}{3}}} \;\; ; \;\; y_{vs}^+ = 11.8$$

Temperature difference across conducting sub-layer (ΔT_{cs}) is determined by using the thermal resistance analogy. After integrating Fourier's law of conduction in the conducting sub-layer, the temperature difference across it is given as:

$$\Delta T_{cs} = \frac{q_w}{\alpha_{cs}} \tag{B.2}$$

Where heat transfer coefficient across conducting sub-layer (α_{cs}) is determined by using properties evaluated at conducting sub-layer (subscript 'cs') and wall (subscript 'w').

$$\alpha_{cs} = \frac{1}{y_{cs}} \frac{(\omega_w - \omega_{cs})}{(T_w - T_{cs})}$$

$$\omega = \int_{T_{ref}}^{T} \kappa(T) dT \;\; ; \;\; y_{cs} = \frac{y_{vs,w}}{\mathrm{Pr}_w^{\frac{1}{3}}} \;\; ; \;\; y_{vs}^+ = \frac{y_{vs,w} u_{\tau w}}{\upsilon_w} \;\; ; \;\; u_{\tau w} = \sqrt{\frac{\tau_w}{\rho_w}}$$

Here; κ represents the thermal conductivity, y_{cs} is the thickness of conducting sub-layer and $u_{\tau w}$ is shear velocity based upon wall temperature. The expression for the wall temperature (T_w) is given by:

$$T_w = \overline{T_{cl}} + \Delta T_{turb} + \Delta T_{cs} \tag{B.3}$$

And the wall shear stress (τ_w) is calculated as:

$$\tau_w = \mu \frac{du}{dy}\Big|_{y=0} \approx \mu \frac{u_{vs}}{y_{vs}} \tag{B.4}$$

For velocity at the edge of viscous sub-layer (u_{vs}), the logarithmic law of the wall is used. The well known power law velocity profile, $u/u_{max} = (1-r/R)^{(1/n)}$ was utilized. The exponent n is a function of Reynolds number, however, $n = 7$ observed to be applicable to a wide range of pipe flows and is a good approximation [66]. Relation between maximum velocity i.e. velocity at the center (u_{cl}) and mean velocity (u_m) is derived as follow:

$$u_m = \frac{2}{R^2}\int_0^R u(r) r dr \tag{B.5}$$

$$u_m = \frac{2}{R^2}\int_0^R u_{cl}\left(1-\frac{r}{R}\right)^{\frac{1}{7}} r dr \tag{B.6}$$

$$u_{cl} = \frac{u_m}{0.8167} \tag{B.7}$$

$$\tag{B.8}$$

Then u_{vs} is given as:

$$u_{vs} = u_{cl} + \Delta u_{turb} \tag{B.9}$$

$$\Delta u_{turb} = \frac{1}{\kappa}\left(lnR^{+b} - lny_{cs}^{+b}\right) u_{\tau b} \tag{B.10}$$

The above mentioned model does not include the effects of buoyancy and flow acceleration or deceleration. To account these effects, certain variables are introduced by using the knowledge gained from the DNS and are calibrated with the DNS data. Following section briefly explains the effects and how they are accounted in this model.

B.1 Relaminarization

During heating of sCO_2, fluid density decreases and it results in an increase in the fluid velocity. This will accelerate the fluid and creates a condition similar to a boundary layer subjected to a large favorable pressure gradient that will revert the turbulent flow to laminar [93]. This will influence the heat transfer to sCO_2 and it has to be accounted in the present model to enhance the accuracy. It is well agreed that the thickness of laminar sub-layer will increase due to relaminarization brought by acceleration and it will increase the thermal resistance thereby restricts the heat transfer between the wall and bulk fluid. Therefore, to account for this, the thickness of the viscous sub-layer is increased; equation B.11 is modified form of non-dimensional wall thickness. Here the acceleration parameter (K_v) is used, originally introduced by McEligot [90] while c_v is an empirically fitted parameter and its value is empirically fitted using the DNS data. In the equation, β is the thermal expansion coefficient and A is an arbitrary constant.

$$y_{vs}^{+} = 11.8 + c_v \mathrm{K_v} \tag{B.11}$$

Where

$$\mathrm{K_v} = \frac{4 q_w \mu_b \beta_b}{G D u_m \rho_b C_{pb}} \; ; c_v = A u_m^2$$

B.2 Buoyancy

Due to density variations in the radial direction of the flow, its effects cannot be neglected especially at high heat flux. The flow will change from forced convection flow to mixed type, where natural convection plays an important role. To take buoyancy into account, a buoyant shear stress is inserted in addition to wall shear stress. This approach to include buoyancy effect by an

extra shear stress has already been used for drag reducing fluids by Shenoy [122]. Equation B.12 shows the modified form of wall shear stress.

$$\tau_{w,m} = \tau_w + (flow\tau_b) \tag{B.12}$$

The resultant magnitude of the wall shear stress depends on the '*flow*' direction and intensity of buoyancy in a flow. The value of *flow* is calibrated with DNS data for upward and downward flow.

$$\tau_b = y_b g(\rho_b - \rho_m) \tag{B.13}$$

Where,

$$\rho_m = \frac{1}{(T_w - T_b)} \int_{T_b}^{T_w} \rho dT; \quad y_b = \frac{y_{vs}}{\mathrm{Pr}_{cs}{}^{\frac{1}{3}}}; \quad u_{\tau w} = \sqrt{\frac{\tau_{w,m}}{\rho_w}}$$

An additional parameter c_v was introduced earlier in equation B.11 to model the acceleration effect and it consists of an arbitrary constant A and u_m^2. The value of u_m^2 depends upon the flow while the magnitude of A was adjusted to have an optimized value of goodness of fit. The mean square error (MSE) was chosen as the goodness of fit and value of c_v is found to be 7.3×10^6 while optimizing MSE for wall temperature and modified wall shear stress. The second step in the process of calibration is to calibrate the data for buoyancy for equation B.13. For that, parameter '*flow*' was varied and MSE was optimized similarly to relaminarization.

B.3 Verification and validation

The constant property case is an important measure to check the validity of any model or correlation in the subcritical region and high-pressure region, where

Table B.1 Summary of calibration parameter

Case	A (in $c_v = Au_m^2$)	$flow$	μ in eq. B.4
Forced	7.3×10^6	0	μ_{cs}
Upward	7.3×10^6	1	μ_w
Downward	7.3×10^6	-10	μ_w

the properties variations are negligible. Figure B.2 shows the comparison of presented model with the most commonly used correlations. An excellent agreement can be observed at low Prandtl number. All the correlations deviate at high Pr. In spite of that, the current model agrees with the Gnielinski's correlation very well at all value of Re and Pr.

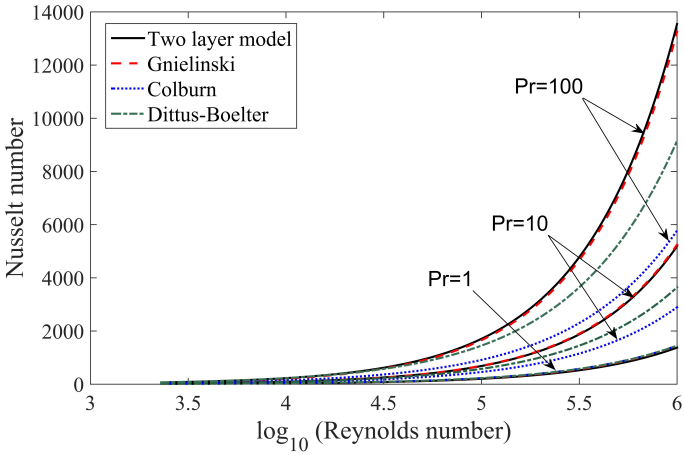

Fig. B.2 Variation of bulk Nusselt number with bulk Reynolds number

Figure B.3 depicts the validation for presented model with experiments of Kim et al. [68]. The mean relative error (MRE) is 13.1% for high heat

flux case (i.e. q_w= 50 kW/m^2). Also, heat transfer deterioration is predicted with higher accuracy than the previous as compared to the correlations (as depicted in Figure 1.4) and RANS models. For medium heat flux (correspond to q_w= 30 kW/m^2), there is not much improvement in term of MRE. Also, presented model predicts a peak in wall temperature, which wasn,t observed in experiments.

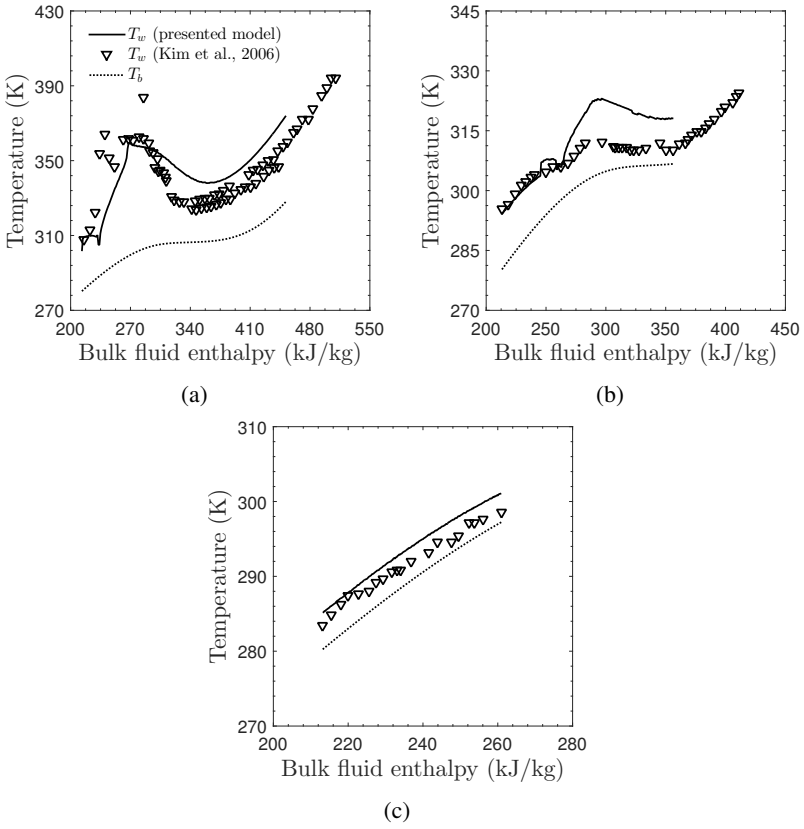

Fig. B.3 Variation of wall temperature with bulk fluid enthalpy (a) q_w= 50 kW/m^2 (b) q_w= 30 kW/m^2 (c) q_w= 10 kW/m^2

Figure B.4 illustrates the comparison with the experiments of Dang and Hihara [33]. Horizontal layout with comparatively larger mass flux to heat flux ratio was considered during the experiments. Therefore, smaller property variation and it resembles near-constant property case. An excellent agreement can be observed, including in the prediction of heat transfer enhancement at pseudocritical temperature.

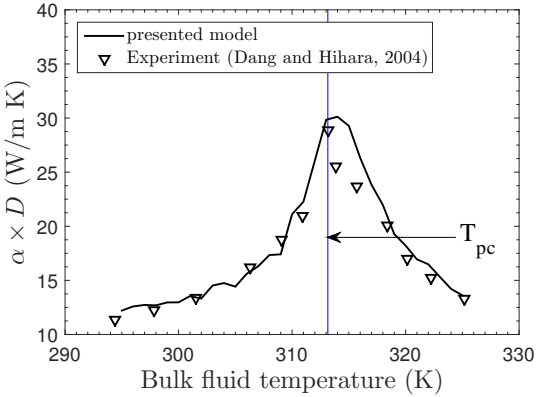

Fig. B.4 Comparison with experiments for cooling at P= 9 MPa, $G \times D$= 2.4 kg/m s, q_w= -12 kW/m^2

A fairly well agreement with the experimental can be seen with this method. However, only 3 cases of DNS were used to calibrate the model. To have a more comprehensive, reliable and generalize model, there is need to calibrate with more DNS cases.

Institut für Kernenergetik und
Energiesysteme

Universität Stuttgart
Pfaffenwaldring 31

D- 70569 Stuttgart